

SCIENCE OF TSUNAMI HAZARDS

Journal of Tsunami Society International

Volume 31

Number 1

2012

SIMULATION OF THE EFFECT OF FAR FIELD TSUNAMI THROUGH AN OPEN BOUNDARY CONDITION IN A BOUNDARY-FITTED CURVILINEAR GRID SYSTEM 1

Mohammed Ashaque Meah - *Dept. of Mathematics, Shahjalal University of Science & Technology, BANGLADESH*

Ahmad Izani M Ismail - *School of Mathematical Sciences, University Sains Malaysia, 11800 Pulau Pinang, MALAYSIA*

Md. Fazlul Karim - *Faculty of Engineering, Institute Technology Brunei, BRUNEI*

Md. Shafiqul Islam - *Dept. of Mathematics, Shahjalal University of Science & Technology, BANGLADESH*

THE SAMOA TSUNAMI OF 29 SEPTEMBER 2009 - Early Warning and Inundation Assessment 19

Giovanni Franchello - *European Commission, Joint Research Centre, Institute for the Protection and Security of the Citizen, Ispra (VA), ITALY*

Alessandro Annunziato¹ - *European Commission, Joint Research Centre, Institute for the Protection and Security of the Citizen, Ispra (VA), ITALY*

A STUDY OF THE EFFECT OF PERMEABILITY OF ROCKS IN TSUNAMI GENERATION AND PROPAGATION BY SEISMIC FAULTING USING LINEARIZED SHALLOW –WATER WAVE THEORY 62

Parul Saxena - *Dept of Mathematics, Jaypee Institute of Information Technology, Nodia, INDIA*

Lokendra Kumar - *Dept of Mathematics, Jaypee Institute of Information Technology, Nodia, INDIA*

ALGERIA'S VULNERABILITY TO TSUNAMIS FROM NEAR-FIELD SEISMIC SOURCES 82

L. Amir - *USTHB-FSTGAT, BP 32, Bab Ezzouar, Algiers, ALGERIA*

A. Cisternas - *Universidad De Chile, Santiago, CHILE*

J. -L. Vignerese - *UHP, UMR 7566, Vandoeuvre les Nancy, FRANCE*

W. Dudley - *University of Hawaii, Hilo, Hawaii, USA*

B. Mc Adoo - *Vassar College, Poughkeepsie, NY, 12601 USA*

WWW.TSUNAMISOCIETY.ORG

TSUNAMI SOCIETY INTERNATIONAL, 1741 Ala Moana Blvd. #70, Honolulu, HI 96815, USA.

SCIENCE OF TSUNAMI HAZARDS is a CERTIFIED OPEN ACCESS Journal included in the prestigious international academic journal database DOAJ, maintained by the University of Lund in Sweden with the support of the European Union. SCIENCE OF TSUNAMI HAZARDS is also preserved, archived and disseminated by the National Library, The Hague, NETHERLANDS, the Library of Congress, Washington D.C., USA, the Electronic Library of Los Alamos, National Laboratory, New Mexico, USA, the EBSCO Publishing databases and ELSEVIER Publishing in Amsterdam. The vast dissemination gives the journal additional global exposure and readership in 90% of the academic institutions worldwide, including nationwide access to databases in more than 70 countries.

OBJECTIVE: Tsunami Society International publishes this interdisciplinary journal to increase and disseminate knowledge about tsunamis and their hazards.

DISCLAIMER: Although the articles in SCIENCE OF TSUNAMI HAZARDS have been technically reviewed by peers, Tsunami Society International is not responsible for the veracity of any statement, opinion or consequences.

EDITORIAL STAFF

Dr. George Pararas-Carayannis, Editor
<mailto:drgeorgepc@yahoo.com>

EDITORIAL BOARD

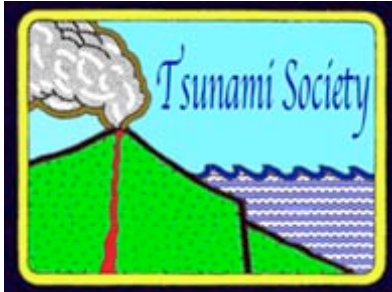
Dr. Charles MADER, Mader Consulting Co., Colorado, New Mexico, Hawaii, USA
Dr. Hermann FRITZ, Georgia Institute of Technology, USA
Prof. George CURTIS, University of Hawaii -Hilo, USA
Dr. Tad S. MURTY, University of Ottawa, CANADA
Dr. Zygmunt KOWALIK, University of Alaska, USA
Dr. Galen GISLER, NORWAY
Prof. Kam Tim CHAU, Hong Kong Polytechnic University, HONG KONG
Dr. Jochen BUNDSCHUH, (ICE) COSTA RICA, Royal Institute of Technology, SWEDEN
Dr. Yurii SHOKIN, Novosibirsk, RUSSIAN FEDERATION

TSUNAMI SOCIETY INTERNATIONAL, OFFICERS

Dr. George Pararas-Carayannis, President;
Dr. Tad Murty, Vice President;
Dr. Carolyn Forbes, Secretary/Treasurer.

Submit manuscripts of research papers, notes or letters to the Editor. If a research paper is accepted for publication the author(s) must submit a scan-ready manuscript, a Doc, TeX or a PDF file in the journal format. Issues of the journal are published electronically in PDF format. There is a minimal publication fee for authors who are members of Tsunami Society International for three years and slightly higher for non-members. Tsunami Society International members are notified by e-mail when a new issue is available. Permission to use figures, tables and brief excerpts from this journal in scientific and educational works is granted provided that the source is acknowledged.

Recent and all past journal issues are available at: <http://www.TsunamiSociety.org> CD-ROMs of past volumes may be purchased by contacting Tsunami Society International at postmaster@tsunamisociety.org Issues of the journal from 1982 thru 2005 are also available in PDF format at the Los Alamos National Laboratory Library <http://epubs.lanl.gov/tsunami/>



SIMULATION OF THE EFFECT OF FAR FIELD TSUNAMI THROUGH AN OPEN BOUNDARY CONDITION IN A BOUNDARY-FITTED CURVILINEAR GRID SYSTEM

Mohammed Ashaque Meah¹, Ahmad Izani M Ismail², Md. Fazlul Karim³, Md. Shafiqul Islam¹

¹*Department of Mathematics, Shahjalal University of Science & Technology, Bangladesh*

²*School of Mathematical Sciences, University Sains Malaysia, 11800 Pulau Pinang, Malaysia*

³*Faculty of Engineering, Institute Technology Brunei, Brunei*

Corresponding Author: Dr. Mohammed Ashaque Meah, Associate Professor, Dept of Mathematics, Shahjalal University of Science & Technology, Sylhet, Bangladesh. Phone: 88-0821-717850-256.

mamsust@yahoo.com ; izani@cs.usm.my; karimfazlul67@gmail.com ; msim5588@gmail.com

ABSTRACT

A new approach is developed to simulate the effect of far field tsunami in a limited area model domain where the coastal and Island boundaries are curvilinear in nature and the bending is high. The model is designed in a boundary fitted curvilinear grid system. To simulate the effect of far field tsunami, it is considered that the tsunami source is located far away from the model domain. The coastal and island boundaries and the other open boundaries of the model domain are represented by some functions so as to generate the boundary fitted grids. To use the regular finite difference scheme a transformation is used so that the physical domain is transformed into a rectangular one. The transformed shallow water equations are then solved in the transformed domain. The response of the tsunami source due to 26 December 2004 Indonesian tsunami is computed along the western open boundary of the model domain. Based on the response of the tsunami source, an appropriate boundary condition is formulated to simulate the effect of far field tsunami along the coastal belt. All simulations show excellent agreement with the observed data.

Key Words: *Boundary-fitted curvilinear grids, Open boundary condition, Far field tsunami, Shallow water equations, Tsunami source, Indonesian tsunami 2004.*

1. INTRODUCTION

The mega earthquake of 26 December 2004 with magnitude 9.3 occurred off the west coast of northern Sumatra of Indonesia and triggered a devastating tsunami. The tsunami waves spread across the Indian Ocean impacting and causing damage to the shores of more than a dozen countries throughout south and south east Asia. The catastrophic tsunami causes devastating damage not only on shores of neighboring countries but also on shores of more distant countries. It was clearly recorded by a large number of tide gauges throughout the world ocean, including tide gauges located in the North Pacific and North Atlantic (Rabinovich et al., 2006).

Tsunamis are called local, regional and far field or distant if the distances of the source are within 100 km, 100 – 700 km, and more than 700 km respectively from the coast. The three phases of a tsunami: generation, propagation and run-up are equally important for the accurate simulation of water levels in the coastal area for a near field or a local tsunami. But for distant tsunami the propagation phase becomes more important, since the time required for propagation is much longer than those for other phases (Yoon, 2002). However, the effect of a tsunami source along a particular coastal area far away from the region of interest may be significant if the waves move through deep Ocean. Since the response of the 2004 Indonesian tsunami reached every distant corner of the globe, it is necessary to estimate the response along a particular region due to a source located far away from that region. This may be done through a global model that contains both the source and the region of interest.

Kowalik et al. (2005) developed a global model to simulate the tsunami wave characteristics along the coastal belts throughout the globe associated with 2004 Indonesian tsunami. Arcas and Titov (2006) computed a worldwide tsunami propagation simulation of Sumatran tsunami of 2004 to compare their computational results with the stream of tide gage data from around the globe. However a global model is very expensive in terms of both computer storage and CPU time and is not suitable for real time simulation. In hydrodynamical computations problem arises when the theoretical model applies to an infinite or semi-infinite region. In this case, where the original domain of the problem under investigation is infinite or very large, open boundaries may be used. An open boundary is an artificial boundary of a computational domain through which propagation of waves or flow should pass in order to leave the computational domain without giving rise to spurious reflection (Joolen et al. 2003). The main purpose of using the open boundaries is to enable waves and disturbances which originate from within the model domain to leave the model domain without affecting the interior solution of the mathematical model.

According to Yoon (2002), the prevention and mitigation of tsunami hazards depend on the accurate assessment of the generation, propagation and run-up of tsunamis. So, efforts should be made to construct mathematical (numerical) models. In particular regional tsunami numerical models should be developed to develop the early warning system. A number of studies have been done on modeling the Indonesian tsunami of 2004 for the west coast of Southern Thailand and Peninsular Malaysia after the event 26 December 2004 (Roy and Ismail, 2005; Roy et al., 2006; Karim et al., 2006). A lot of other researchers (e.g. Agarwal et al., 2005; Cho et al., 2007; Zahibo et al., 2006) have also modeled the 2004 Indian Ocean event. Then majority of the studies are based on depth-averaged shallow water equations and were discretized by the finite-difference Cartesian grids with the coastline represented by stair-steps. With a stair-step model the coastal boundaries are approximated

along the nearest finite difference gridlines of the numerical scheme (Roy, 1999). Though the finite difference grids with the coastline represented by stair-steps technique is often used in traditional hydrodynamic models of coastal currents like a tsunami, the computational costs have become excessive and affects the model accuracy negatively. To resolve the lateral geometry better, refined lateral grids should be used in finite difference models by using a large number of grids within the model domain (Bao et al., 2000). Since the accuracy of a stair step model depends on the grid size the grid spacing should be made small enough. So the computational costs often become excessive.

On the other hand boundary-fitted curvilinear grid systems combines the best aspects of finite-difference discretization with grid flexibility. The boundary fitted grid technique makes the equations and boundary conditions simple and better represents the complex geometry with relatively less grid points. Thus, it significantly improves the finite difference schemes (Bao et al. 2000). The use of this kind of grid system allows the user extensive control over the design of the computational mesh. However one difficulty in boundary fitted grid system is that the gridline of the numerical scheme are curvilinear and non-orthogonal. In order to apply a regular finite difference scheme the grid system must be rectangular. In a boundary-fitted model, the curvilinear boundaries are transformed into straight ones using appropriate transformations, so that in the transformed space regular finite difference techniques can be used.

Karim et al. (2007) developed a shallow water model using a boundary fitted curvilinear grid system to simulate the 2004 Indonesian tsunami along the coastal belts of Phuket and Penang. Roy et al. (2006) presented a technique to compute the effect of a far field tsunami along the coastal belts by formulating an open boundary condition where the tsunami source is removed during the far field tsunami computation. The main goal of this study is to simulate the effect of a far field tsunami along the coastal belt of Phuket and Penang Island through an open boundary condition in a boundary fitted curvilinear grid system. For this purpose the boundary fitted curvilinear grid model of Karim et al. (2007) is used as the source model to compute the response of the source of Indonesian tsunami 2004 along the western open boundary of the model. Using the technique of Roy et al. (2006) and based on the data computed from the source model, an appropriate boundary condition is formulated along the western open boundary of the boundary fitted curvilinear grid model and at the same time the tsunami source near Sumatra is removed. This boundary condition is applied in the absence of the source in the model domain to simulate the effect of far field tsunami. Thus for far field tsunami computation instead of considering a tsunami source inside the model domain, an open boundary condition is imposed as an effect of a tsunami source.

2. GOVERNING EQUATIONS AND BOUNDARY CONDITIONS

The shallow water equations, which describe the inviscid flow of a shallow fluid in two dimensions, have been used for many years testing numerical methods for solving atmospheric and oceanic problems (Haltiner and Williams, 1980). These are coupled first order non-linear hyperbolic partial differential equations and are often used governing equations approximating tsunami propagation in the deep ocean as well as in near-shore regions including inundation (Aizinger and Dawson, 2002).

The displaced position of the free sea surface from the mean sea level is considered as $z = \zeta(x, y, t)$ and the sea floor as $z = -h(x, y)$ so that, the total depth of the fluid layer is $\zeta + h$.

Following Roy (1998), the vertically integrated shallow water equations for tsunami computations are

$$\frac{\partial \zeta}{\partial t} + \frac{\partial}{\partial x} [(\zeta + h)u] + \frac{\partial}{\partial y} [(\zeta + h)v] = 0 \quad (1)$$

$$\frac{\partial u}{\partial t} + u \frac{\partial u}{\partial x} + v \frac{\partial u}{\partial y} - f v = -g \frac{\partial \zeta}{\partial x} - \frac{C_f u (u^2 + v^2)^{1/2}}{\zeta + h} \quad (2)$$

$$\frac{\partial v}{\partial t} + u \frac{\partial v}{\partial x} + v \frac{\partial v}{\partial y} + f u = -g \frac{\partial \zeta}{\partial y} - \frac{C_f v (u^2 + v^2)^{1/2}}{\zeta + h} \quad (3)$$

where u and v are the velocity components of flow particle in x and y directions, f is the Coriolis parameter, g is the acceleration due to gravity, C_f is the friction coefficient.

For numerical treatment it is convenient to express the equations (2) & (3) in the flux form by using the equation (1). The shallow water equations in flux forms are

$$\frac{\partial \zeta}{\partial t} + \frac{\partial \tilde{u}}{\partial x} + \frac{\partial \tilde{v}}{\partial y} = 0 \quad (4)$$

$$\frac{\partial \tilde{u}}{\partial t} + \frac{\partial (u\tilde{u})}{\partial x} + \frac{\partial (v\tilde{u})}{\partial y} - f \tilde{v} = -g(\zeta + h) \frac{\partial \zeta}{\partial x} - \frac{C_f \tilde{u} (u^2 + v^2)^{1/2}}{\zeta + h} \quad (5)$$

$$\frac{\partial \tilde{v}}{\partial t} + \frac{\partial (u\tilde{v})}{\partial x} + \frac{\partial (v\tilde{v})}{\partial y} + f \tilde{u} = -g(\zeta + h) \frac{\partial \zeta}{\partial y} - \frac{C_f \tilde{v} (u^2 + v^2)^{1/2}}{\zeta + h} \quad (6)$$

where, $(\tilde{u}, \tilde{v}) = (\zeta + h)(u, v)$

Here u and v in the bottom stress terms of (2) and (3) have been replaced by \tilde{u} and \tilde{v} in (5) and (6) in order to solve the equations in a semi-implicit manner. \tilde{u} and \tilde{v} are the depth-averaged volume fluxes in the x and y directions, respectively.

According to Tang and Grimshaw (1996), open boundary conditions arise in numerical simulation of coastal ocean model and they play a role in determining the validity of the result. Numerical open boundary conditions should allow fluid motions generated in the computational domain and which are left at the open boundary to pass through the boundary without influencing the interior solution. They are imposed along the edge of the model domain where the solution is unknown. Open boundaries contrast to other boundaries where the solution can be specified from data, models, or assumed. Since the solution is unknown along the open boundaries an assumption must be made or the interior solution extrapolated (Roed and Cooper, 1986). For convenience of the treatment of boundary conditions, open boundaries are usually placed along coordinate axes.

The appropriate boundary condition along the coastal boundary is that the normal component of the vertically integrated velocity vanishes at the coast and following Roy (1998) this may be expressed as:

$$u \cos \alpha + v \sin \alpha = 0 \quad \text{for all } t \geq 0 \quad (7)$$

where α is the inclination of the outward directed normal to the x -axis. It then follows that $u = 0$ along y - boundaries and $v = 0$ along the x - boundaries.

At the open-sea boundaries the waves and disturbance, generated within the model domain, are allowed to leave the domain without affecting the interior solution. Thus the normal component of velocity cannot vanish and so a radiation type of boundary is generally used. Following Heaps (1973), the following radiation type of condition may be used:

$$u \cos \alpha + v \sin \alpha = -(g/h)^{1/2} \xi \quad \text{for all } t \geq 0 \quad (8)$$

Note that the velocity structure in a shallow water wave is described by $w = \frac{g\xi}{\sqrt{gh}}$, where w is the horizontal particle velocity.

3. GENERATION OF BOUNDARY-FITTED GRIDS

The OX points are considered towards the west and OY points towards the north. The eastern coastal boundary, along y -axis, is situated at $x = b_1(y)$ and the western open-sea boundary, parallel to y -axis, is at $x = b_2(y)$. The southern open-sea boundary, along x -axis, and the northern open-sea boundary, parallel to x -axis, are at $y = 0$ and $y = L$ respectively. This configuration is shown in Fig. 1.

Following Roy (1999), the system of gridlines oriented to $x = b_1(y)$ and $x = b_2(y)$ are given by the generalized function

$$x = \{(k-l)b_1(y) + lb_2(y)\} / k \quad (9)$$

where $k = M$, the number of gridlines in x -direction and l is an integer and $0 \leq l \leq k$.

The system of gridlines oriented to $y = 0$ and $y = L$ are given by the generalized function

$$y = \{(q-p)0 + pL\} / q \quad (10)$$

where $q = N$, the number of gridlines in y -direction and p is an integer and $0 \leq p \leq q$.

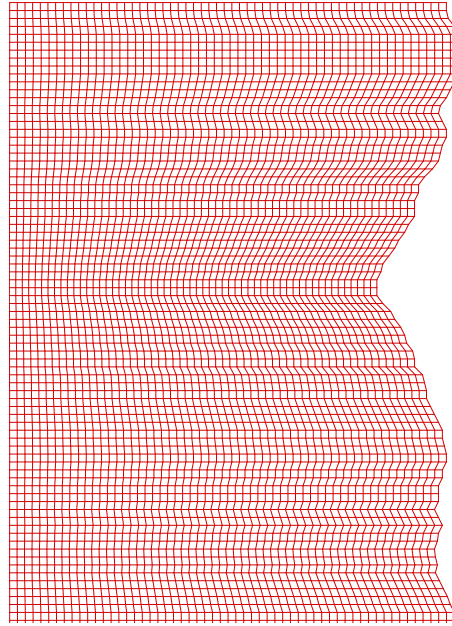


Figure 1. Boundary fitted grids in physical domain.

$$\lambda = 1$$

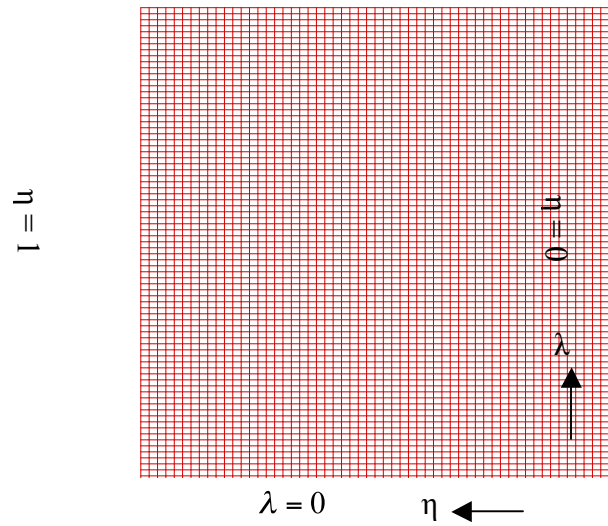


Figure 2. Transformed domain and the rectangular grid lines.

Note that equation (9) reduces to $x = b_1(y)$ and $x = b_2(y)$ for $l = 0$ and $l = k$ respectively. Similarly equation (10) reduces to $y = 0$ and $y = L$ for $p = 0$ and $p = q$ respectively. Now by proper choice of l, k and p, q the boundary-fitted curvilinear grids can be generated.

Every boundary of each island inside the model domain has been broken into several segments and every segment has been aligned either along (9) or along (10) so that the boundary of every island is aligned along the boundary fitted gridlines (Roy, 1999). The representation of the island boundaries are done this way so that the whereabouts of them have not been lost in the transformed domain. Each of the eastern and western boundaries of an island is given by (9) and each of the southern and northern boundaries of an island is given by (10).

Since $l = 0$ implies $x = b_1(y)$ or $\eta = 0$, the coastal boundary and $l = k$ implies $x = b_2(y)$ or $\eta = 1$, the open boundary, equation (9) with two different values of l , say, l_1 and l_2 with $l_1 < l_2$ will express the eastern and western boundaries of an island. Similarly equation (10) with two different values of p , say p_1 and p_2 with $p_1 < p_2$ will express the south and north boundaries of the island. Thus the transformed boundaries of an island are expressed as

$$\eta = l_1 / k, \eta = l_2 / k, \lambda = p_1 / q, \lambda = p_2 / q \quad (11)$$

For $x = b_1(y)$, the boundary condition (7) may be simplified as $u + v \tan \alpha = 0$, which gives $u - v \frac{dx}{dy} = 0$, that yields $u - v \frac{db_1}{dy} = 0$. Therefore, following Johns et al. (1981), the boundary conditions are given by

$$u - v \frac{db_1}{dy} = 0 \quad \text{at } x = b_1(y), \text{ along } x\text{-axis} \quad (12)$$

$$u - v \frac{db_2}{dy} = (g/h)^{1/2} \xi \quad \text{at } x = b_2(y), \text{ parallel to } y\text{-axis} \quad (13)$$

$$v + (g/h)^{1/2} \xi = 0 \quad \text{at } y = 0, \text{ along } x\text{-axis} \quad (14)$$

$$v - (g/h)^{1/2} \xi = 0 \quad \text{at } y = L, \text{ parallel to } x\text{-axis} \quad (15)$$

4. COORDINATE TRANSFORMATION

To facilitate the numerical treatment of an irregular boundary configuration, a transformation of coordinates used is. The transformation is similar to that in Johns et al. (1985), which is based upon new set independent variables η, λ, y, t where

$$\eta = \frac{x - b_1(y)}{b(y)}, \quad \lambda = \frac{y}{L}, \quad b(y) = b_2(y) - b_1(y). \quad (16)$$

This mapping transforms the analysis area enclosed by $x = b_1(y), x = b_2(y), y = 0$ and $y = L$ into a rectangular domain given by $0 \leq \eta \leq 1, 0 \leq \lambda \leq 1$ (Fig. 2).

The generalized function (9) takes the form $b\eta + b_1 = \{(k-l)b_1(y) + lb_2(y)\}/k$, which can be written as $\eta = \frac{l(b_2 - b_1)}{bk}$ and this gives

$$\eta = \frac{l}{k}. \quad (17)$$

The generalized function (10) takes the form $\lambda L = \{(q-p)y + pL\}/q$, which gives

$$\lambda = \frac{p}{q}. \quad (18)$$

For $l = 0$, we have the eastern coastal boundary $\eta = 0$ or $x = b_1(y)$ and for $l = k$, we have the western open-sea boundary $\eta = 1$ or $x = b_2(y)$. Similarly, for $p = 0$, we have the southern open sea boundary $\lambda = 0$ or $y = 0$ and for $p = q$ we have the northern open-sea boundary $\lambda = 1$ or $y = L$. Thus by the proper choice of the constants k and q and the parameters l and p , rectangular grid system can be generated in the transformed domain.

5. TRANSFORMED SHALLOW WATER EQUATIONS AND BOUNDARY CONDITIONS

By using the transformations (16),

$$\frac{\partial}{\partial x} \equiv \frac{1}{b} \frac{\partial}{\partial \eta} \quad (19)$$

$$\frac{\partial}{\partial y} \equiv -\frac{1}{b} \left(\frac{db_1}{dy} + \eta \frac{db}{dy} \right) \frac{\partial}{\partial \eta} + \frac{1}{L} \frac{\partial}{\partial \lambda} \quad (20)$$

Taking η, λ, y, t as the new independent variables and using the relations (19) and (20), the equations (4) – (6) transform to (by Karim et al., 2007)

$$\frac{\partial(bL\xi)}{\partial t} + \frac{\partial \tilde{U}}{\partial \eta} + \frac{\partial \tilde{V}}{\partial \lambda} = 0 \quad (21)$$

$$\frac{\partial \tilde{u}}{\partial t} + \frac{\partial(U\tilde{u})}{\partial \eta} + \frac{\partial(V\tilde{u})}{\partial \lambda} - f\tilde{v} = -gL(\xi + h) \frac{\partial \xi}{\partial \eta} - \frac{C_f \tilde{u} (u^2 + v^2)^{1/2}}{\xi + h} \quad (22)$$

$$\frac{\partial \tilde{v}}{\partial t} + \frac{\partial(U\tilde{v})}{\partial \eta} + \frac{\partial(V\tilde{v})}{\partial \lambda} + f\tilde{u} = -g(\xi + h) \left[b \frac{\partial \xi}{\partial \lambda} - L \left(\frac{db_1}{dy} + \eta \frac{db}{dy} \right) \frac{\partial \xi}{\partial \eta} \right] - \frac{C_f \tilde{v} (u^2 + v^2)^{1/2}}{\xi + h} \quad (23)$$

where, $U = \frac{1}{b} \left[u - \left(\frac{db_1}{dy} + \eta \frac{db}{dy} \right) v \right]$, $V = \frac{v}{L}$, $(\tilde{u}, \tilde{v}, \tilde{U}, \tilde{V}) = bL(\xi + h)(u, v, U, V)$

At $x = b_1(y)$ i.e. at $\eta = 0$, $U = \frac{1}{b} \left[u - \left(\frac{db_1}{dy} + \eta \frac{db}{dy} \right) v \right] = \frac{1}{b} \left[u - \frac{db_1}{dy} v \right] = 0$.

And at $x = b_2(y)$ i.e. at $\eta = 1$, $U = \frac{1}{b} \left[u - \left(\frac{db_1}{dy} + 1 \cdot \frac{db}{dy} \right) v \right] = \frac{1}{b} \left[u - \frac{db_2}{dy} v \right]$, which gives

$$bU = u - \frac{db_2}{dy} v.$$

Therefore the boundary conditions (12) – (15) reduces to

$$U = 0 \quad \text{at } \eta = 0 \quad (24)$$

$$bU - (g/h)^{1/2} \xi = 0 \quad \text{at } \eta = 1 \quad (25)$$

$$VL + (g/h)^{1/2} \xi = 0 \quad \text{at } \lambda = 0 \quad (26)$$

$$VL - (g/h)^{1/2} \xi = 0 \quad \text{at } \lambda = 1 \quad (27)$$

At each boundary of an island, the normal component of the velocity vanishes. Thus, the boundary conditions of an island are given by

$$U = 0 \quad \text{at } \eta = l_1/k \text{ and } \eta = l_2/k \quad (28)$$

$$V = 0 \quad \text{at } \lambda = p_1/q \text{ and } \lambda = p_2/q \quad (29)$$

6. GRID GENERATION IN TRANSFORMED DOMAIN WITH FINITE DIFFERENCE SCHEME

Since the analysis area or the physical domain is transformed into a rectangular one, the rectangular grid system is generated in the analysis area using a set of equidistant straight lines parallel to η -axis and a set of equidistant straight lines parallel to λ -axis. The space between any two consecutive gridlines parallel to λ -axis is $\Delta\eta$ and that between any two consecutive gridlines parallel to η -axis is $\Delta\lambda$. Let there be M gridlines parallel to λ -axis and N gridlines parallel to η -axis. So, there are M grid points in η -direction and N grid points in λ -direction and the total number of grid points is $M \times N$.

We define the grid points (η_i, λ_j) in the domain by

$$\eta_i = (i - 1)\Delta\eta, \quad i = 1, 2, 3, \dots, M \quad (30)$$

$$\lambda_j = (j - 1)\Delta\lambda, \quad j = 1, 2, 3, \dots, N \quad (31)$$

The sequence of discrete time instants is given by

$$t_k = k \Delta t, \quad k = 1, 2, 3, \dots \quad (32)$$

A staggered grid system, similar to Arakawa C system (Arakawa and Lamb, 1977), is used in the transformed domain where there are three distinct types of computational points. These three types of points are defined as follows: For every discrete grid point (η_i, λ_j) , if i even and j odd, the point is a ζ -point at which ζ is computed. If i is odd and j is odd, the point is a u -point at which u is computed. If i is even and j is even, the point is a v -point at which v is computed. In a staggered grid system, since every dependent variable is computed at any one of these three types of points rather than at every point, the CPU time is reduced. Moreover, a staggered grid system is favorable in filtering out sub-grid scale oscillations.

The transformed shallow water equations (21) - (23) together with the boundary conditions (25) - (27) are discretized by finite difference (Forward Time Centered Space) and are solved by a conditionally stable semi-implicit method.

The η -axis is directed towards west at an angle 15° (anticlockwise) with the latitude line and the λ -axis is directed towards north inclined at an angle 15° (anticlockwise) with the longitude line. In this model the analysis area is extended from 2° N to 14° N latitudes (incorporating the west coasts of Malaysia including Penang and Southern Thailand including Phuket) and 91° E to 101.5° E longitudes (Fig. 3).

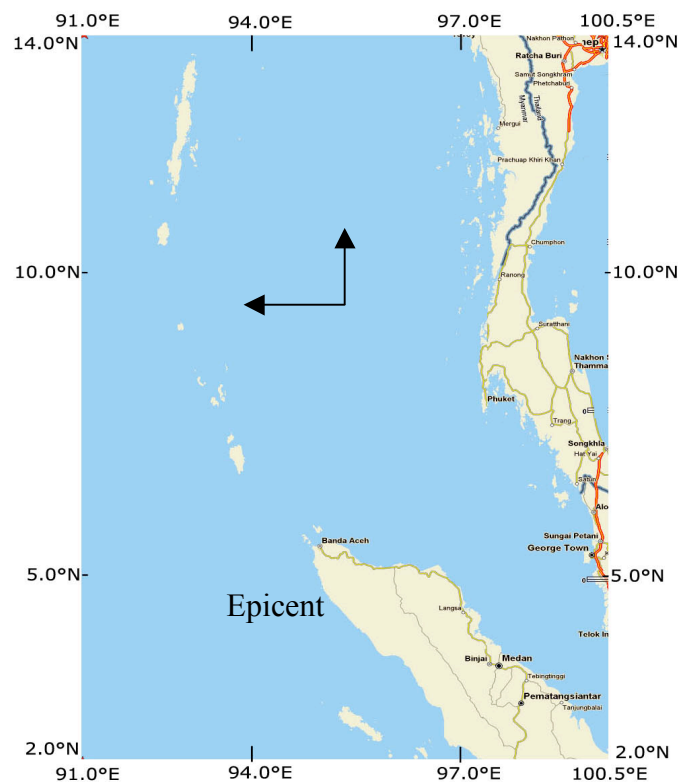


Figure 3. Model Domain including the coastal geometry and the epicenter of the 2004 earthquake (Courtesy: Roy et al., 2006).

The number of grids in η and λ - directions are respectively $M = 230$ and $N = 319$. The model area includes the source region of Indonesian tsunami 2004. On the ocean boundary, radiation condition, in which the tsunami wave is assumed to go out without changing its shape, is assumed. For the land boundary (i.e the coast), it is assumed there is total reflection. The coastal boundary is fixed; i.e. we assume no run-up on the land. The time step of computation is determined to satisfy the stability condition. It is set to 10 s in this computation. Following Kowalik et al. (2005), the value of the friction coefficient C_f is taken as 0.0033 through out the model area. The available depth data for some representative grid points of the model area are collected from the Admiralty bathymetric charts. The depth at the entire rest grid points of the mesh are computed by some averaging process. The bathymetry of the modal domain is shown in the Fig. 4.

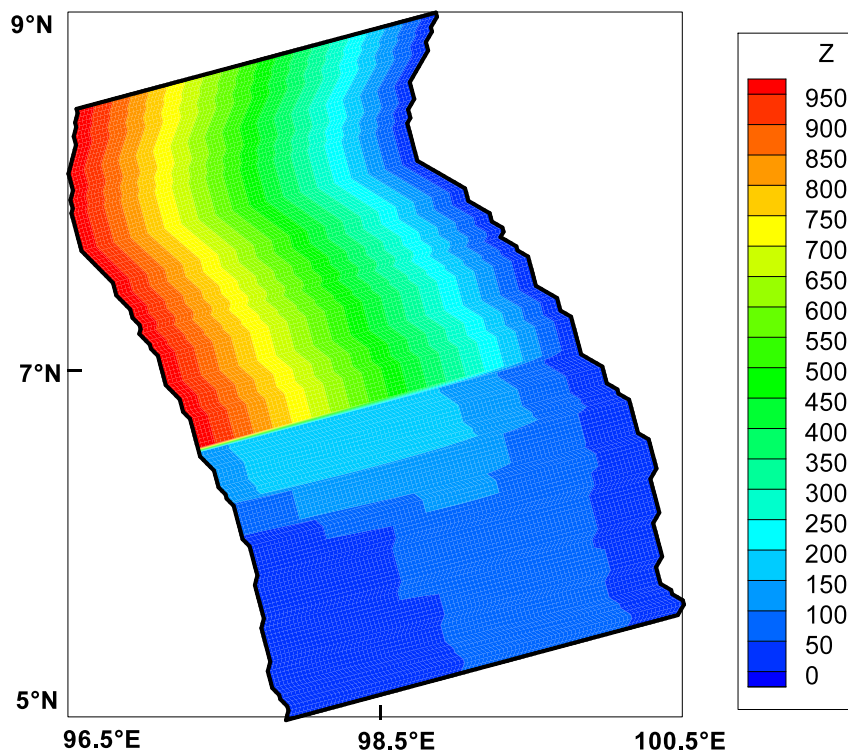


Figure 4. Bathymetry used in the numerical simulation (depth unit: m).

7. TSUNAMI SOURCE GENERATION AND INITIAL CONDITIONS

For tsunami computation initialization of model geometry, various parameters and variables is required first. The tsunami generation is modelled by the initialisation of the water surface. The generation of an earthquake tsunami source depends essentially on the pattern and dynamics of motions in the earthquake source zone and on the initial seafloor movements. The generation mechanism of the 2004 Indonesian tsunami was mainly a static sea floor uplift caused by an abrupt slip at the India/Burma plate interface. A detailed description of the estimation of the extent of the earthquake rupture as well

as the maximum uplift and subsidence of the seabed is given in Kowalik et al. (2005) and this estimation is based on seismological methods in Okada (1985). From the deformation contour, it was concluded that the estimated uplift and subsidence zone is between 92° E to 97°E and 2°N to 10°N with a maximum uplift of 507 cm at the west and maximum subsidence of 474 cm at the east. The uplift to subsidence is approximately from west to east relative to the west coasts of the Malaysian Peninsula and Thailand. The major force of tsunamis is the vertical displacement of the seafloor. For computational purposes tsunami models are often initialized by a sea-surface displacement. We can assume that the initial value of the sea surface displacement that starts a tsunami is the same as the vertical displacement of the sea floor (Arreaga-Vargas et al., 2005; Aida, 1974), due to incompressibility of the ocean water. The assumption is taken with an instantaneous source approximately with the length of the rupture zone (the area covered by the initial aftershock distribution). Following Kowalik et al. (2005) the disturbance in the form of rise and fall of sea surface is assigned as the initial condition in the source model with a maximum rise of 5 m to maximum fall of 4.75 m to generate the response of the tsunami along the western open boundary of the model domain. In all other regions of the domain the initial sea surface deviations are taken as zero. Also the initial x - and y -components of the velocity are taken as zero throughout the model area.

8. OPEN BOUNDARY CONDITION FOR FAR FIELD TSUNAMI COMPUTATION

The time series of the sea surface fluctuation and amplitude of the source of Indonesian tsunami 2004 along the western open boundary of the model has been computed. To simulate the far field tsunami or to investigate the effect of a far field tsunami it is considered that the tsunami source is located far away from the model domain. The amplitudes of tsunami wave along the western open boundary as the response of the source has been computed to estimate the amplitude of the boundary condition by which far field tsunami will be computed in absence of the source.

For generating tidal oscillation in a limited area model through a boundary, the open boundary condition is generally formulated by associating a sinusoidal term, containing amplitude, period and phase, with the radiation type of boundary condition (Johns et al., 1985; Roy, 1995) and this is described as

$$u - \sqrt{g/h} \xi = -2\sqrt{g/h} a \sin(2\pi t/T + \varphi), \text{ at } x = b_2(y) \quad (33)$$

where a is the amplitude, T is the period, φ is the phase of the wave. But for tsunami propagation the time series is oscillatory with damping amplitude. On the basis of time series data and amplitude, the open boundary condition that represents the effect of far field tsunami for the boundary fitted curvilinear model is (Roy et al., 2006)

$$bU - \sqrt{g/h} \xi = -2\sqrt{g/h} e^{(-st)} a \sin(2\pi t/T + \varphi), \text{ at } x = b_2(y) \quad (34)$$

where s is the scale factor used for damping the amplitude of the wave with respect to time. In equation (34), the following conditions are imposed:

$$s = 0 \quad \text{for } t \leq T \quad \text{and} \quad s > 0 \quad \text{for } t > T.$$

Through this condition we are allowing one wave, with full amplitude, to enter into the domain through the open boundary before damping of the amplitude begins.

The assigned amplitudes (a) in (34) are adjusted so that the response of the boundary condition in model domain is similar to that associated with the source of Indonesian tsunami 2004. By trial and error method, the values of phase (φ), period (T) and the scale factor in equation (34) have also been adjusted and these are $\varphi = 0$, $T = 0.5$ hr and $s = 0.01$. Fig. 5 shows the time series of sea surface fluctuation at (230, 155) th grid point at the western open boundary due to the source of Indonesian tsunami 2004 and the boundary condition. Both the time series are found to be almost identical, which means that the boundary condition is capable of generating time series which is similar to that generated by the source.

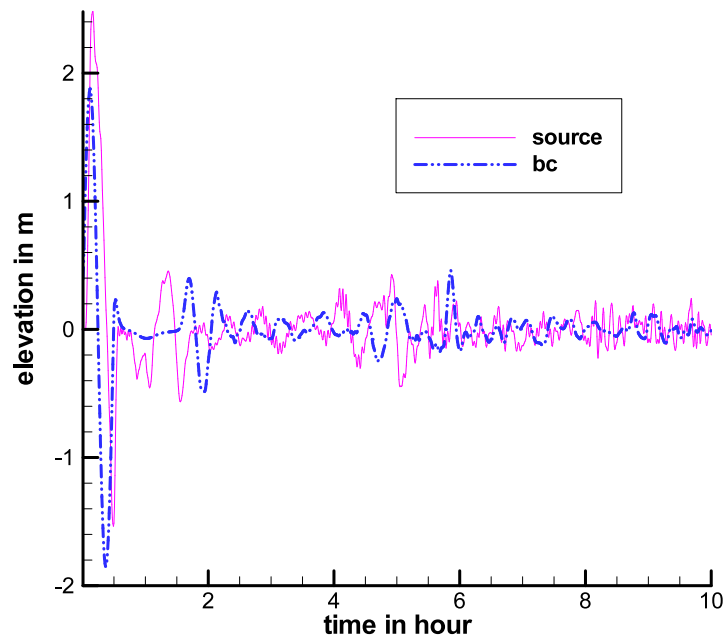


Figure 5. Time series of sea surface fluctuation at the western open boundary.

9. SIMULATION OF 2004 TSUNAMI THROUGH THE OPEN BOUNDARY CONDITION

In this section, the propagation of water waves generated by the open boundary condition without considering the tsunami source of 2004 Indian ocean earthquake inside the model domain is studied. Tsunami travel time towards the two coastal locations and the time series of water elevation due to the open boundary condition are also presented. Finally, the contour of the maximum water level at different coastal locations is also presented. The computed results are compared with those recorded and observed data.

The arriving time of tsunami at the coast has been studied. Fig. 6 shows the contour plot of time, in minutes, for attaining +0.1 m sea level rise at each grid point in the model domain. Thus considering the 0.1 m sea level rise as the arrival of tsunami, it is seen that after imposition of the boundary condition, the disturbance propagates gradually towards the coast. The arrival time of tsunami due to the boundary condition at Phuket is 150 min and the same at Penang is approximately 270 min. If the source is considered within the model domain, the arrival time of tsunami from the source at Phuket and Penang islands are 110 min and 240 min respectively (Karim et al., 2007). In the present study the response of the open boundary condition imposed at the west boundary has been computed, which is away from the source zone of the Indonesian tsunami 2004. This is why the computed arrival time is delayed by up to 30 to 40 min compared to the arrival time when the source is considered within the model domain. This time difference can be estimated by measuring the total distance of the open boundary from the coast and tsunami travel time due to the boundary condition. Thus the corrected time related to the tsunami source at Sumatra should be 30 to 40 min earlier than the present computed time. In the USGS website it is reported that the tsunami waves reached at Phuket within two hours time after the earthquake and the arrival time of tsunami at Penang is between 3 hr 30 min and 4 hours. Thus the tsunami travel time along the coastal and island boundaries of Phuket and Penang computed by the open boundary condition agree well with the data available in the USGS website.

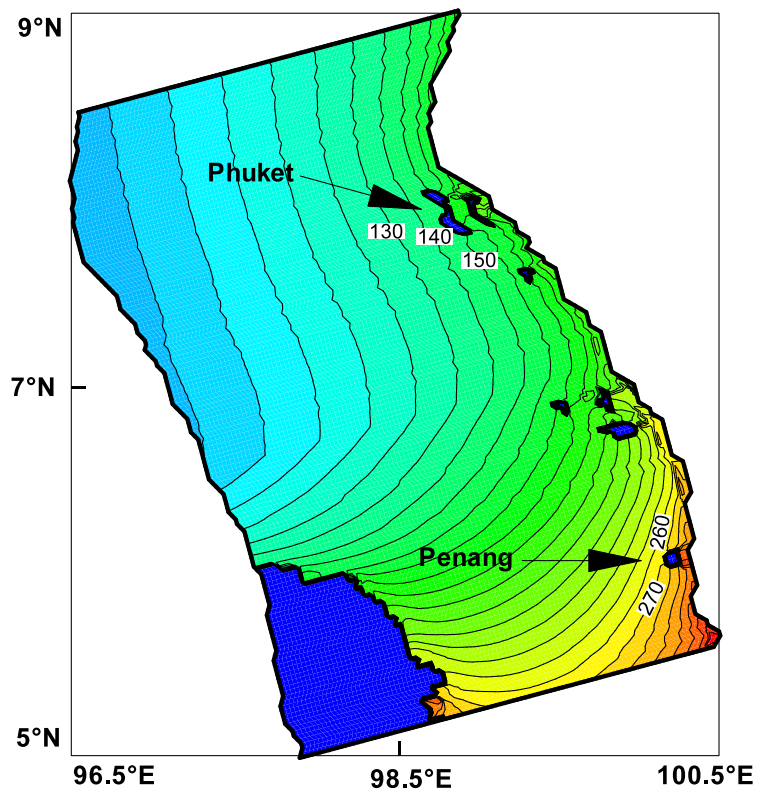


Figure 6. Tsunami propagation time in minutes towards Phuket and Penang due to the boundary condition.

Fig. 7 depicts the maximum water level contours, along the coast from Penang Island to Phuket. The surge amplitude is increasing from south to north; the maximum water level at Penang Island is from 2 m to 4 m, whereas the same at Phuket region is 6 m to 11 m. The computed water levels indicate that the north and west coasts of Penang Island and the north-west part of Phuket are at risk of highest surge due to the source at Sumatra. The maximum coastal surge estimated by the boundary condition varies from 18 - 20 m in some locations located approximately 50 km north from the Phuket. Tsuji et al. (2006) reported that the largest tsunami height reached up to 19.6 m at Ban Thung Dap located at 50 km north from the Phuket. Thus the model result shows a quite good agreement with the study of Tsuji et al. (2006) for the Phuket region.

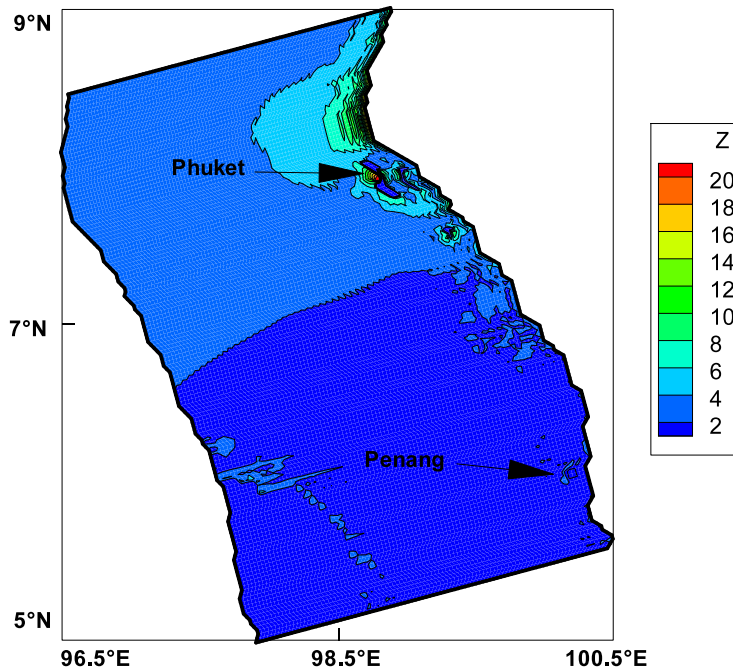


Figure 7. Contour of maximum water elevation due to the boundary condition around the west coast of Thailand and Malaysia.

The computed water levels at different locations of the coastal belt of Phuket and Penang Island are stored at an interval of 30 seconds. Fig. 8 depicts the time series of water levels for the Phuket region in south west Thailand. At the west coast of Phuket, the maximum water level is 6.5 m and the water level continues to oscillate for long time (Fig. 8a). At the south coast of Phuket the time series begins with a depression of -3.7 m and the maximum water level reaches up to 4.1 m and the oscillation continues with low amplitudes (Fig. 8b). Fig. 9 shows the similar results at two locations at the north and north-east coasts of Penang Island in Malaysia. At Batu Ferringi (north coast) the maximum elevation is approximately 3.2 m (Fig. 9a). At the location Tanjung Tokong (north-east coast) the maximum elevation is approximately 3.2 m (Fig. 9b). Simulations are also taken out (not shown in the figure) for the other coast locations of Phuket and Penang. The computed results show that, the west coast of Phuket and the north and north-west coasts of Penang Island are vulnerable for stronger tsunami surges.

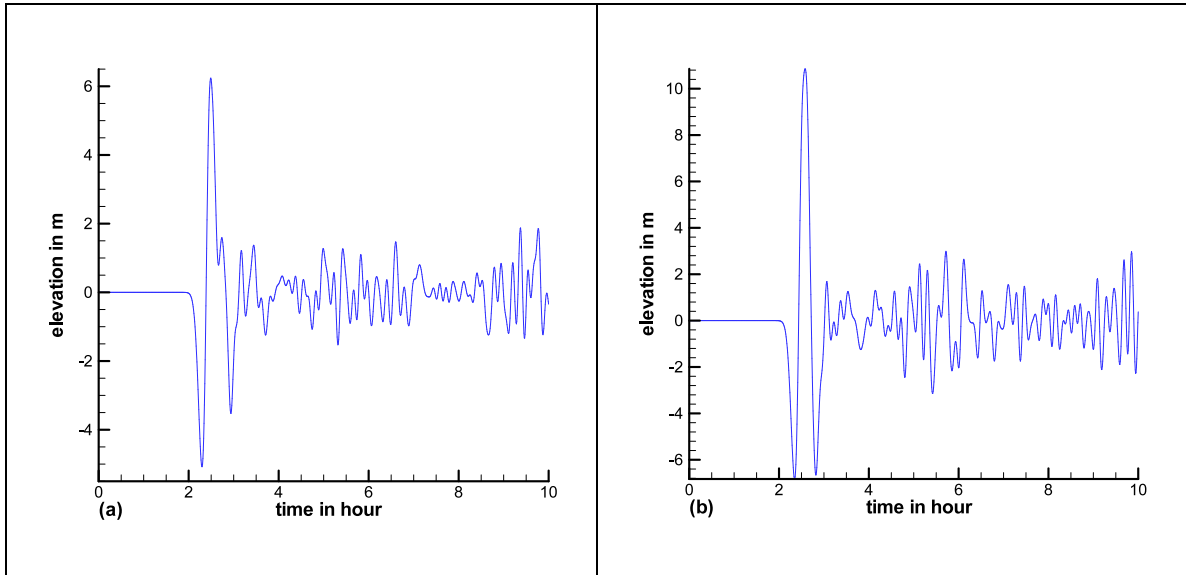


Figure 8: Time series of computed elevation at coastal locations of Phuket: (a) West Phuket,(b) South Phuket.

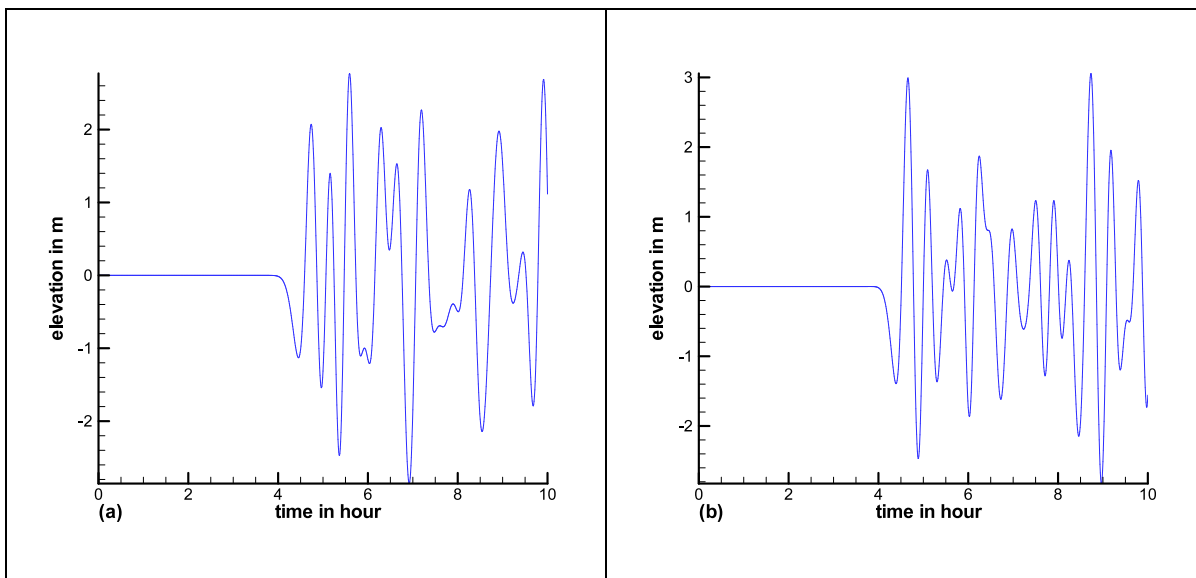


Figure 9: Time series of computed elevation at coastal locations of Penang Island: (a) Batu Ferringhi (b) Tanjung Tokong.

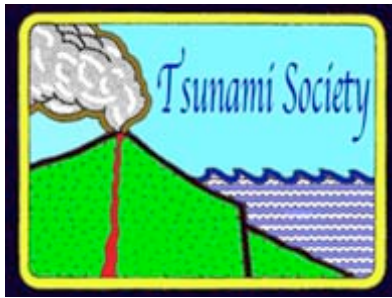
10. CONCLUSIONS

The effect of far field tsunami along the coastal belt of the west coast of Peninsular Malaysia and southern Thailand has been described. A detailed description of the generation of boundary fitted curvilinear grids and the formulation of the boundary condition on this boundary fitted curvilinear grid system is carried out. The tsunami source was removed during the simulation of the far field tsunami along the coastal belts through the open boundary condition. Comparisons between the recorded and simulated waves have been made at two coastal locations of Phuket of Thailand and Penang of Malaysia and good agreement has been found in water elevation. There is a time lag in tsunami propagation time due to the tsunami source and the boundary condition. This time difference can be estimated by measuring the total distance of the open boundary from the coast and tsunami propagation time. So the authors do believe that this approach of simulating far field tsunami can be applied in a limited area model domain where the coastal belts are curvilinear and the bending is high.

REFERENCES

- Agarwal, V. K., Agarwal, N. & Kumar, R. (2005). Simulations of the 26 December 2004 Indian Ocean tsunami using a multi-purpose Ocean disaster simulation and prediction model. *Current Science*, 88(3), 439 - 444.
- Aida, I. (1974). Numerical Computation of a Tsunami Based on a Fault Origin Model of an Earthquake. *J. Seismol. Soc. Japan*, 27, 141-154.
- Aizinger, V., & Dawson, C. (2002). A discontinuous Galerkin method for two-dimensional flow and transport in shallow water. *Advances in Water Resources*, 25(1), 67-84.
- Arakawa, A., & Lamb, V. (1977). Computational design of the basic dynamical processes of the UCLA general circulation model. In J. Chang (Ed.), *Methods in Computational Physics* (Vol. 7, pp. 173-265). New York: Academic Press.
- Arcas, D., & Titov, V. (2006). Sumatra tsunami: lessons from modeling. *Surv Geophys*, 27, 679 - 705.
- Arreaga-Vargas, P., Ortiz, M. & Farreras, S.F. (2005). Mapping the Possible Tsunami Hazard as the First Step Towards a Tsunami Resistant Community in Esmeraldas, Ecuador. In K. Satake (Ed.), *Tsunamis: Case Studies and Recent Developments* (pp. 203 - 215). Netherlands: Springer.
- Bao, X.W., Yan, J. & Sun, W. X. (2000). A Three-dimensional Tidal Model in Boundary-fitted Curvilinear Grids. *Estuarine, Coastal and Shelf Science*, 50, 775-788.
- Berkman, S. C., & Symons, J.M. (1964). *The tsunami of May 22, 1960 as recorded at tide gauge stations*. Washington, D.C.: U.S. Department of Commerce, Coast and Geodetic Survey.
- Cho, Y.-S., Sohn, D.H. & Lee, S.O., (2007). Practical modified scheme of linear shallow-water equations for distant propagation of tsunamis. *Ocean Engineering*, 34, 1769 – 1777.
- Haltiner, G. J., & Williams, R.T. (1980). *Numerical Prediction and Dynamic Meteorology*. New York: Wiley.
- Heaps, N. S. (1973). A three dimensional numerical model of the Irish Sea. *Geophysics. J. Astron. Soc.*, 35, 99 - 120.
- Indian Ocean Tsunami at Syowa Station Antarctica. (2007). Retrieved 10 April, 2007, from http://www1.kaiho.mlit.go.jp/KANKYO/KAIYO/KOUHOU/iotunami/iotunami_eng.html
- Johns, B., Dube, S.K., Mohanti, U.C., & Sinha, P.C. (1981). Numerical Simulation of surge generated by the 1977 Andhra cyclone. *Quart. J. Roy. Soc. London* 107, 919 – 934.

- Johns, B., Rao, A.D., Dube, S.K. & Sinha, P.C. (1985). Numerical modelling of tide–surge interaction in the Bay of Bengal. *Philos. Trans. R. Soc. London Ser. A*, 313, 507–535.
- Joolen, V., Givoli, D., & Neta, B. (2003). High-order Non-reflecting Boundary conditions for Dispersive Waves in Cartesian, Cylindrical and Spherical Coordinate Systems. *International Journal of Computational Fluid Dynamics*, 17(4), 263 - 274.
- Karim, M. F., Roy, G.D., Ismail, A. I. M. & Meah, M.A. (2006). A Linear Cartesian Coordinate Shallow Water Model for Tsunami Computation along the West coast of Thailand and Malaysia. *International Journal of Ecology & Development*, 4(S06), 1 - 14.
- Karim, M. F., Roy, G.D., Ismail, A. I. M. & Meah, M.A. (2007). A Shallow Water Model for Computing Tsunami along the West Coast of Peninsular Malaysia and Thailand Using Boundary- Fitted Curvilinear Grids, *Science of Tsunami Hazards*, 26 (1), 21 – 41.
- Kowalik, Z., Knight, W., & Whitmore, P. M. (2005). Numerical Modeling of the Tsunami: Indonesian Tsunami of 26 December 2004. *Sc. Tsunami Hazards*, 23(1), 40 – 56.
- Murty, T. S. (1977). *Seismic Sea Waves – Tsunamis*. Ottawa: Bull. Fish. Res. Board Canada.
- Okada, Y. (1985). Surface Deformation due to Shear and Tensile Faults in a Half Space. *Bull, Seism. Soc. Am.*, 75, 1135 - 1154.
- Rabinovich, A. B., Thomson, R.E. & Stephenson, F.E. (2006). The Sumatra tsunami of 26 December 2004 as observed in the North Pacific and North Atlantic oceans. *Surveys in Geophysics*, 27, 647 – 677.
- Roed, L. P., & Cooper, C.K. (1986). Open boundary conditions in numerical ocean models. In J. J. O'Brien (Ed.), *Advanced Physical Oceanographic Numerical Modeling*: D. Reidel Publishing.
- Roy, G. D. (1995). Estimation of maximum water level along the Meghna estuary using a tide and surge interaction model. *Environment International*, 21(5), 671 - 677.
- Roy, G. D. (1998). *Mathematical Modeling of Tide, Surge and their Interaction along the Coast of Bangladesh*. Paper presented at the Mini-Workshop on Appl. Math., SUST, Sylhet, Bangladesh.
- Roy, G. D. (1999). Inclusion of Off-shore Islands in a Transformed coordinates Shallow Water Model along the Coast of Bangladesh *Environment International*, 25(1), 67 - 74.
- Roy, G. D., & Ismail, A. I. M. (2005). *An investigation of 26 December 2004 tsunami waves towards the west coast of Malaysia and Thailand using a Cartesian coordinates shallow water model*. Paper presented at the Int. Conf. Math. & Applications, Mahidol University, Thailand.
- Roy, G. D., Karim, M. F., & Ismail, A. M. (2006). Numerical Computation of Some Aspects of 26 December 2004 Tsunami along the West Coast of Thailand and Peninsular Malaysia Using a Cartesian Coordinate Shallow Water Model. *Far East J. Appl. Math.*, 25(1), 57-71.
- Tang, Y., & Grimshaw, R. (1996). Radiation Boundary Conditions in Barotropic Coastal Ocean Numerical Models. *Journal of Computational Physics*, 123, 96 - 110.
- Tsuji, Y., Namegaya, Y., Matsumoto, H., Iwasaki, S.-I., Kanbua, W., Sriwichai, M. & Meesuk, V. (2006). The 2004 Indian tsunami in Thailand: Surveyed runup heights and tide gauge records. *Earth Planets Space*, 58(2), 223-232.
- Yoon, S. B. (2002). Propagation of distant tsunamis over slowly varying topography, *Journal of Geophysical Research*, 107, 1 – 11.
- Zahibo, N., Pelinovsky, E., Talipova, T., Kozelkov, A. & Kurkin, A. (2006). Analytical and numerical study of nonlinear effects at tsunami modeling. *Applied Mathematics and Computation*, 174(2), 795 - 809.



SCIENCE OF TSUNAMI HAZARDS

Journal of Tsunami Society International

Volume 31

Number 1

2012

THE SAMOA TSUNAMI OF 29 SEPTEMBER 2009 Early Warning and Inundation Assessment

Giovanni Franchello^{1*}, Alessandro Annunziato¹

¹European Commission, Joint Research Centre, Institute for the Protection and Security of the Citizen, TP 680, Via E. Fermi, 2749, I-21027 Ispra (VA), Italy

*Corresponding author, e-mail: giovanni.franchello@jrc.ec.europa.eu

ABSTRACT

On 29 September 2009 at 17:48:11 UTC, a large earthquake of magnitude 8 struck off-shore of the Samoa Islands and generated a large tsunami that destroyed several villages and caused more than 160 fatalities. This report first presents the characteristics of the earthquake and discusses the best estimations for the fault parameters, which are the necessary input data for the hydrodynamic tsunami calculations. Then, the assessment of the near-real time systems invoked by the Global Disasters Alert and Coordination System (GDACS)1 and the post-event calculations are performed, making comparisons with the observed tidal measurements and post-event survey. It was found that the most severely damaged locations are the Southern section of the Western Samoa Islands, Tutuila Isl in American Samoa and Niutoputapu Isle in Tonga. This is in agreement with the locations indicated by the Red Cross as the most affected and with the results of the post-tsunami surveys. Furthermore, an attempt was made to map the inundation events using more detailed digital elevation models (DEM) and hydrodynamic modelling with good results. The flooded areas for which we had satellite images and post-tsunami surveys confirm the inundated areas identified correctly by the hydrodynamic model. Indications are given on the DEM grid size needed for the different simulations.

Key words: *GDACS; 2009 Samoa tsunami, tsunami propagation and inundation; early warning system; fault model; DEM assessment*

Science of Tsunami Hazards, Vol. 31, No. 1, page 19 (2012)

¹ <http://www.gdacs.org/>

1. INTRODUCTION

On 29 September 2009 at 17:48:11 UTC a large earthquake of magnitude 8 struck offshore of the Samoa Islands and generated a large tsunami that destroyed several villages and caused more than 160 fatalities.

The Joint Research Centre of the European Commission has developed an impact tsunami calculation system that is invoked automatically by the Global Disasters Alert and Coordination System (GDACS) when needed. During the Samoa event, the system was repeatedly activated when increasingly accurate information on the earthquake became available. Calculations are triggered when new parametric data (magnitude, depth and location) are published by seismological organizations (e.g. USGS, EMSC, GEOFON or others). The automatic system successfully identified the risk of a large event for the Samoa islands and its initial impact calculations were available online in less than 20 minutes after the earthquake event.

One day after the event, USGS published² the Global CMT Project Moment Tensor Solution for the earthquake and a day later the Finite Fault Model solution. The latter represents the best solution for the reconstruction of the initial fault form. This report shows the initial calculations, automatically performed by the JRC Tsunami Calculation System and the enhanced calculations performed in the days after the event, when the Finite Fault Model solution became available. Calculation accuracy is evaluated by quantifying the discrepancy between sea level measurements and the initial (near-real time) calculations, and more detailed follow-up calculations.

It is important, however, to underline that there are several types of calculations and each of them has its own merit and needs.

- *Grid scenario pre-calculations.* These are performed before an event for all likely tsunami scenarios (key parameters are epicentre and magnitude, more details will be presented in the next section) and stored in a database. General (conservative) assumptions on the fault mechanism are made. The nodalisation is deliberately rather coarse (cell size between 2 and 8 km) to shorten the calculation time and to limit the data volume. GDACS look up the scenario results in the database and use the estimated maximum sea level in the alerting logic.
- *Near-real time calculations.* They are automatically performed 15-20 min after the event as far as the information on the event became available. The fault mechanism at this stage is not well defined (therefore conservative assumptions must be made) and the position and depth of the earthquake epicentre are not precise at the beginning. The nodalisation is still rather coarse (as for the grid scenario calculation) to shorten the calculation time. The objective of these calculations is the identification of the likely locations under threat of inundation without intending to exactly predict the height in all these locations.
- *Post event calculations.* These are performed from 1-2 hours to several days after an event when more information becomes available on 1) the actual fault mechanism and 2) the measured tsunami waves and inundation zones. The simulation accuracy becomes more detailed, depending on the objective of the simulations and on the available DEM. The identified objectives are the following:

² <http://earthquake.usgs.gov/eqcenter/eqinthenews/2009/us2009mdbi/#scitech>

- *Alert assessment.* The objective here is to assess the tsunami predicted by the conservative grid scenario and near-real time calculations that use conservative fault sources and coarse grid sizing. This is necessary because it may be that no tsunami is associated with an earthquake, due to a very high depth or other fault mechanism for which the evaluated dislocation is negligible. For this assessment, the used grid size is typically in the range of 1 to 2 km.
- *Early run-up area identification.* The objective here is to identify more precisely the likely affected locations and try to estimate the run-up height and the potential inundation in the various coastal areas. The used grid size is on the order of 100 to 300m.
- *Inundation assessment.* If detailed DEM is available the inundation calculations can be performed. In this case the requested detail level is on the order of 10-to 30m-cell grid size. The results are affected by the precision of the available topography and bathymetry.
- *Risk assessment and risk management calculations.* They are performed before an event and are based on historical events. These calculations are aimed at preparing evacuation plans in case of tsunami. They are very much site specific and in general it is necessary to perform very detailed calculations reducing the cell size to 5 to 10m.

For the tsunami in Samoa, *post event calculations* have been performed in order to better understand the phenomena, identify the locations affected and obtain feedback to assess the near-real time calculations and evaluate the possibility to quantify the extent of inundation.

The analysis is conducted using three numerical codes: the *SWAN-JRC* code (Annunziato, 2007), which is the basis for the overall tsunami grid scenario calculations in support of GDACS; the *HyFlux2 JRC* code (Franchello, 2008), (Franchello, *et al.*, 2008), (Franchello, 2010), (Cruz, *et al.*, 2010) which is used for the inundation calculations; the *TUNAMI2* code (Imamura, Yalciner, & Ozyurt, 2006), to have another reference code.

The mentioned numerical codes solve the shallow water equations using different numerical methods: *SWAN-JRC* and *TUNAMI* use the finite difference method (FD) while *HyFlux2* uses the finite volume method (FV).

The *finite difference* method is largely used to model tsunami wave propagation and run-up. Models based on this scheme are usually less time consuming than those based on finite volumes. However, most of the FD codes present unphysical oscillations when dealing with flow discontinuities such as wetting and drying interfaces and bore formation.

- *The finite volume method has been developed in the past to simulate dam-break events and flash flooding and has been used recently also for tsunami modelling. The finite volume method is conservative in terms of mass and momentum and, if the dry/wet front is well modelled, the method is particularly suitable for run-up and inundation modelling.*

Science of Tsunami Hazards, Vol. 31, No. 1, page 21 (2012)

SWAN-JRC code is the numerical code implemented for the *Global Disaster Alerts and Coordination System (GDACS)*. GDACS has been jointly developed by the European Commission and the United Nations and combines existing web-based disaster information management systems, with the aim to alert the international community in case of major sudden-onset disasters and to facilitate the coordination of international response during the relief phase of the disaster. When a new event is detected by the seismological sources (USGS, EMSC), an evaluation of the importance of the event from a humanitarian point of view is performed. In case of an earthquake event occurring under water and of magnitude greater than 6.5, the JRC Tsunami Assessment Tool is invoked and a new calculation is requested. The SWAN-JRC model solves the shallow water equations by the finite difference numerical scheme based on the Mader code (Mader C., 2004).

The SWAN-JRC code estimates also the fault length, height and direction to determine the initial water displacement. The code initializes the calculation space, performs the travel time propagation calculation, verified at each step if there are locations reached by the wave and thus updates the visualization and animation files. For early warning purposes the model can run automatically and will publish the results in the GDACS web site.

TUNAMI code consists of several sub-codes:

- (a) TUNAMI-N1, linear theory with constant grids.
- (b) TUNAMI-N2, linear theory in deep sea, shallow-water theory in shallow sea and run-up on land with fixed grids.
- (c) TUNAMI-N3, linear theory with varying grids.
- (d) TUNAMI-F1, linear theory for propagation in the ocean in the spherical coordinates.
- (e) TUNAMI-F2. linear theory for propagation in the ocean and coastal waters.

In this analysis TUNAMI-N2 has been used. The TUNAMI code package is included in the SWAN-JRC suite and therefore the results can be easily produced within the same environment as the SWAN code.

HYFLUX2 code has been developed to simulate severe inundation scenarios due to dam break events, flash floods and tsunami-wave run-up. The model solves the conservative form of the two-dimensional shallow water equations using a finite volume method. The interface flux is computed by a Flux Vector Splitting method for shallow water equations based on a Godunov-type approach. A second-order scheme is applied to the water surface level and velocity. Physical models are included to deal with bottom steps and shorelines. The second-order scheme together with the shoreline-tracking method makes the model well balanced in respect to mass and momentum conservation laws, providing reliable and robust results. In HYFLUX2, numerical stability is ensured under the Courant-Friedrich-Levy (CFL) criteria (Franchello, 2010).

In addition, HYFLUX2 is included in the suite of codes that can be invoked by the SWAN-JRC suite, thus enabling an easy comparison of the code results.

NOAA-MOST code. The MOST package (Titov, *et al.*, 2005) is a suite of numerical simulation codes capable of simulating three processes of tsunami evolution: earthquake deformation, transoceanic propagation and inundation.

MOST Tsunami modelling proceeds in three distinct stages:

- A Deformation Phase generates the initial conditions for a tsunami by simulating ocean floor changes due to a seismic event.
- A Propagation Phase propagates the generated tsunami across deep ocean using Nonlinear Shallow Water (NSW) equations.
- An Inundation Phase simulates the shallow ocean behaviour of a tsunami by extending the NSW calculations using a multi-grid “run-up” algorithm to predict coastal flooding and inundation.

The tsunami generation process is based on a fault plane model of the earthquake source (Okada, 1985), which assumes an incompressible liquid layer on an underlying elastic half space to characterize the ocean and the Earth’s crust. The implementation of this elastic fault plane model (Titov, 1997) utilizes a formula for static sea-floor deformation to calculate the initial conditions required for subsequent computations of tsunami propagation and inundation.

The near-real time calculations performed by NOAA considered the best fitting scenario used at the moment of an event. NOAA’s Pacific Marine Environmental Laboratory (PMEL) forecast system combines real-time seismic and tsunami data with a forecast database of pre-computed scenarios. The database model scenarios for unit sources consist of fault blocks of 100 km along strike and 50 km down dip. The model requirement in this case is similar to retrospective studies: the solution must provide the best fit to the observations (Titov *et al.*, 2005) and use seismic or DART scaling factors to fit the data. The use of these scaling laws may be inadequate for complex events resulting in forecasting errors (Weinstein S., 2008).

NOAA-MOST initial conditions are adjusted by direct comparison with the Deep-ocean Assessment and Reporting of Tsunamis (DART) buoys stations available records, in order to estimate correctly the source parameters that better represent the results (tsunami forecast)³.

Commonly, most of the numerical tsunami models use nested computational grids from coarse to high-resolution, to get more detail into the area of interest, i.e., the coastal flooding and inundation is commonly simulated by extending propagation calculations with such a nested grid approach.

The most common procedure to track movements of the shoreline (Imamura, *et al.*, 2006) is the moving boundary treatment. Run-up is calculated with nonlinear computations.

Science of Tsunami Hazards, Vol. 31, No. 1, page 23 (2012)

³ NOAA-MOST results are accessed online through an agreement between NOAA and JRC.

HYFLUX2 uses a shoreline tracking method to model the interface between dry and wet zones (Franchello, 2010). HYFLUX2 inundation 2D scheme has been designed to identify the shoreline as an intersection between two planar surfaces, which describe the bottom, and the water free surface. Mass conservation is always realised during the wetting/drying processes. With this method a cell can be partially wetted, i.e. the fraction of cell that is wetted is a result of the proposed shoreline tracking methodology.

Other FV models have realized a preservation of mass conservation during dry/wet processing by reconstructing the bottom topography (Audusse, *et al.*, 2004), (Brufau, *et al.*, 2003), (Marche, 2005), (Liang, 2010).

Another way to describe the wet/dry moving front and inundation process is the adaptive grid approach, which is studied in detail in (Liang, 2004), and (Liang, 2010).

In the TUNAMI-N2 code, like in other FD models, a numerical algorithm is needed to determine if the total water depth is high enough to flood the neighbouring dry cells (land) and hence to move the shoreline. Momentum equations are used to update the volume in the wet cells only. When the water surface is rising, the volume flux is no longer zero and the shoreline moves one grid point in the onshore direction.

2. DESCRIPTION OF THE TSUNAMI EVENT

2.1. Tectonic Summary

In order to perform correct tsunami simulations of the 29 September 2009 Samoa earthquake, it is necessary to take into account the tectonic setting and seismicity of Samoa and its surrounding area. It is important to analyse the entire scenario of effects by carrying out a sensitivity analysis on earthquake parameters in the form of epicentre, depth, fault length, fault width, slip distribution and fault mechanism (Annunziato, 2009).

The earthquake occurred as part of a clustering of major seismic activity in the north of Tonga Trench (TT) which may have reflected a reactivation of all major plate boundaries in the region (Pelletier, Calmant & Pillet, 1998).

The Tonga Trench is located in the Pacific Ocean and is 10882 meters (35702 ft) deep at its deepest point, known as the Horizon Deep. It is a deep canyon on the edge of the Pacific Plate. The region has a complex tectonic regime and very high level of seismic activity related to the compression motion between the Pacific and Australian Plates (Pelletier, Calmant, & Pillet, 1998).

The Pacific tectonic plate dives beneath the Australian plate at a rate of almost a centimetre a year, making the area one of the most active earthquake regions in the world. Earthquakes occur within the Pacific plate on both sides of the trench. The trench and associated faults are forming as the Pacific Plate moves westward, sinking beneath a complex series of smaller plates on the edge of the Australian Plate. There have been around 30 quakes of magnitude 7.0 or more along this trench since 1900⁴. The Figure 1 shows the location of the earthquake in relation to the Samoa islands.

Science of Tsunami Hazards, Vol. 31, No. 1, page 24 (2012)

³NGDC Tsunami Runup database, <http://www.ngdc.noaa.gov/nndc/struts/form?t=101650&s=167&d=166>

⁴ Deep-ocean Assessment and Reporting of Tsunamis, <http://nctr.pmel.noaa.gov/Dart/>

⁴

<http://www.un.org.au/files/files/Samoa%20Tonga%20Tsunami%20OCHA%20SitRep%20No%206%206%200ct%2009.pdf>

⁴ <http://earthquake.usgs.gov/regional/nejc>

In an extensive study performed on year 1980 (Pararas-Carayannis, et al., 1980) about 60 tsunamis - generated by earthquakes in the Pacific Ocean - have located the Soamoa Islands. The 2009 tsunami under analysis was very similar to the one on June 26, 1917.

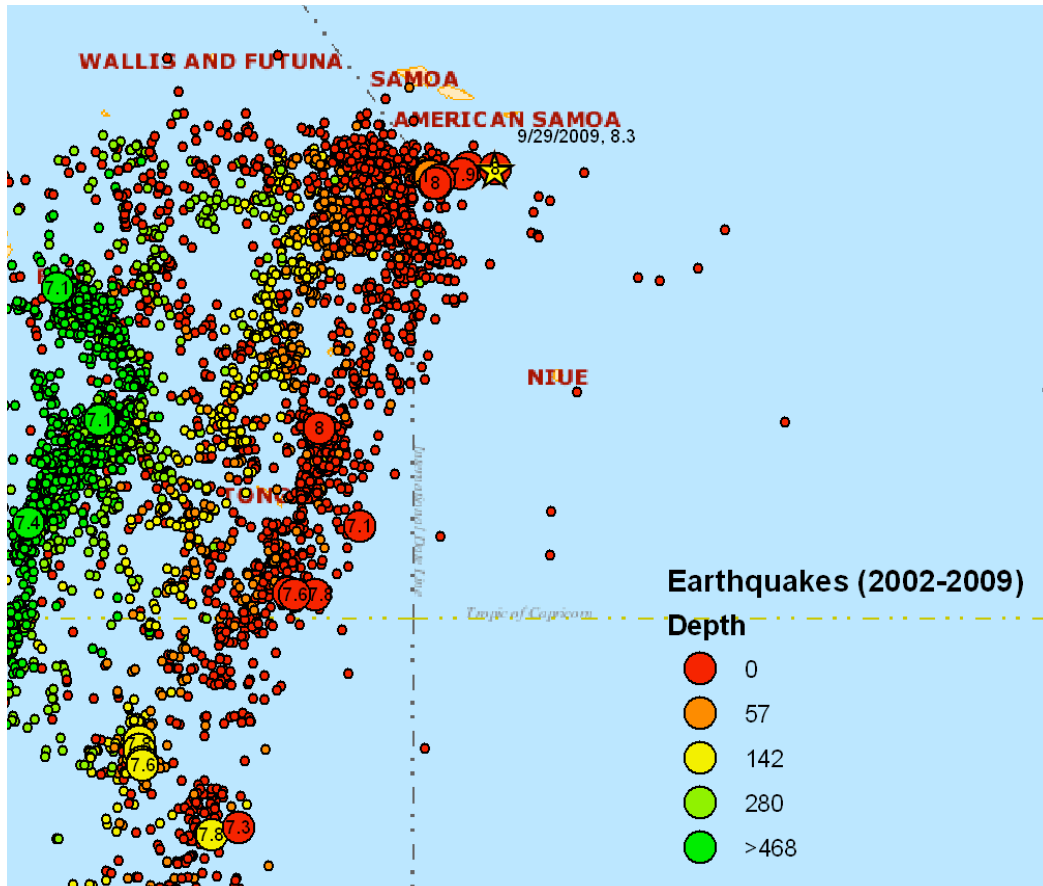


Figure 1 - Distribution of the historical earthquakes (dots) and epicentre of the 29 September 2009 Samoa earthquake (star)

2.2 Available measurements

Several in-situ sensors are located in the area, but not all were functioning during the event. The closest to epicentre online measurement points, against which the calculations will be compared, are shown in Figure 2.

According to the tsunami travel time both DART buoys should have been reached in about 1h and the tidal measurements between 15 and 25 minutes after the event.

A negative initial wave was recorded by 3 sensors (51425, Apia and Pago Pago, (see Figure 3, figure 5, Figure 6) which is consistent with the proposed fault mechanism (see next chapter). The sensor on the North – Northeast side shows a negative section; while 51426 shows (Figure 4) an initial positive section which could indicate that a higher positive section should be present in the Southern part of the fault.

There are several other measurement points available in the Pacific Ocean that can be useful to estimate the arrival time, but the ones indicated are the most relevant to analyse the tsunami phenomenon with acceptable detail.

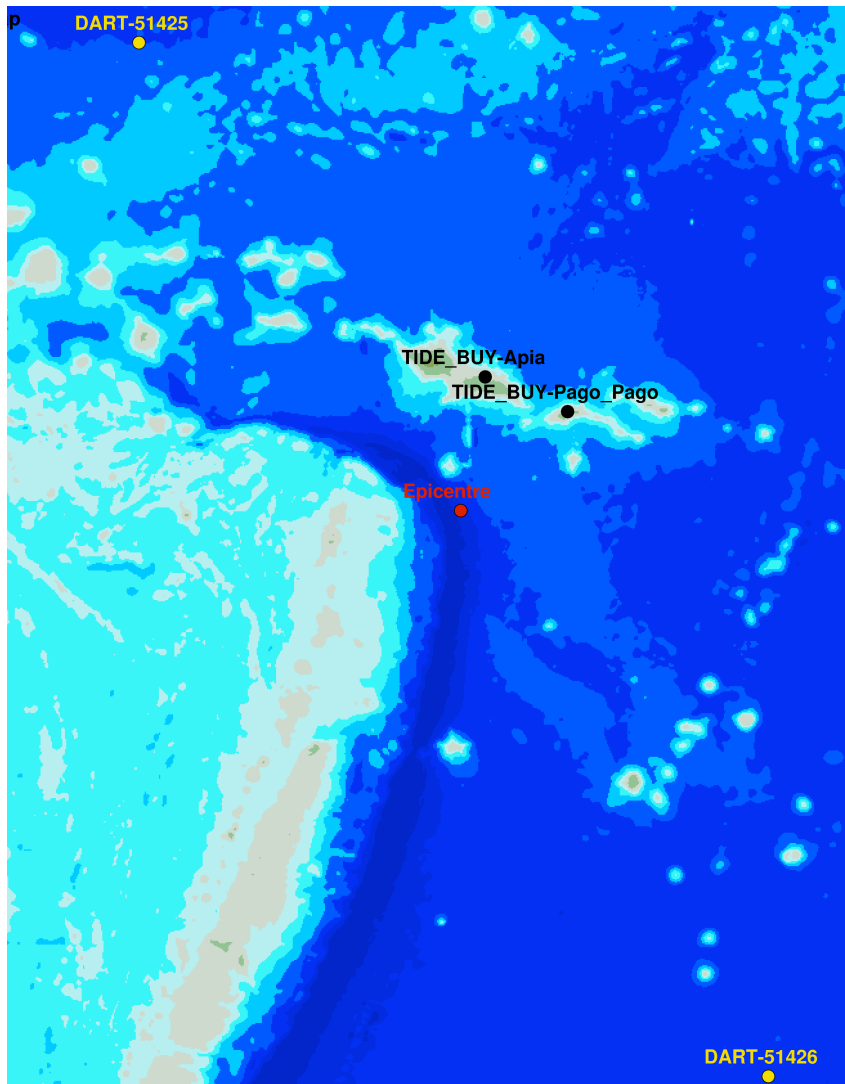


Figure 2 - Online measurements

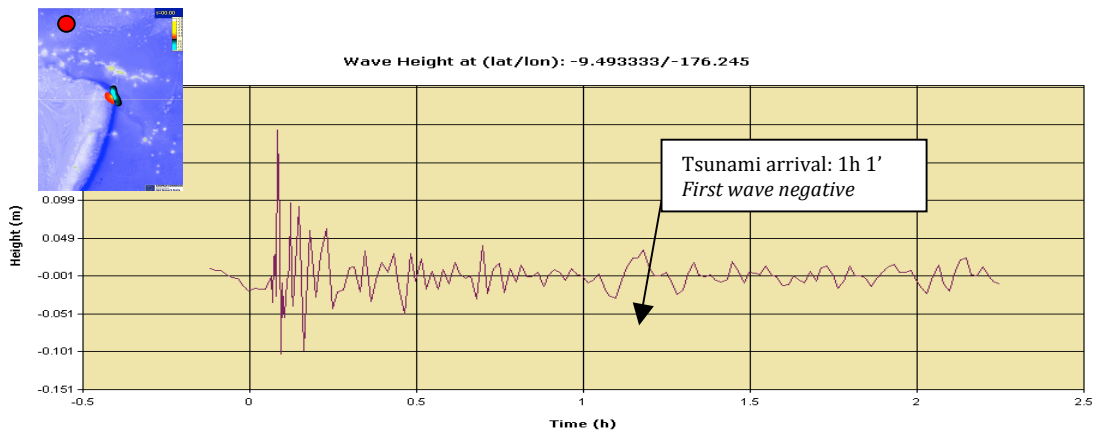


Figure 3 - DART Measurement 51425

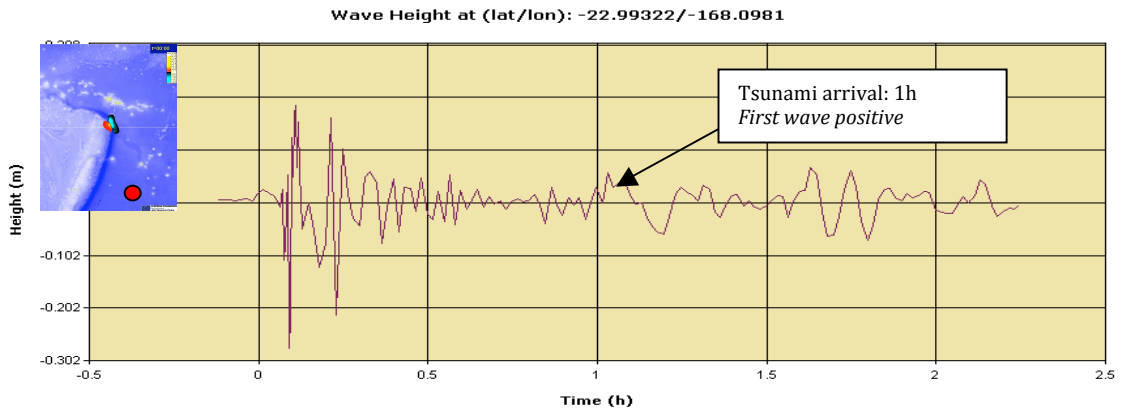


Figure 4 - DART Measurement 51426

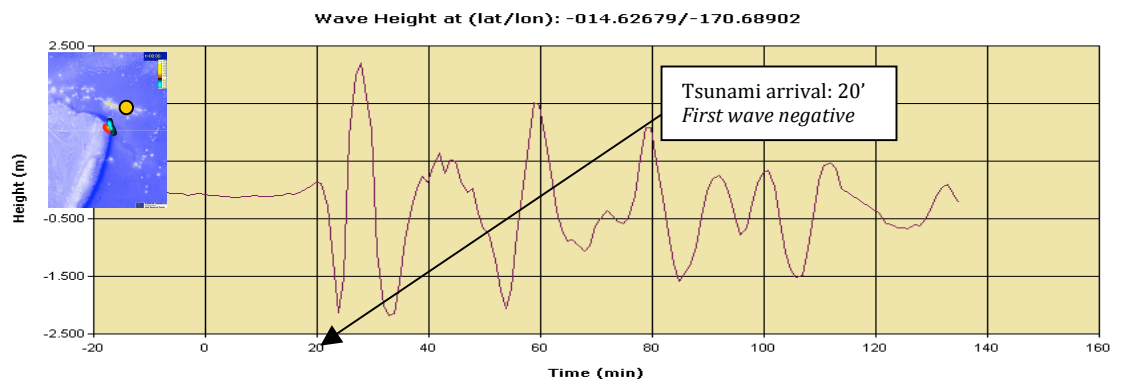


Figure 5 - Tidal measurement in Pago-Pago

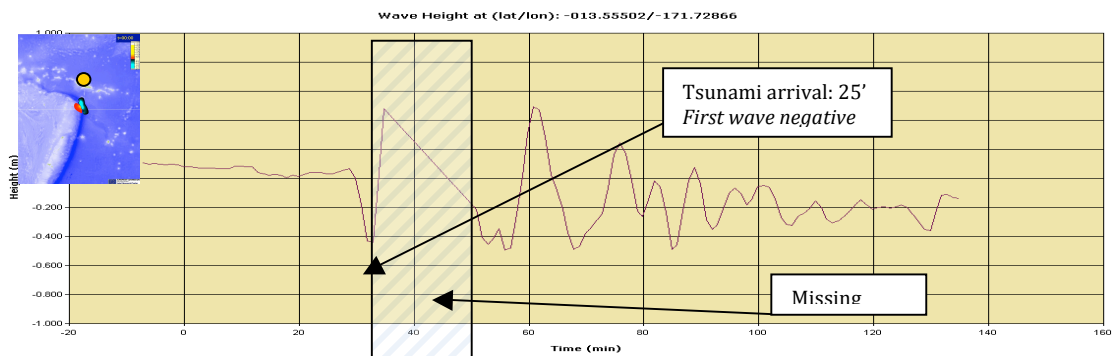


Figure 6 - Tidal measurement in Apia

The conditions of the tide at the time of the tsunami were in the descending part (Figure). In this location and this period of the year, the tidal height does not show large variations, about 0.5m between minimum and maximum. Post-tsunami survey measurements on the run-up height 5 and damage maps performed using satellite images on the inundated area⁶ became available on the web some weeks after the event.

Science of Tsunami Hazards, Vol. 31, No. 1, page 27 (2012)

⁵ <http://www.ngdc.noaa.gov/nndc/struts/form?t=101650&s=167&d=166>

⁶ http://unosat.web.cern.ch/unosat/asp/prod_free.asp?id=125

http://unosat.web.cern.ch/unosat/asp/prod_free.asp?id=126

Buoy readings DART Pacific
400 NM Southeast of Tonga
-22.99322/-168.0981

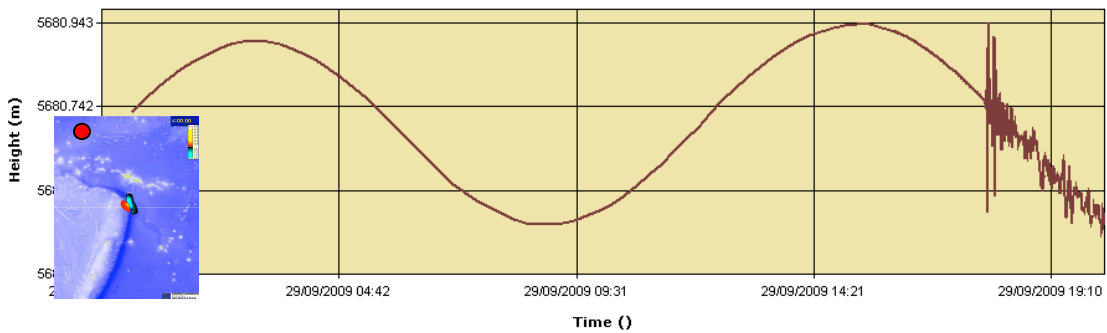


Figure 7 - DART Measurement 51425, long range, tidal data

Most of the post-tsunami survey measurements were done in Tutuila Island (American Samoa), where 34 fatalities were recorded, while on Opolu Island – with 149 fatalities – only the buoy measurement is available. On Niauatoputapu Island – with 9 fatalities – no measurements were recorded in the NGDC database, but a field survey done 2 months later recorded a maximum run-up of 22 m (EERI, 2010). Damage maps performed using satellite images (see Figure 8 and Figure 9) are available for Savali'i & Upolu Islands (Samoa) and for Tutuila Island (American Samoa).

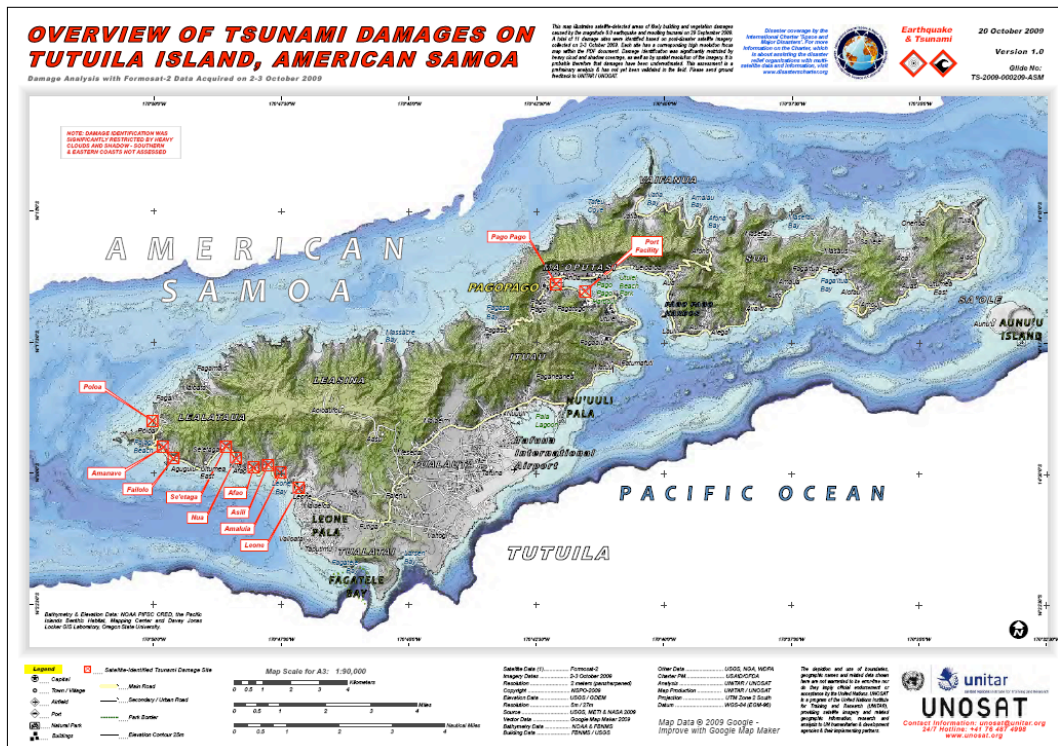


Figure 8 - Overview of tsunami damage on Tutuila Island

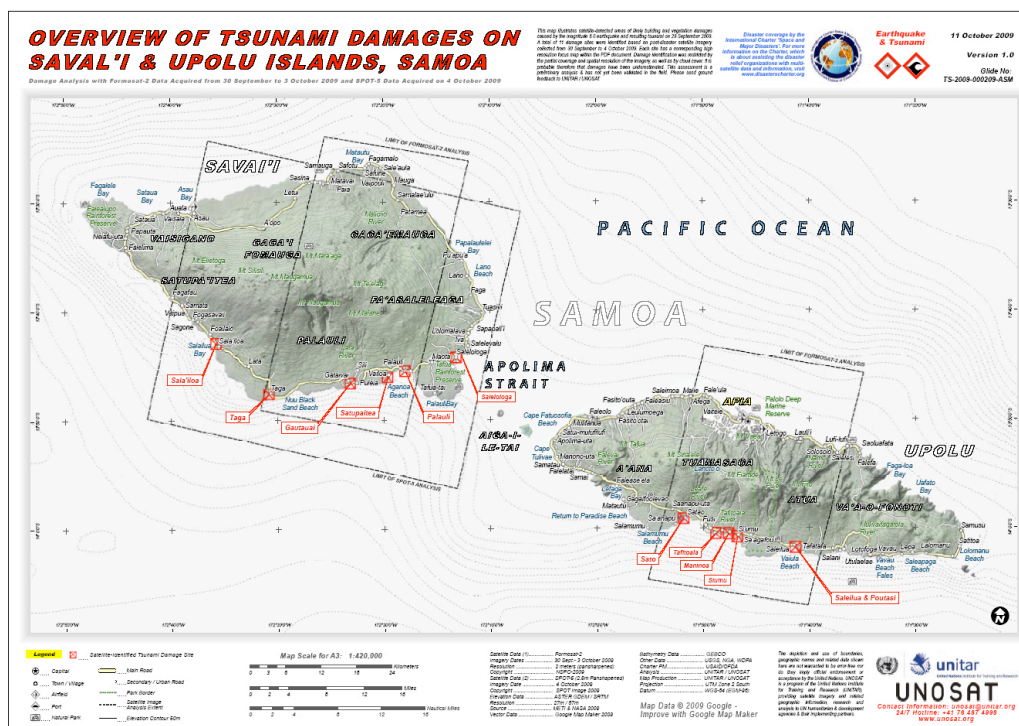


Figure 9 - Overview of tsunami damage on Savai'i & Upolu Islands

Table 1 - Post-tsunami survey measurements. Type: 1 = Eyewitness, 5 = Post-tsunami Survey, 2 = Tide-gauge, 3 = Deep ocean gauge, 6 = Atmospheric Wave, 7 = Seiche

| Tsunami Runup Location | | | | Tsunami Runup Measurements | | | | | Tsunami Runup Location Effects | |
|----------------------------------|----------|-----------|----------------------|----------------------------|-----|------------------|------|-----|--------------------------------|--------|
| Name | Latitude | Longitude | Distance from Source | Travel Time | | Max Water Height | Type | Per | Lst Mtn | Deaths |
| | | | km | hr | min | m | | | | Num |
| NIUATOPUTAPU | -15.95 | -173.75 | 184 | | | | 1 | | | 9 |
| AMANAVE, AMERICAN SAMOA | -14.333 | -170.829 | 187 | | | 7 | 5 | | | |
| POLOA, AMERICAN SAMOA | -14.322 | -170.833 | 188 | | | 16.3 | 5 | | | |
| LEONE, TUTUILA I, AMERICAN SAMOA | -14.344 | -170.791 | 189 | | | 5 | 5 | | | |
| UPOLU, APIA | -13.817 | -171.75 | 190 | | 21 | 0.78 | 2 | 8 | R | 149 |
| FAGATELE BAY, AMERICAN SAMOA | -14.37 | -170.764 | 190 | | | 5 | 5 | | | |
| VAITOGI, AMERICAN SAMOA | -14.359 | -170.735 | 193 | | | 4 | 5 | | | |
| PAGO PAGO, AMERICAN SAMOA | -14.283 | -170.683 | 203 | 0 | 11 | 2.16 | 2 | 8 | R | 34 |
| PAGO PAGO, AMERICAN SAMOA | -14.281 | -170.674 | 203 | | | 7 | 5 | | | |
| FAGAITUA, AMERICAN SAMOA | -14.28 | -170.612 | 209 | | | 4 | 5 | | | |
| AMOULI, AMERICAN SAMOA | -14.278 | -170.583 | 211 | | | 3 | 5 | | | |
| ONENOA, AMERICAN SAMOA | -14.257 | -170.58 | 213 | | | 4 | 5 | | | |
| TULA, AMERICAN SAMOA | -14.258 | -170.564 | 214 | | | 7 | 5 | | | |
| FAGAMOLA, AMERICAN SAMOA | -14.249 | -169.504 | 311 | | | 12 | 5 | | | |
| NUKUALOFA (NUKU'ALOFA) | -21.133 | -175.167 | 707 | 0 | 59 | 0.15 | 2 | 10 | | |
| D51425 BPR, 370 NM NW OF APIA | -9.493 | -176.245 | 805 | | | 0.04 | 3 | | | |
| D51426 BPR, 400 NM SE OF TONGA | -22.993 | -168.098 | 934 | | | 0.05 | 3 | | | |

Separate focus maps are included, highlighting damage sites identified from post-disaster satellite imagery collected from 30 September to 4 October 2009. Damage identification was restricted by the partial coverage and spatial resolution of the imagery, as well as by cloud cover. It is probable therefore that damage estimates have been underestimated. This assessment was a preliminary analysis not yet validated in the field when the report (UNITAR/UNOSAT, 2009) was written.

3. SIMULATION METHODOLOGY AND BOUNDARY CONDITIONS

The tsunami simulations depend strongly on: a) the initial fault mechanism; b) the hydraulic conditions (DEM, cell size). It is also important to point out that the earthquake information available immediately after the event were only epicentre, magnitude and depth. All these estimated quantities may change significantly in time due to progressive improvement of the seismological parameters. The day after the event the fault mechanism was identified and two days later USGS published the finite fault model solution, which is the best characterization of the fault available at the moment.

The choice of the tsunami source is usually a complicated issue because it requires good knowledge of the earthquake parameters such as epicentre, depth, fault length, fault width, slip distribution and rupture mechanism. It is assumed that the tsunami is generated by co-seismic displacement of the sea floor. Thus, the initial condition for the modelling of the expected tsunami in the region is assumed to coincide with the vertical co-seismic displacement of the sea bottom induced by the earthquake. The initial conditions are one of the major factors that affect the wave propagation and the resulting run-up amplitudes along the coast. Different approaches can be used to calculate the initial conditions from the motion of the fault.

The first approach is to evaluate the Earth deformation caused by the earthquake and impose an initial water level as proposed by Ward (Ward, 2002). This approach gives the initial water level increase by using the empirical relationships between the magnitude of the earthquake and fault length and width.

The second one was developed by Okada (Okada, 1985). This algorithm calculates the distribution of co-seismic uplift and subsidence by using the epicentre of the earthquake, fault strike, fault dip, fault rake and amount of average displacement on the fault.

The third approach is to use the fault and the direction of slips by separating the fault plane into sub-faults. In order to reveal the rupture process of the fault with this approach, USGS uses GSN broadband waveforms downloaded from the National Earthquake Information Centre (NEIC) waveform server⁷. They analyse teleseismic broadband P waveforms, broadband SH waveforms and long period surface waves selected based on data quality and azimuthal distribution. Waveforms are first converted to displacement by removing the instrument response and then used to constrain the slip history based on a finite fault inverse algorithm (Ji, Wald, & Helmberger, 2002).

The earthquake parameters, fault mechanism solutions and slip distribution cross-section of the fault model – which are available after the earthquake from the different organizations – are given respectively in fault model – which are available after the earthquake from the different organizations – are given respectively in Table 2 and Table 3. The mechanism solutions show an almost normal fault, on a plane striking roughly parallel to the Tonga Trench axis, with seismic moment of 1.82×10^{28} dyne cm.

Science of Tsunami Hazards, Vol. 31, No. 1, page 30 (2012)

⁷ http://earthquake.usgs.gov/earthquakes/eqinthenews/2009/us2009mdbi/finite_fault.php

Table 2 - Earthquake parameters (USGS/NEIC)

| | |
|----------------|------------------------------------|
| Magnitude (Mw) | 8.0 |
| Date and Time | 29, September 2009 at 17:48:10 UTC |
| Location | 15.509°S, 172.034°W |
| Depth (km) | 18 |
| Region | Samoa Island Region |

In the following sections we will show the fault mechanisms adopted for the various phases and will compare them.

3.1 Fault mechanism and hydraulic initial condition

For the definition of the hydraulic initial condition it is assumed that the bottom floor Earth deformation is instantaneously transmitted to the water. Thus the initial water level field is initialized with the bottom deformation.

The near-real time calculations were performed using the JRC fault model (based on the Ward approach), which should be considered as an upper bound or worst case. Several calculations were automatically requested by the early warning system (see Table 6) until the epicentre was better identified (see previous chapter). The final case has been performed with the following parameters:

- L=158 km, W=44 km, Strike=318.4, Form Cosinusoidal, all positive, Slip=3.16m

The JRC fault model (see Figure 10, left assumes a cosinusoidal shape all positive, in order to maximize the impact. The model assumes a standard earthquake depth of 5 km, and applies a scaling factor for the real depth. For a depth of 18km, the depth factor is 0.8. Thus, the calculated wave height of 3.16m is reduced to 2.5m.

Other near-real time calculations during the event were those performed by NOAA⁸ with the MOST code (Titov, *et al.*, 2005). They found that the best solution for the current fault (as compared with the DART measurements), was obtained using the unit sources ntsza34 plus the ntszb34 solution, both multiplied by the factor 3.96 (see Figure 10 – Fault models: JRC left, NOAA, right). It should be remembered that every NOAA unit fault source corresponds to a 100 km x 50 km fault of elevation 1m (e.g. corresponding to a magnitude of 7.5); thus it is necessary to multiply by some factor to take into account the magnitude difference.

⁸ <http://nctr.pmel.noaa.gov/propagation-database.html>

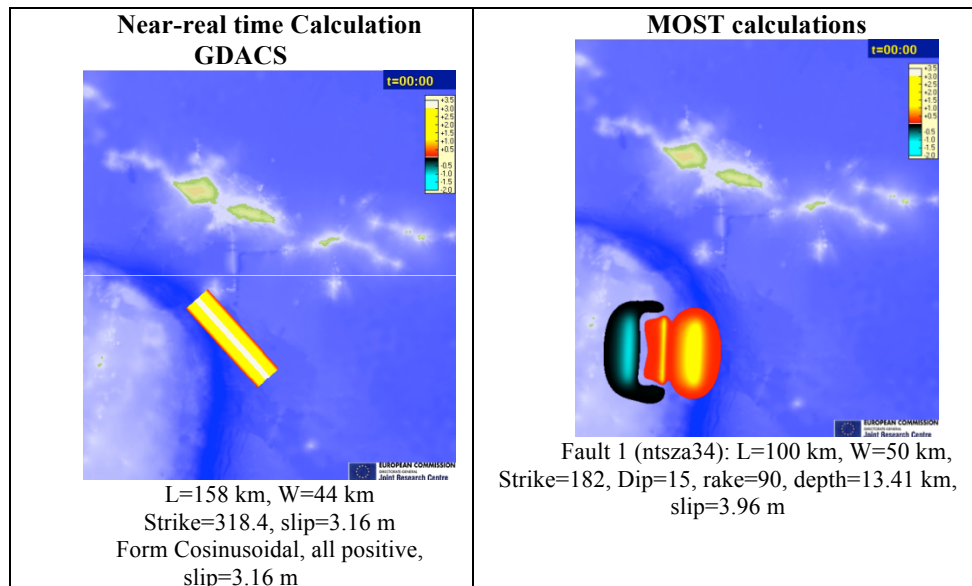


Figure 10 - Fault models: JRC left, NOAA right

According to the fault mechanisms published by USGS the day after the event, two possible solutions can be analyzed; the USGS solution and the Harvard one. They differ for the location and mostly for the strike angle (more vertical in the Harvard case).

The parameters in Table 3 have been included in the Okada model (Okada, 1985) in order to set up the initial deformation.

Table 3 - Fault mechanism solutions

| Time 17:48:10.57 | | Lat/L | Mag | Strike | Dip | Rake | Depth |
|------------------------|----------|-----------------|------|--------|-----|------|-------|
| | | on | (Mw) | | | | (km) |
| USGS | Centroid | - | 8.0 | 345 | 46 | -61 | 10 |
| Moment Tensor Solution | | 15.418/-172.005 | | | | | |
| Harvard | Global | - | 8.1 | 7 | 71 | -64 | 12 |
| CMT Project | Moment | 15.195/-171.9 | | | | | |
| Tensor Solution | | | | | | | |

Two days after the event the Finite Fault Model solution was published by USGS. The hypocenter adopted was the USGS one (Lon. =-15.60 deg.; Lat.=-172.30 deg.).

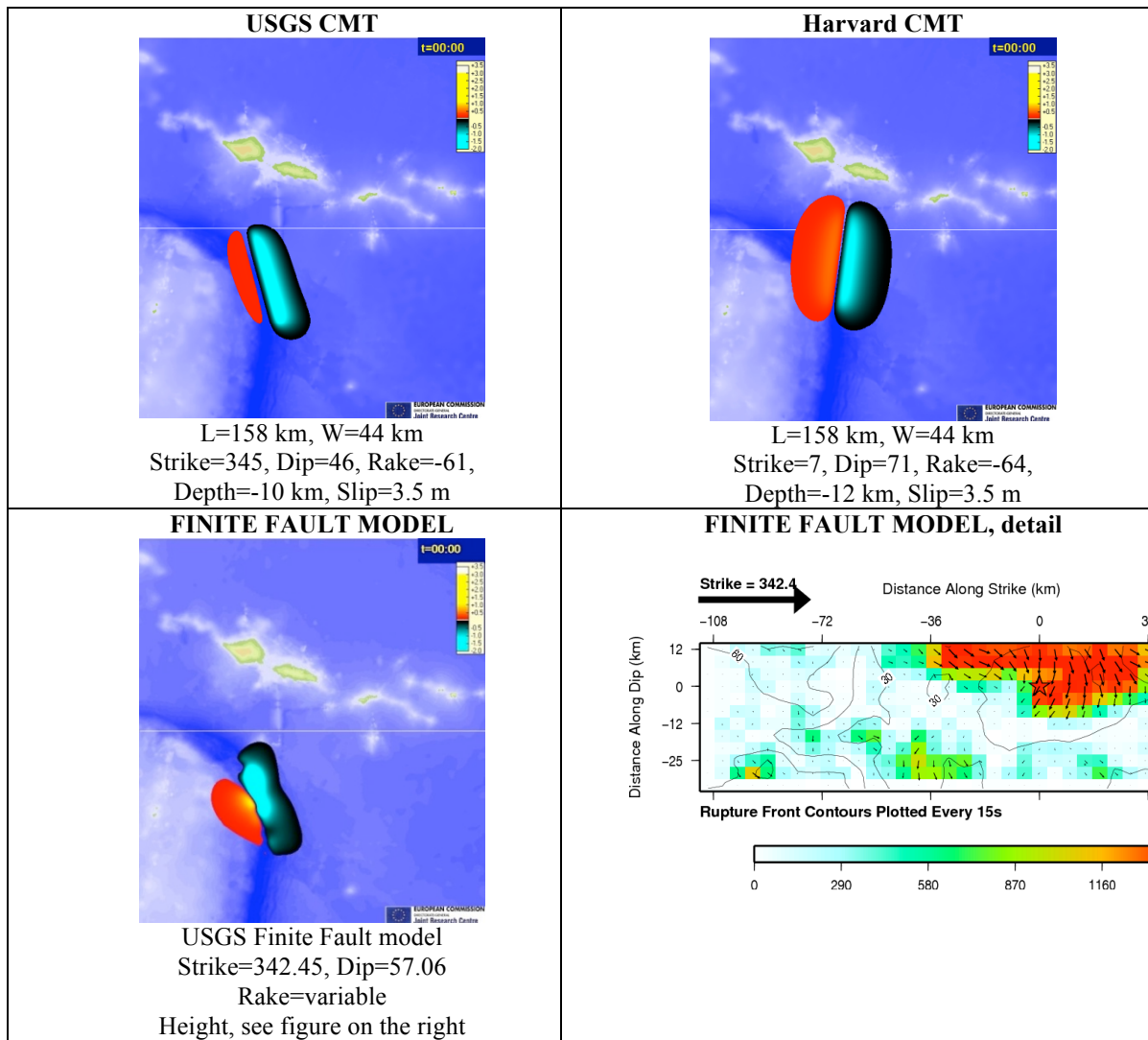


Table 4 - Different sources for post-event calculations. The best “simple” solution is the one proposed by CMT USGS.

The result of this procedure is a series of 432 individual sources of 5 km by 4 km; all at strike 342.45 and dip 57.06. All fault planes have their own rake and slip. Combined, the sources produce an initial deformation as shown in the previous figure, which indicates that the best “simple” solution is the one proposed by CMT USGS.

In order to evaluate the effect of each solution on the wave height estimates, it is necessary to run simulations for the various source solutions. It may be anticipated however that, contrary to the adopted initial condition for the near-real time calculation (cosinusoidal shape all positive), all the solutions show a negative section on the Northeast side.

Most of the calculations have been performed using as initial conditions the Finite Fault model because it is considered to be the best one, as confirmed by sea level measurements.

About one year after the event (Lay, et al., 2010), further detailed analysis of the seismic information indicated that the tsunami could be enhanced by an additional doublet triggered 2 minutes after the initial normal fault event (magnitude 8). This doublet corresponds to a second earthquake of magnitude 8.

Another study published at the same time (Beaven, et al., 2010), proposed a fault model consisting of a slow thrust event of magnitude 8 which triggered several minutes after a normal fault (outer rise) event of magnitude 7.9. The analysis was based on using GPS measurements, field surveys in Niuaotupapu Island (close to the epicentre) and DART measurements. However, the objectives of this paper is to understand what the accuracy is of the tsunami early warnings triggered by the fault models data available from a few minutes to a few days after the event: for this reason these latter analyses performed one year after the event have not been included in the present study.

3.2 Digital elevation model

The available Digital Elevation Models (DEM) used for the simulations are listed in Table 5.

Table 5 - Bathymetry and Topography used for the simulations

| Source | Grid size | Bathymetry | Topography | Coverage |
|---|-----------|------------|------------|------------|
| ETOPO1 Global Relief Model 9 | 1' | yes | yes | World |
| SRTM30 PLUS Global topography (v 5.0)¹⁰ | 30'' | yes | yes | World |
| GEBCO Global Topography¹¹ | 30'' | yes | yes | World |
| SRTM DTED® Level 1 (3 arc second)¹² | 3'' | NO | yes | World |
| NOAA - AS 3 arc-second Pago Pago¹³ | 3'' | NO | yes | Pago Pago |
| NOAA - AS 1/3 arc-second Pago Pago¹⁴ | 1/3'' | yes | Yes | Pago Pago. |

The most reliable data sources for which both bathymetry and topography are available worldwide are SRTM³⁰ PLUS¹⁰ and GEBCO¹³. For the inundation simulations in Tutuila Island^{15,16} the DEM developed by NOAA (Lim, et al., 2009) have been used. A sensitivity analysis with respect to the available DEM is described in the next section.

4. GDACS ASSESSMENT

The Global Disaster Alert and Coordination System (GDACS) aims at alerting the international humanitarian response community to impending disasters that will require international response. GDACS consists of an automatic alerting system (sending SMS, email and fax alerts to around 10000 users) and a restricted website for professional responders (the Virtual OSOCC).

Science of Tsunami Hazards, Vol. 31, No. 1, page 34 (2012)

⁹ <http://www.ngdc.noaa.gov/mgg/global/global.html>

¹⁰ http://topex.ucsd.edu/WWW_html/srtm30_plus.html

¹¹ http://www.bodc.ac.uk/data/online_delivery/gebco/










¹² <http://edcns17.cr.usgs.gov/EarthExplorer/>

¹³ <http://www.ngdc.noaa.gov/dem/showdem.jsp?dem=Pago Pago&state=AS&cell=3 arc-second&vdat=MHW>

¹⁴ <http://www.ngdc.noaa.gov/dem/showdem.jsp?dem=Pago Pago&state=AS&cell=1/3 arc-second&vdat=MHW>

After the Samoa event, seismological institutions published more accurate data, which triggered new impact evaluations (see Table 6). The first data was received from the Pacific Tsunami Warning Centre, through the USGS/NEIC information feeds. This was 16 minutes after the event, but had an underestimated magnitude, causing a Green alert. The first Orange alert was based on information from NOAA, received 20 minutes after the event (again through the NEIC feeds). Later, the magnitude estimate was revised upwards and depth downwards, increasing the alert level to Red (with a grid-based tsunami wave height of 4.01m).

Table 6 - List of epicentres identified by the GDACS system, as they were collected¹⁷

| Alert level | Estimated tsunami wave height (m) | Lat/Long | Magnitude (M) | Depth (km) | Source | Publication Date/Time (UTC) | Delay |
|---|-----------------------------------|-------------------------|---------------|------------|--------|-----------------------------|---------|
|  | 0.06 | -15.27, -171.5 | 7.1 | 33 | PTWC | 9/29/2009 06:04:30 PM | 16 min |
|  | 2.27 | -15.4, -171.6 | 7.9 | 33 | NOAA | 9/29/2009 06:09:11 PM | 20 min |
|  | 2.27 | - 15.5538, -172.1409 | 7.9 | 35 | NEIC | 9/29/2009 06:14:51 PM | 26 min |
|  | 2.27 | -15.42, -172.21 | 7.9 | 60 | EMSC | 9/29/2009 06:14:59 PM | 26 min |
|  | 2.27 | -15.43, -172.2 | 8.1 | 60 | EMSC | 9/29/2009 06:30:02 PM | 42 min |
|  | 4.01 | -15.3, -171.0 | 8.3 | 33 | NOAA | 9/29/2009 07:05:59 PM | 1h17min |
|  | 2.27 | - 15.5577, -172.0726 | 8.0 | 18 | NEIC | 9/29/2009 07:37:36 PM | 1h49min |
|  | 2.27 | -15.3, -171.0 | 8.0 | 33 | NOAA | 9/29/2009 10:11:46 PM | 3h23min |
|  | 3.3 | -15.559, -172.0926 | 8.0 | 18 | NEIC | 9/30/2009 03:15:21 PM | >21h |

While these response times are adequate for the international community, the systems would have been too slow to alert some of the most affected areas. The first tsunami waves arrived¹⁸ in Western Samoa 17 minutes after the earthquake. Most cities in Western and American Samoa were reached by the waves within 20 minutes. The highest waves (higher than 7 meters) and generated by local geographic conditions, arrived 30 minutes after the event.

Note that the uncertainty on the earthquake parameters caused an underestimation of wave heights: the maximum wave height reported by the GDACS system increased from 0.06m to 4.01m (1h17 minutes after the event), while the true maximum wave heights were in the order of 7m in American Samoa Islands and up to 20m in Tonga Islands. A detailed report on the automatic GDACS response can be found in (Annunziato, 2009).

4.1 The near-real time calculations

In this section only the final simulation (the last row in Table 6) is discussed. However, the results of all the other simulations are available online in the GDACS report pages.

The system was initialized with an initial maximum height of 3.16m. The maximum wave height near the coast indicated in the calculations is 3.8m in Fagamalo and Poloa and 3.1m in Fagasa, all in Tutuila Island (American Samoa Islands). This calculation, performed with 2.64 min grid size bathymetry (~ 4800 m) was not able to identify the small island where Niuatoputapu Village is located: however, a very high energy above that island is shown.

The comparison with the DART shows that the calculation anticipates the signal by 5 min and the height is overestimated (Figure 12 and Figure 13), while it is very close in height and period for the buoy signal in Pago Pago Bay, Tutuila Island (Figure 14). Nevertheless, the initial negative wave is not predicted because the early warning JRC fault model assumes an all-positive cosinusoidal shape in order to calculate a worst-case scenario.

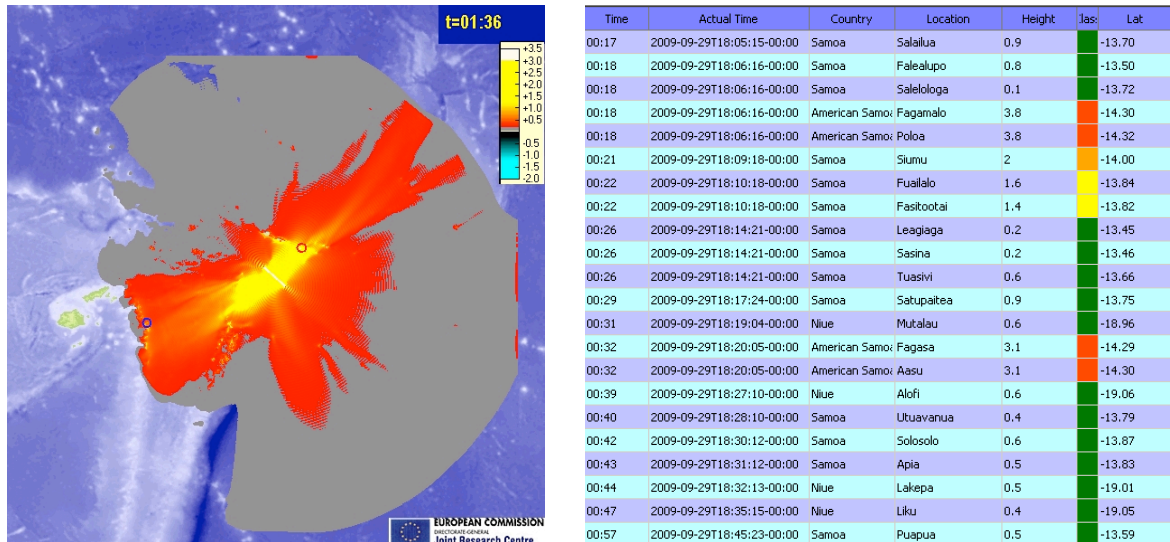


Figure 11 - Near-real time calculation of the Samoa event: on the left the maximum calculated height, on the right the list of identified locations and wave height

The early-identified localities are compared with UNOSAT damage assessment (see Figure 15 and Figure 16). Most of the assessed localities in Savai'i & Upolu Island are identified by the early warning system. In Tutuila Island some of the affected localities identified by the early warning are in the opposite side of the small Island, which is from 5 to 10 km in extent, i.e., on the same order of magnitude as the grid size. However, the objective of alerting the islands has been achieved.

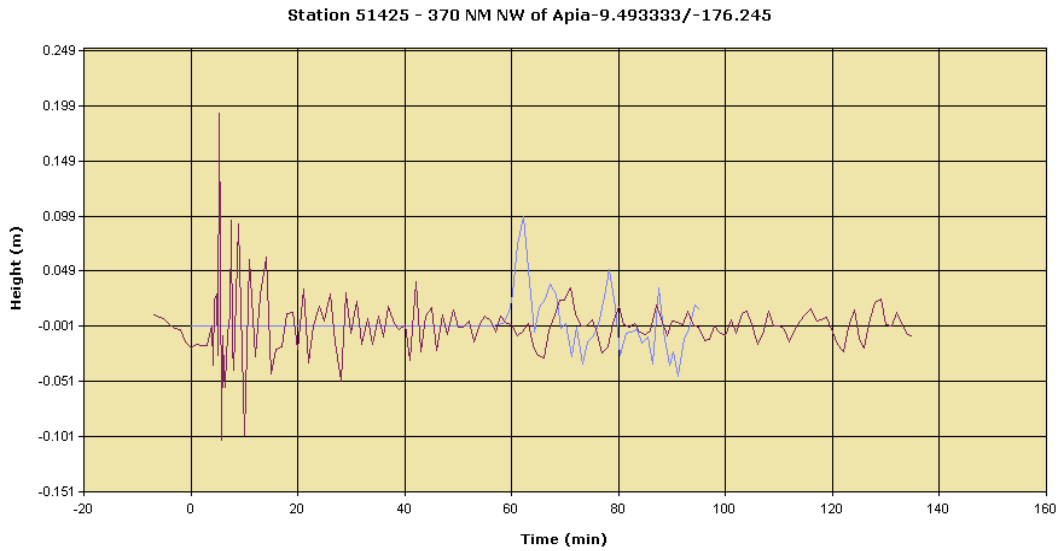


Figure 12 - Comparison of sea level indication from the 51425 DART buoy (red) with the near-real time calculation (blue). Note the oscillation from time 0 min to 60 min in the DART buoy, which are due to the seismic pressure wave transmission.

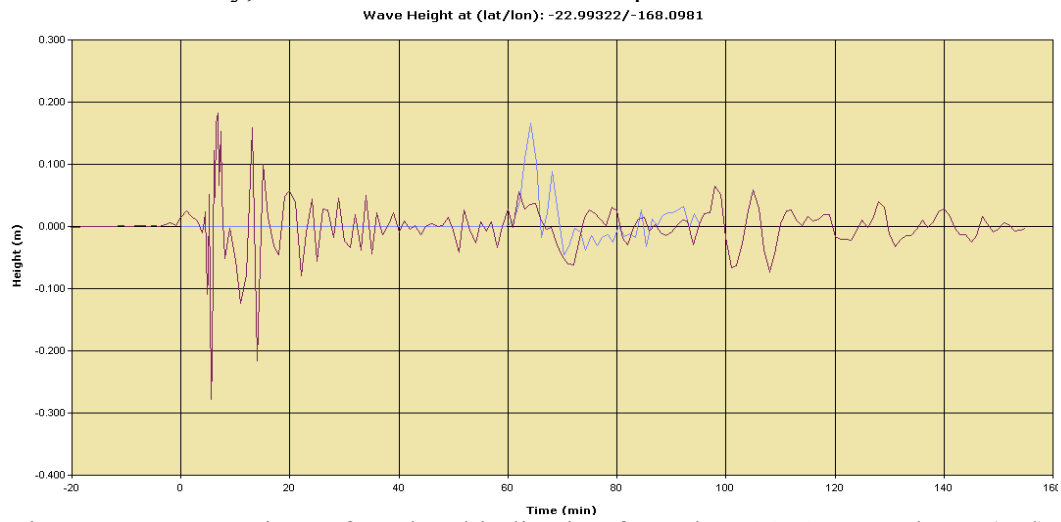


Figure 13 - Comparison of sea level indication from the 51426 DART buoy (red) with the near-real time calculation (blue)

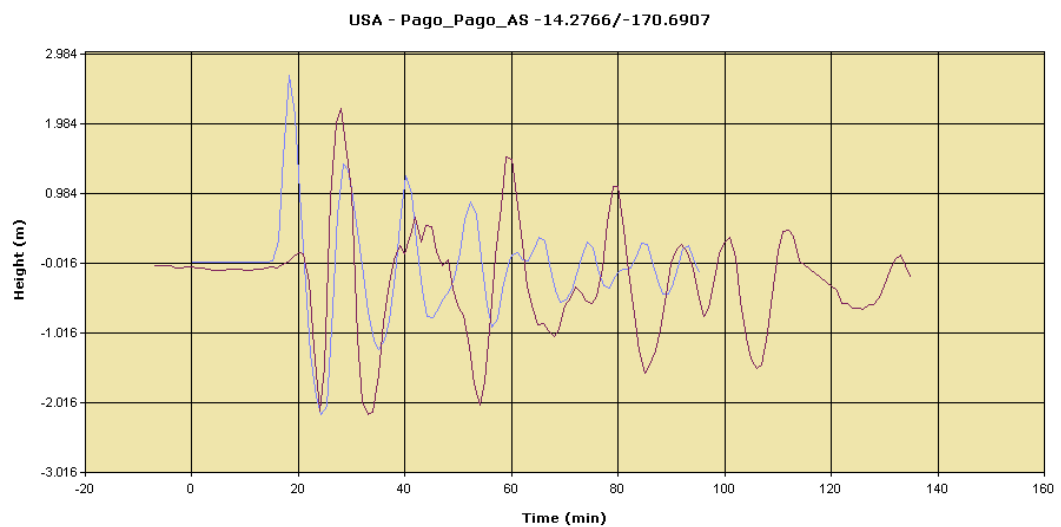


Figure 14 - Comparison of tidal level in Pago Pago (red) with the near-real time calculation (blue)



Figure 15 - Savai'i & Upolu Island. Comparisons of UNOSAT damage assessment and locations (see the place marks) identified by the JRC early-warning system.

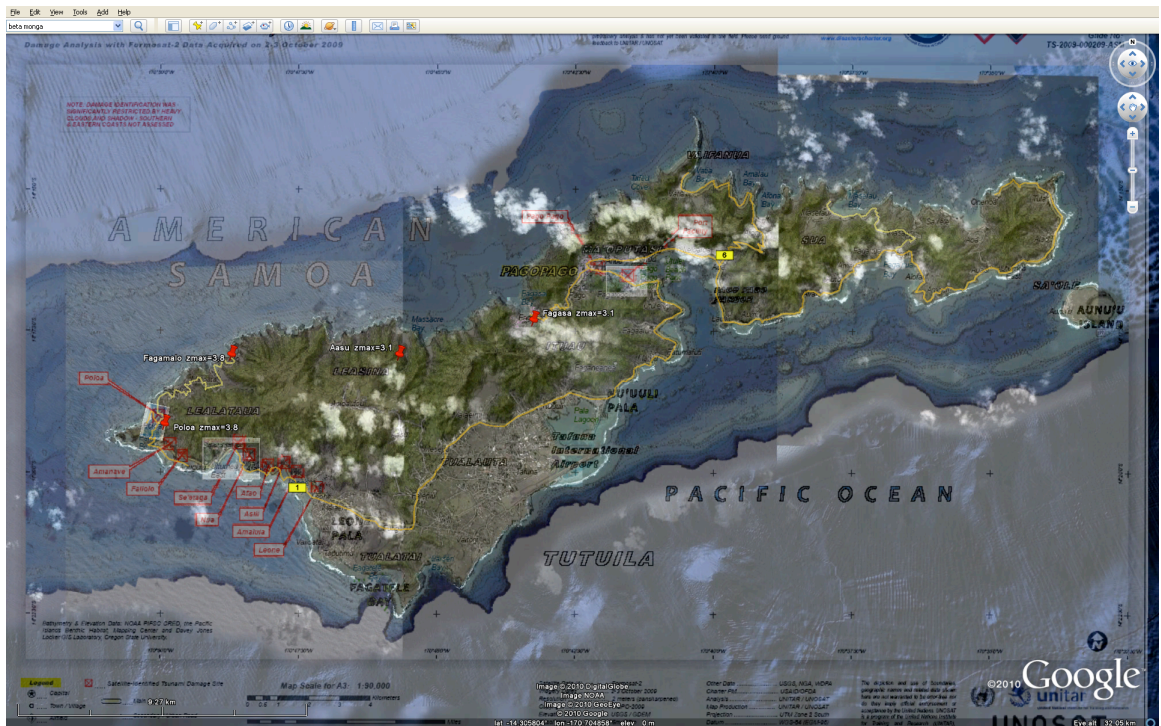


Figure 16 - Tutuila Island. Comparisons of UNOSAT damage assessment map and locations (see the place marks) identified by the JRC early-warning system

4.2 Alert and Models Assessment

Alert assessment is performed in the hours immediately after the event. Together with the objective to assess the early warning launched by retrieval of pre-calculated grid scenario and near-real time simulations, the aim is also to quickly estimate the impact of the tsunami at a more detailed regional scale: in fact the grid size of the near real-time calculations are coarser (~ 4800m) in order to cover a wider window.

In the next section, first the fault sources using the SWAN JRC code are assessed and then the predictions provided by the codes available at the JRC, i.e., SWAN, HyFlux2 and TUNAMI-N2 are assessed.

4.2.1 Fault assessment

In this section are shown the comparisons of the simulations performed by the SWAN JRC code using different fault sources described in section 0 which are available after the event, i.e., USGS-CMT, Harvard CMT and Finite Fault Model. The run grid size is 1800 m.

The fault assessment is based on the available DART measurements (DART 51425 and 51426) and tidal buoy measurements (Pago Pago bay on Tutuila Island and Apia bay on Opolu Island) whose positions are shown in Figure 2.

In Figure and Figure , the comparisons of DART measurements with simulations performed using different fault models are shown. At a first glance, none of the simulations seems to provide good accuracy with the measurements: on both DART's the effects of the p-wave continue until the tsunami (gravitational) wave arrives, providing a measured positive wave on DART 51426, which is opposite with respect to the simulations.

The reason for this prolonged effect of the p-wave as well as its influence on the DART measurement is not well understood or quantified. Probably a best-filter algorithm could improve the quality of the signal. A first explanation could be that the tsunami wave propagates mainly northeast and southwest, while the DART measurements are northwest and southeast of the epicentre, with a consequent lower amplitude of the tsunami gravity wave in respect of the DART directions. Therefore more detailed studies on the use of the DART measurements are necessary.

However, comparing the arrival time and the amplitude of the first measured negative wave with the simulated ones, it can be stated that the Finite Fault Model provides the best wave simulations, while the Harvard CMT Fault model provides the worst ones.

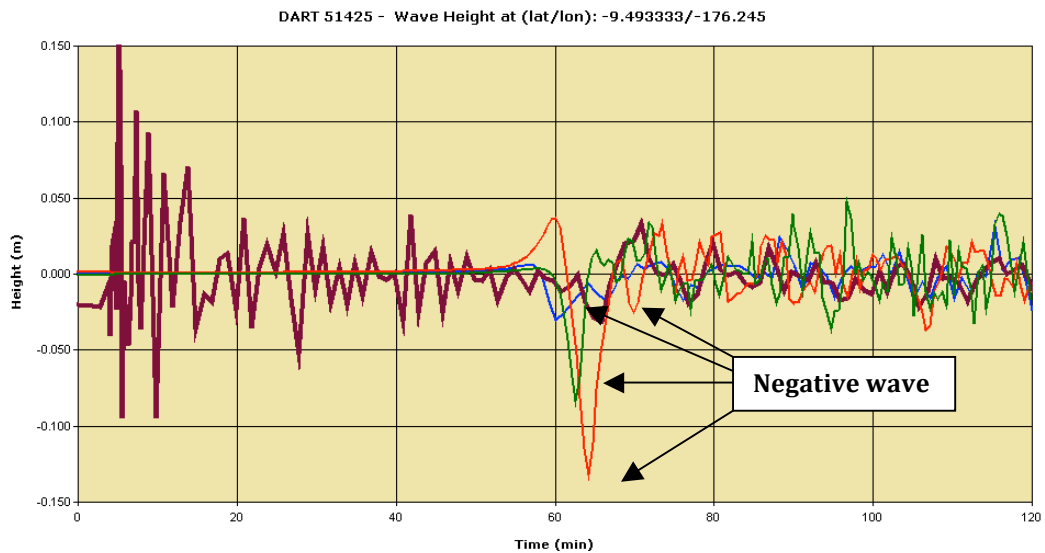


Figure 17 - Comparisons of DART 51425 level (brown) with simulations based on Harvard CMT (red), USGS CMT (blue) and Finite Fault Model (green)

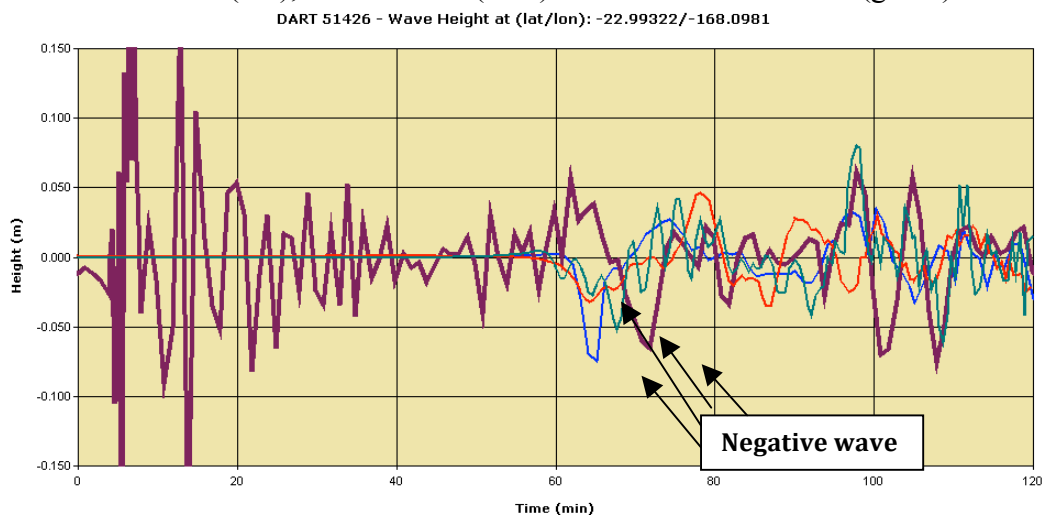


Figure 18 - Comparisons of DART 51426 level (brown) with simulations based on Harvard CMT (red), USGS CMT (blue) and Finite Fault Model (green)

In Figure 19 and Figure 20 the comparisons of buoy measurements with simulations performed using different fault models are shown. On both tidal buoys the first significant wave is negative as in the simulations. The arrival time of the simulations is anticipated in respect to the measurements. One can note that the tidal buoy measurements are not disturbed by the p-wave like on the DART, because a gravitational instrument is used. In Apia bay the simulated wave amplitude is on the same order as the measurements, while in Pago Pago bay they are halved.

The simulations show more oscillations when compared with measurements. Such behaviour can be explained by numerical problems that the finite difference models suffer when the wave approaches the coast.

Also for the buoys it can be stated that the Finite Fault Model provides the best wave simulations, while the Harvard CMT Fault model provides the worst ones.

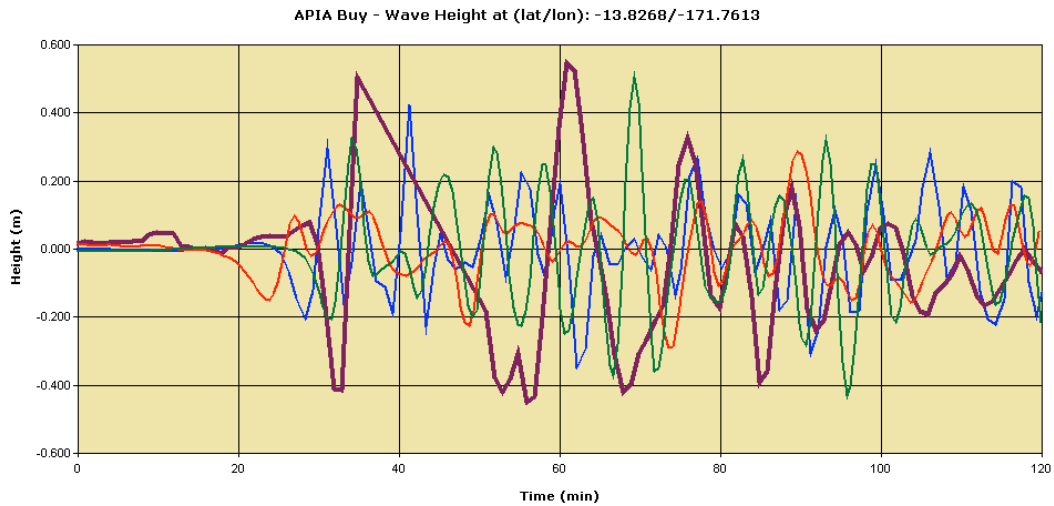


Figure 19 - Comparisons of Apia bay level (brown) with simulations based on Harvard CMT (red), USGS CMT (blue) and Finite Fault Model (green)

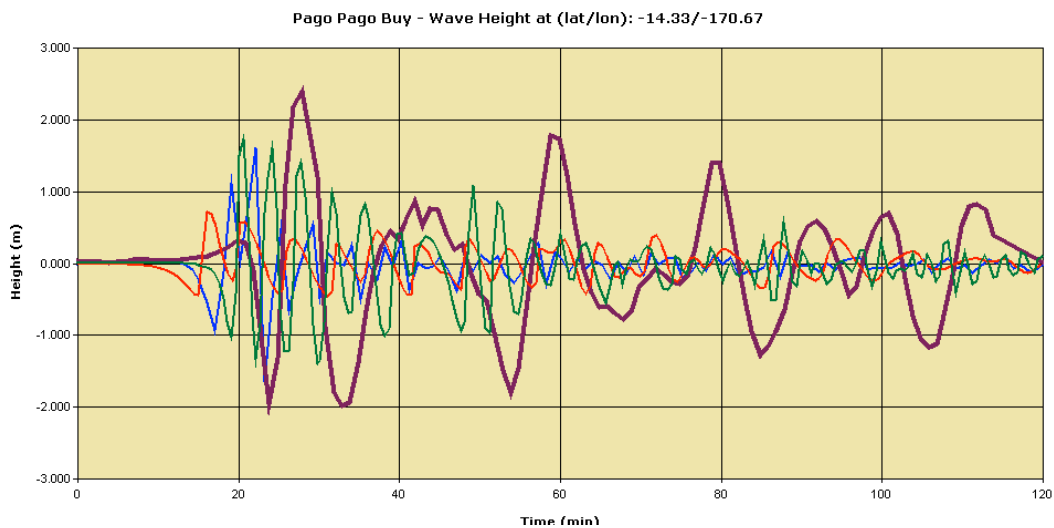


Figure 20 - Comparisons of Pago Pago bay level (brown) with simulations based on Harvard CMT (red), USGS CMT (blue) and Finite Fault Model (green)

4.2.2 Model assessment

In this section are shown the comparisons of the simulations performed by the SWAN JRC code, TUNAMI-N2 and HyFlux2, using as initial conditions the crust deformations provided by the Finite Fault Model. The grid size is 1800 m. In Figure 21 and Figure 22, the comparisons of DART measurements with simulations performed using different codes are shown. The first wave simulated by SWAN-JRC and HyFlux2 is exactly the same. TUNAMI-N2 shows small differences in respect to the previous ones. After the first wave, SWAN-JRC and TUNAMI-N2 show oscillations whose amplitude and frequency are not present in the measurement, and may be considered artefacts as a result of numerical instabilities. HyFlux2 simulations are smoother, with decreasing amplitude.

Similar behaviour can be noted in Figure 23 and Figure 24. The two Finite Difference codes, SWAN-JRC and TUNAMI-N2, continue to show oscillations which

are more evident in the second one, while the Finite Volume code, HyFlux2, is still smoother, but with waves that show lower amplitude in respect to the measurements and the results from the other codes.

The tendency in HyFlux2 code to provide smooth simulations (without numerical oscillations) is a desirable property because in such cases, when oscillations are predicted, they can be imputed to physical reasons and not to numerical artefacts. On the other hand, the results of HyFlux2 are damped: such behaviour disappears when the grid size resolution is higher, providing consistency with the geometry of the coastline. Simulations with higher resolution will be shown in the next section.

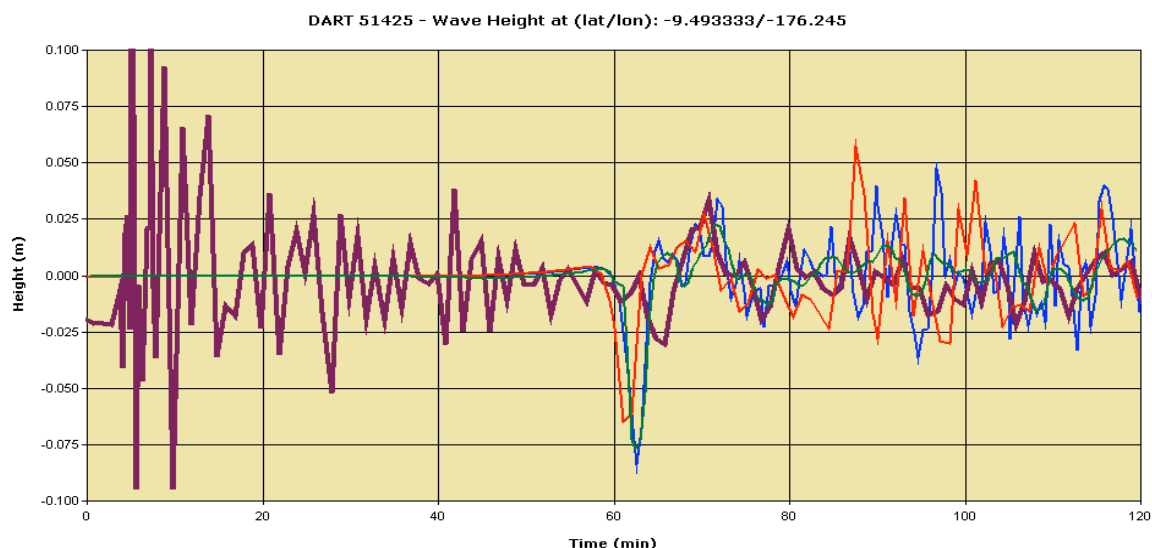


Figure 21 - Comparisons of DART 51425 level (brown) with simulations based on TUNAMI-N2 (red), SWAN JRC (blue) and HyFlux2 (green)

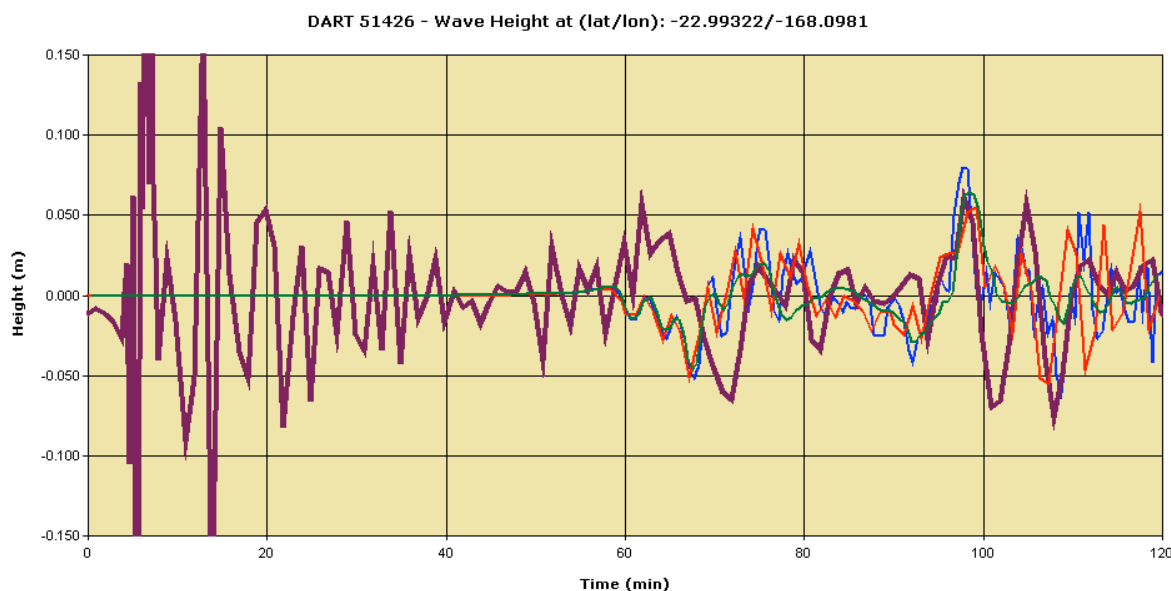


Figure 22 - Comparisons of DART 51426 level (brown) with simulations based on TUNAMI-N2 (red), SWAN JRC (blue) and HyFlux2 (green)

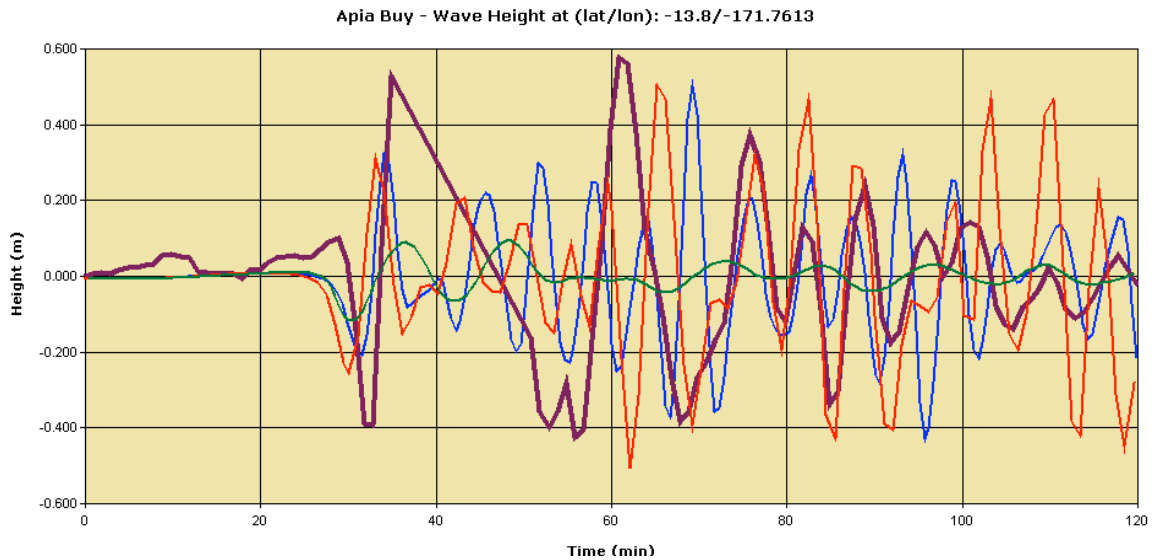


Figure 23 - Comparisons of Apia Bay level (brown) with simulations based on TUNAMI-N2 (red), SWAN JRC (blue) and HyFlux2 (green)

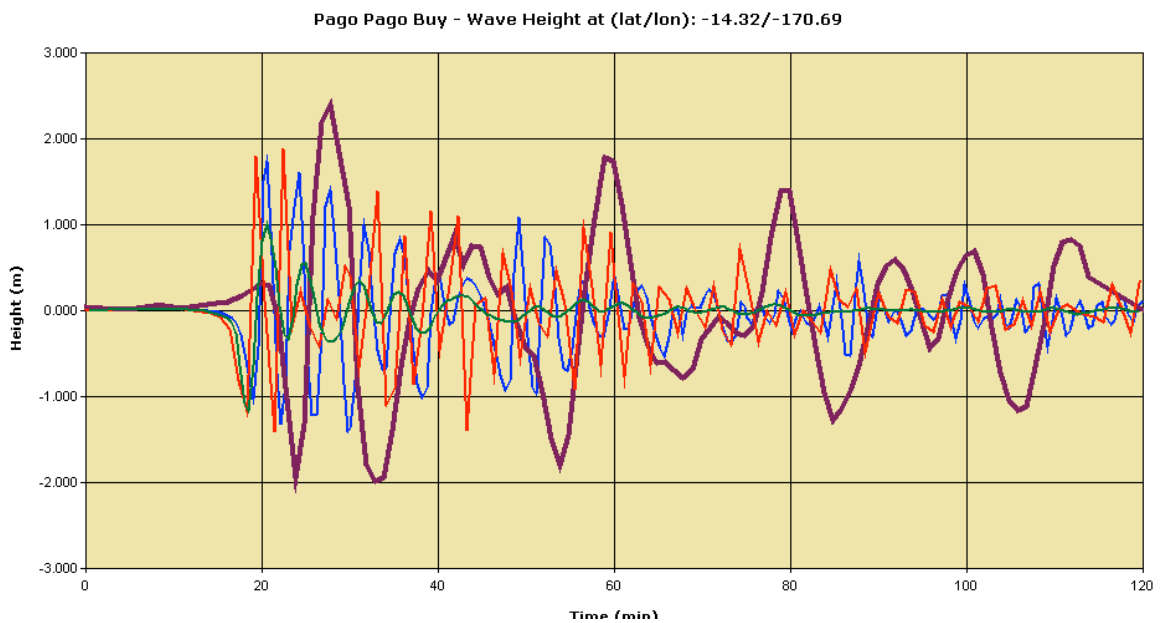


Figure 24 - Comparisons of Pago Pago Bay level (brown) with simulations based on TUNAMI-N2 (red), SWAN JRC (blue) and HyFlux2 (green)

5. INUNDATION MAPPING

The typology of the post event calculations depend on the objectives of the simulations and on the available DEM:

- *Early run-up area identification.* The objective here is to identify more precisely the affected locations and try to estimate the water level at the shoreline and the potential inundation in the various coastal areas. The requested grid size is on the order of 100 to 300m.
- *Inundation assessment.* The objective is to precisely identify the inundated area and run-up and evaluate the impact on buildings and infrastructure. The requested grid size is on the order of 10 to 30m.

The worldwide available DEM has a cell grid size of 30 arc sec (see Table 5), which corresponds to about 900m, so the best detailed simulation that can be done using such a source grid size cannot be significantly smaller. For the Samoa 2009 tsunami event, detailed DEM are also available for the American Samoa Island: this is an ideal opportunity to analyse which source grid size is the most suitable for the different simulation typologies and which are the most detailed simulations that can be done with the worldwide available 900m DEM grid size. In Table 7 are shown the performed runs.

Table 7 - Calculation grid size Vs source grid size. Calculation with grid size from 300m to 10m is nested from the coarser ones. The arrows indicate the flow of information for the nested simulations.

| | | Source Grid Size | | |
|---------------|------|------------------|--------|--------|
| | | 900 | 90 | 10 |
| Run Grid Size | 1800 | x | | |
| | 900 | x ↓ | | |
| | 300 | x ↓ | x ↓ | |
| | 90 | x | x ↓ | |
| | 30 | | x | x ↓ |
| | 10 | | | x |

Simulations with run grid size of 300m and less are done using the results of the coarser one as boundary conditions. The window is reduced in order to maintain the total number of cells on the order of 1 million. Such nested computational grids – from coarse the high-resolution – are used to have a minimum number of nodes spanning a wavelength in order to resolve the wave with finer detail, considering also that the wave length decreases when approaching the coast.

The reason for performing more detailed calculations in subsequent steps, with smaller window and cell size, is that the required CPU time increases as a cubic function of the cell size reduction, i.e., if the cell size is halved and the window remains the same, the number of cells becomes 4 times higher and the CPU time becomes 8 times higher. On the other hand, detailed information is useful only near the coast and not in the open sea where the wavelength is so long that coarse simulations represent well the real behaviour.

5.1 Early run-up area identification

The aim of this section is to describe how the geographical areas that could be affected by tsunami run-up are identified. When the wave reaches shallow water, its wavelength becomes shorter and the surface level rises, due to the conservation of energy. Such phenomena are emphasized in bay areas, where reflection and resonance

take place. Therefore it is necessary to adopt very detailed cells to be able to specify the bathymetry, the shoreline and the possible run-up topography. The precision of such information will strongly influence the simulation accuracy, and the capability of the code to reproduce the real phenomena.

Unfortunately the best resolution of the worldwide available data on bathymetry and topography is 30-arc sec (~ 900 m). To interpolate the available DEM to very low grid size (i.e. smaller than 100 m) does not make sense, considering that the elevation of hills and bays of size smaller than 1 km are averaged to one grid cell in an elevation model of 1km grid size. Therefore the compromise for a quick identification of the inundated area is to make simulations with 300 m grid size bathymetry, which is interpolated from the 900 m available information. With such resolution the wavelength at the shore is quite well represented, but the information on run-up distance is quite poor when the measured values are lower than 300m or when simulating waves entering into bays whose width or length is on the order of 1 km.

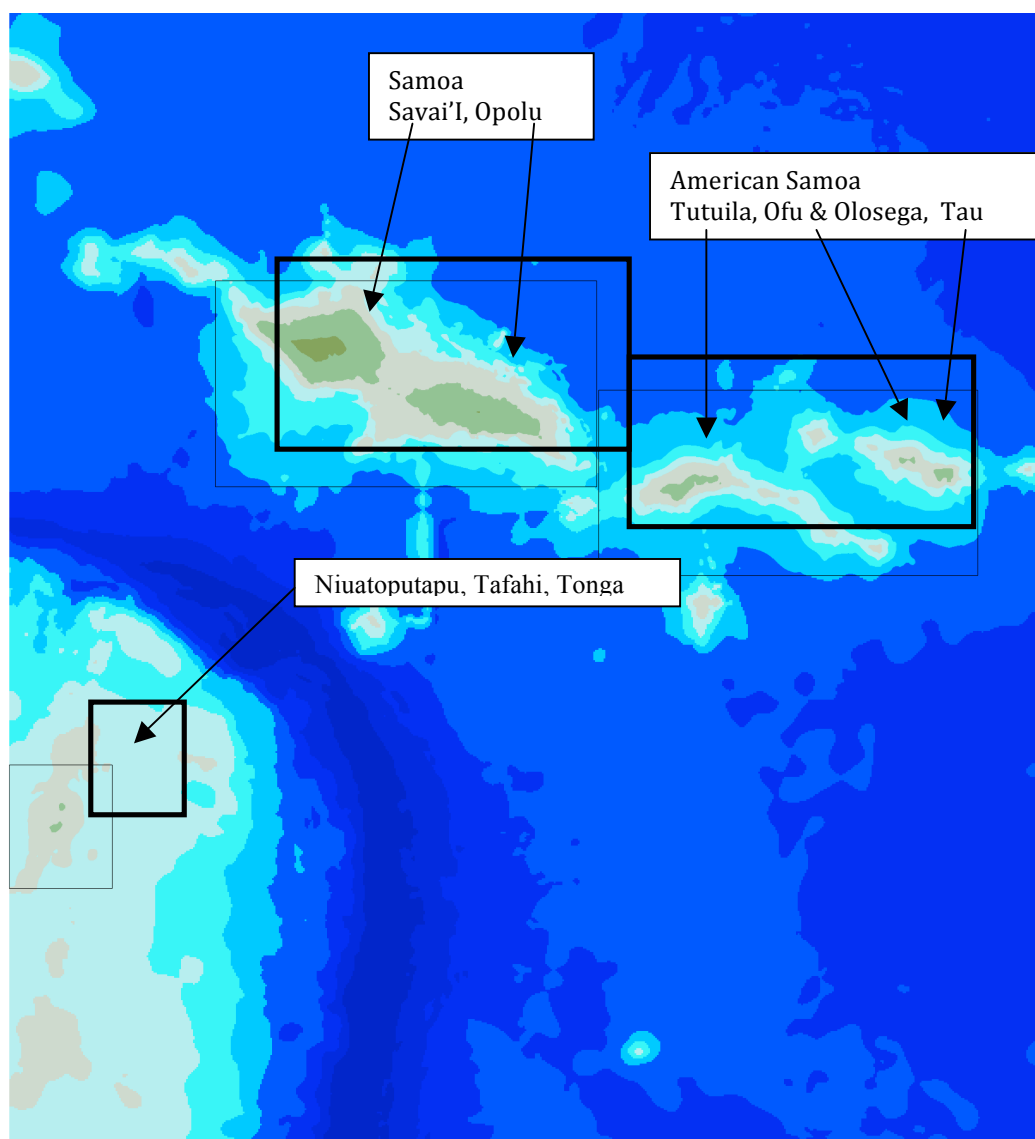


Figure 25 - Windows of the 300 m grid size nested simulations for early run-up identification.

Three nested simulations have been performed as indicated in Figure 25: the simulation result at 900 m grid size resolution (the larger window) is used as the boundary condition for the simulations with 300 m grid size (smaller windows). The crust deformation is provided by the Finite Fault Model.

HyFlux2 code has been used for inundation simulations. At identified (populated) locations, some estimation on the tsunami wave is provided. In Figure a sketch of the defined quantities is presented. All the quantities are evaluated within a 5 km radius from the point on the shoreline, which is the closest to the location of interest. Such a search radius decreases in case the simulation grid size resolution is very low and the number of localities in the search radius is high.

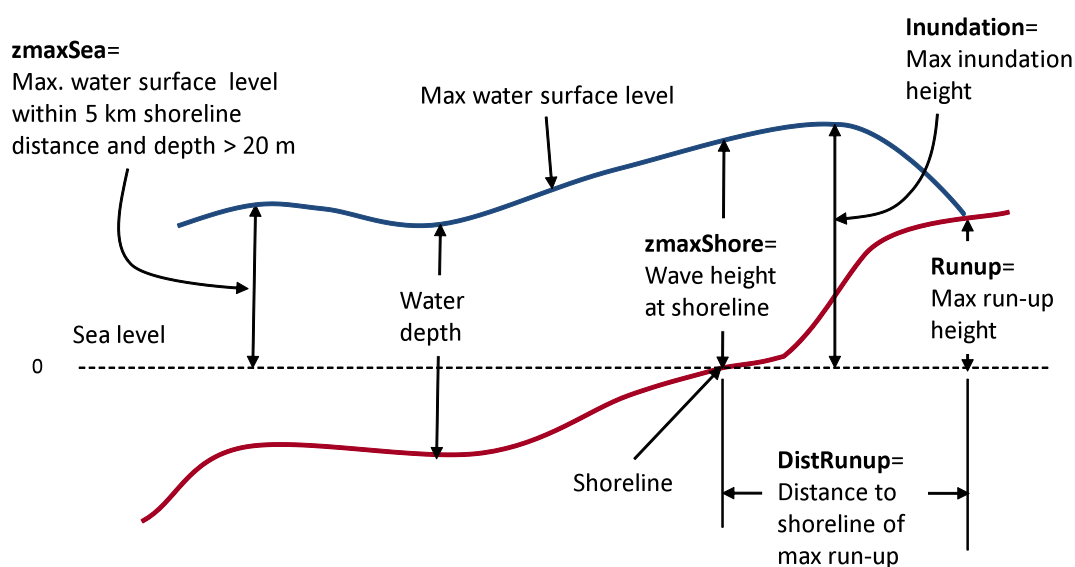


Figure 26 – Definitions on tsunami inundation quantities at selected evaluatee locations.

5.1.1 Saval'I and Opolu Island, Samoa

The Samoa Islands have been the most affected islands in the archipelago with more than 150 fatalities. The run-up areas and locations – identified by the simulation – are compared with the UNOSAT damage assessment image (Figure 27).

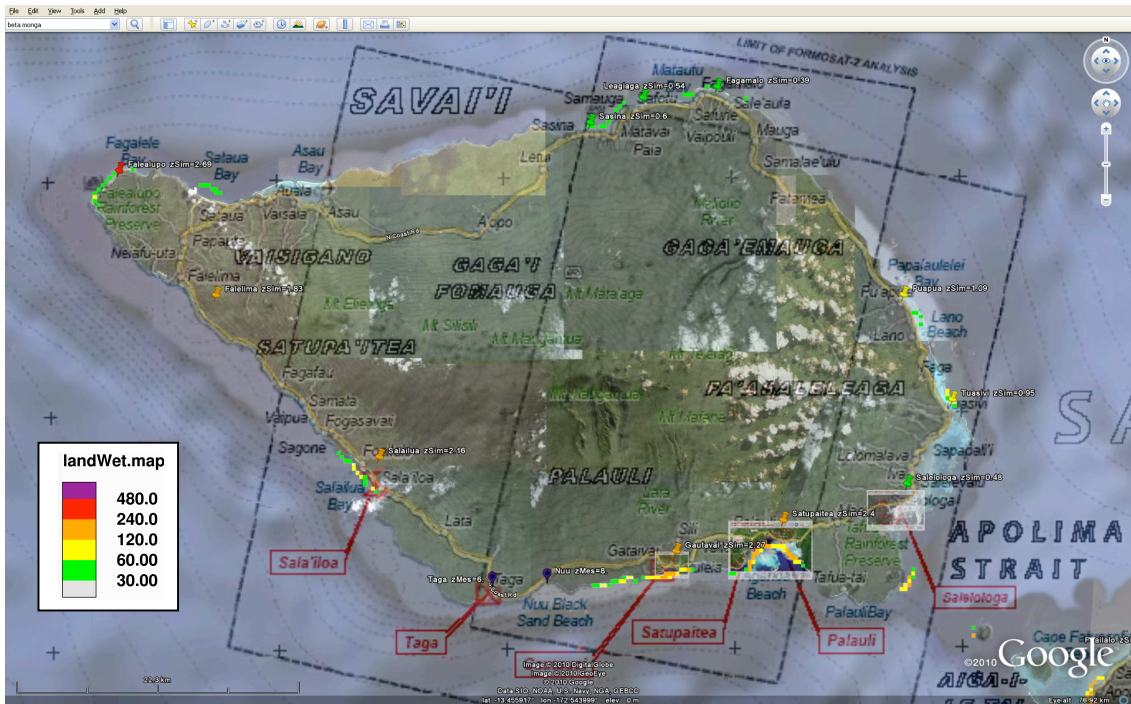


Figure 27 – Savai’i Island. Overlay of UNOSAT damage assessment map with the inundation map (landWet.map, distance from the shoreline [m]) and identified locations (push pin place marks).

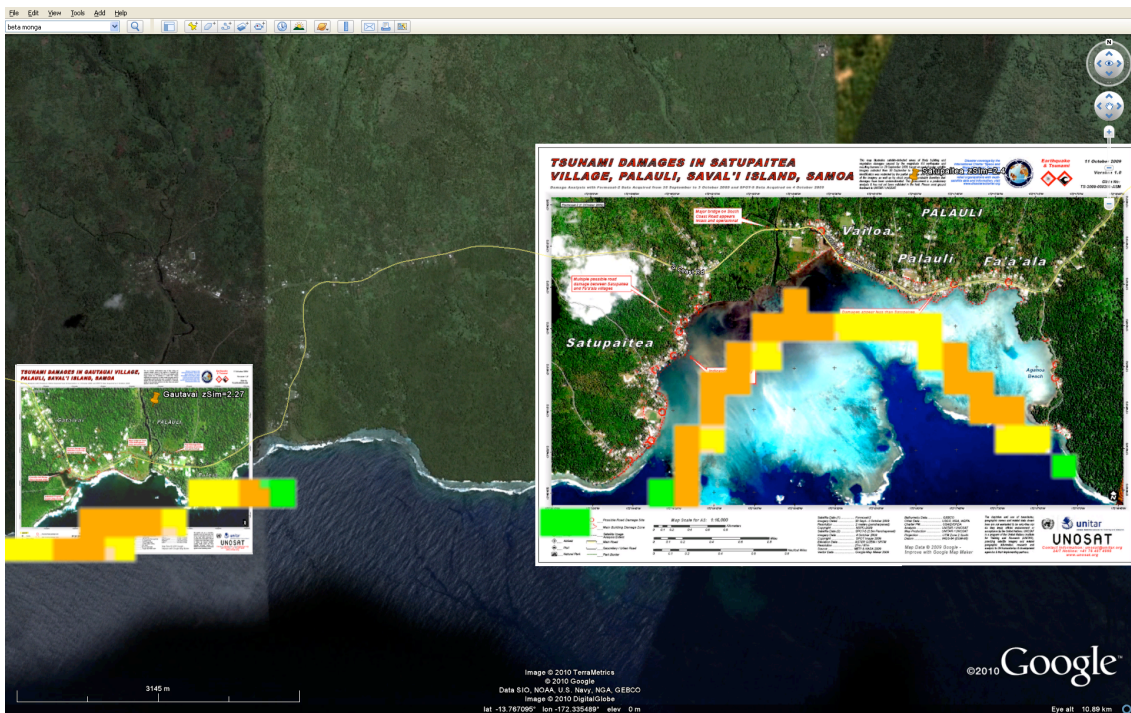


Figure 28 - Savai’i Island, Gautavi, Palauli, Satupaitea Villages. Overlay of UNOSAT damage assessment with the inundation map (landWet.map, distance from the shoreline [m]) and identified locations (place marks)

Most of the localities assessed by UNOSAT images are also identified by the simulations. In Saval'I Island Satupaitea locality, a maximum water height of 2.13 m has been simulated. In Figure 28 is a detail for some villages assessed by UNOSAT. It can be seen that, despite the rather coarse resolution (300m grid size) the simulation is able to identify the run-up areas like using images.

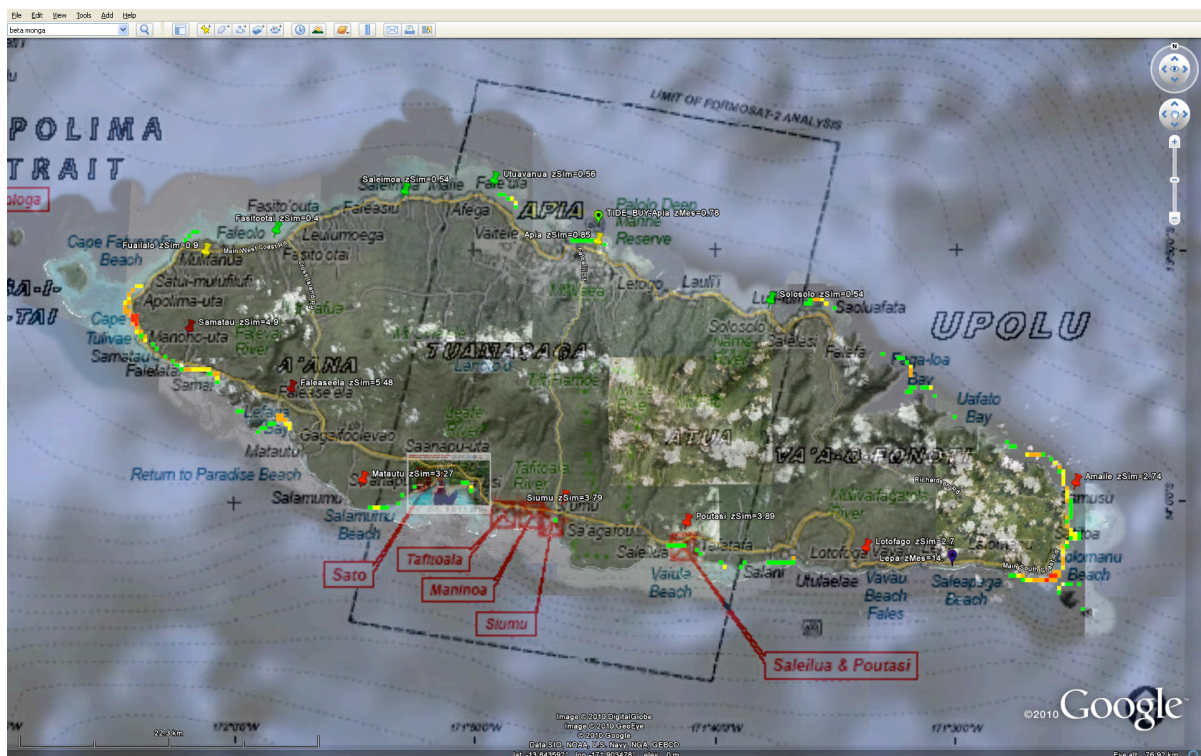


Figure 29 - Opolu Island. Overlay of UNOSAT damage assessment with the inundation map (landWet.map, distance from the shoreline [m]) and identified locations (push pin place marks)

On Opolu Island, Falease'ela locality, the maximum water height (simulated) reached 5.48 m. In addition, the simulations identify some localities in West and East side of Opolu Island that are not assessed by UNOSAT (Figure 8). In the Apia tidal buoy a maximum of 0.7m was measured (see Figure). Despite the fact that the buoy is downstream of the island, the simulated waves (amplitude, oscillation period and trend of decay) fit quite well with the available measurements.

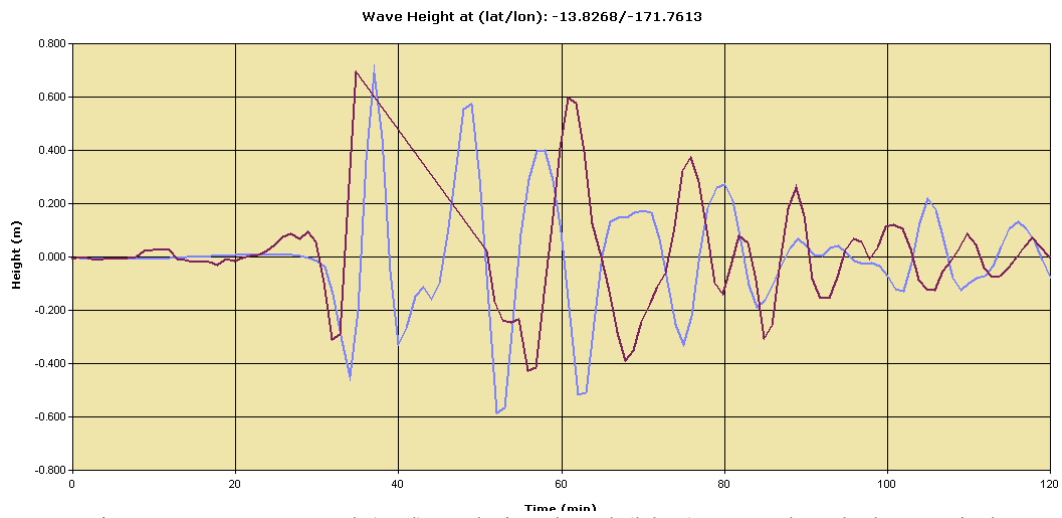


Figure 30 - Measured (red) and simulated (blue) water level at Apia bay. Measures from $t=34$ min and $t=51$ min are missing

5.1.2 Tutuila, Ofu & Olosenga, Tau, American Samoa

Tutuila Island was overcome by tsunami waves on the order of 5 to 7 m, with a splash height of 16 m in Poloa. There were 34 fatalities (see Table 1). The run-up areas and locations – identified by the simulation - are compared with UNOSAT damageassessment image (see Figure 31). In contrast to the Samoa Islands, where destruction was confined to the southern part, in Tutuila Island a significant impact has been measured (and simulated) on both the south and north coastlines. Note that the damage assessment based on satellite imaging has been performed only on the west part of the island because of cloud cover whereas the simulation and the post tsunami survey show inundations along the entire island coastline.

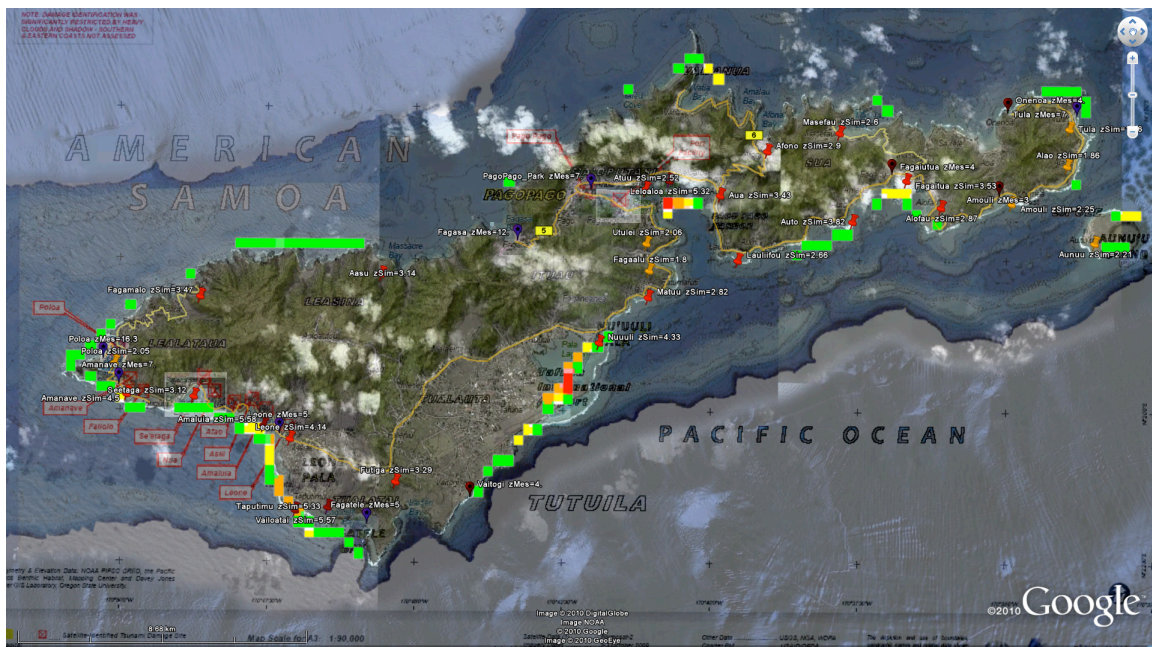


Figure 4 - Tutuila Island. Overlay of UNOSAT damage assessment with the inundation map (landWet.map, distance from the shoreline [m]), identified locations (push pin place marks) and post-tsunami survey (star place mark)

The negative wave reached Pago Pago Bay about 20 minutes after the initiating event, followed by a subsequent positive wave 5 minutes later. A comparison of the simulation results with the tidal buoy measurement is shown in Figure 32. The first wave is simulated quite well, but the frequency of the subsequent waves is different from those measured. These differences could be explained by the poor horizontal accuracy of the DEM, which makes the simulated bay shorter than the real one, with resulting differences between the simulated and measured wave period.

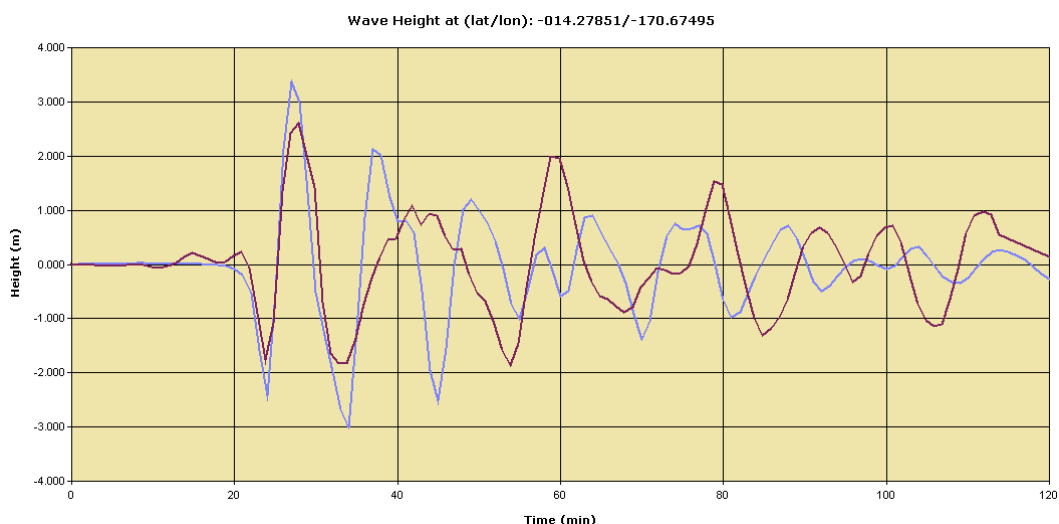


Figure 32 - Measured (red) water level at Pago Pago bay compared with simulated water height in a point out of the shoreline (blue)

Ofu, Olosega and Tau islands (east of Tutuila Island) were the islands with the highest simulated water run-up (see Figure 33). A maximum water level of 11 m was simulated in Ofu and 7 m in Olosega (measured 6.1m and 4m respectively). At Tau a maximum water level of about 5 m was simulated, while the measured level was 12 m.

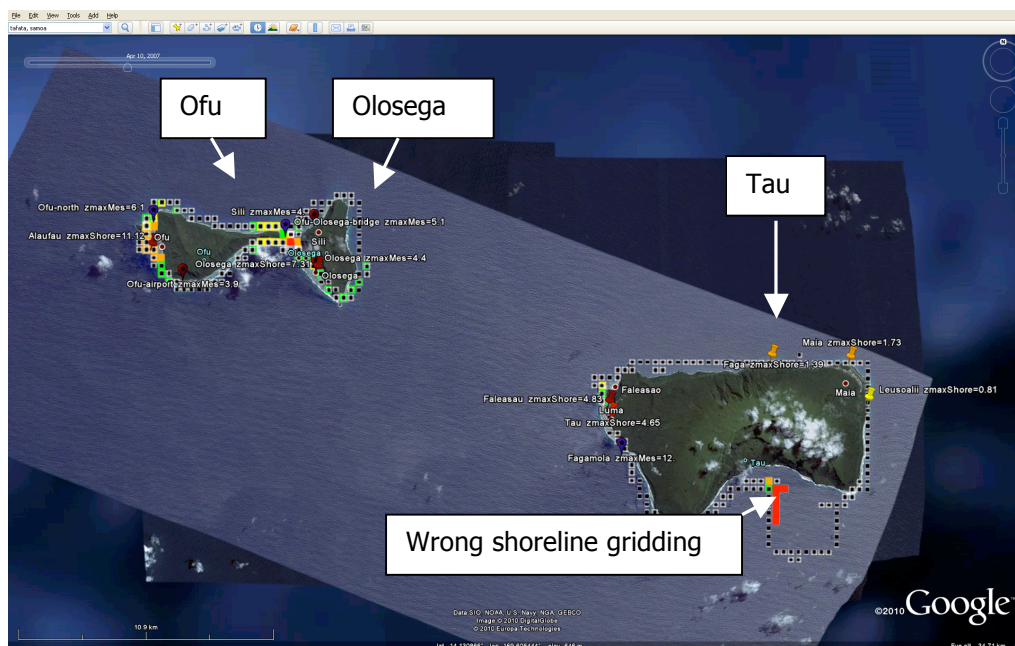


Figure 33 - Ofu, Olosega, Tau Isl. Inundation map and identified locations.

In Figure 34, a comparison of measure data and code simulations is shown. The numerical model under predicted the measurements in Tutuila, over predicted in Ofu & Olosega Islands, and under predicted again in Tau Island. The average of the ratio between prediction and measurement is 0.73 in Tutuila and Tau Island, while it is about 1.66 in Ofu & Olosega. Such differences, as discussed above, can be explained by the coarse and sometimes inappropriate shoreline gridding.

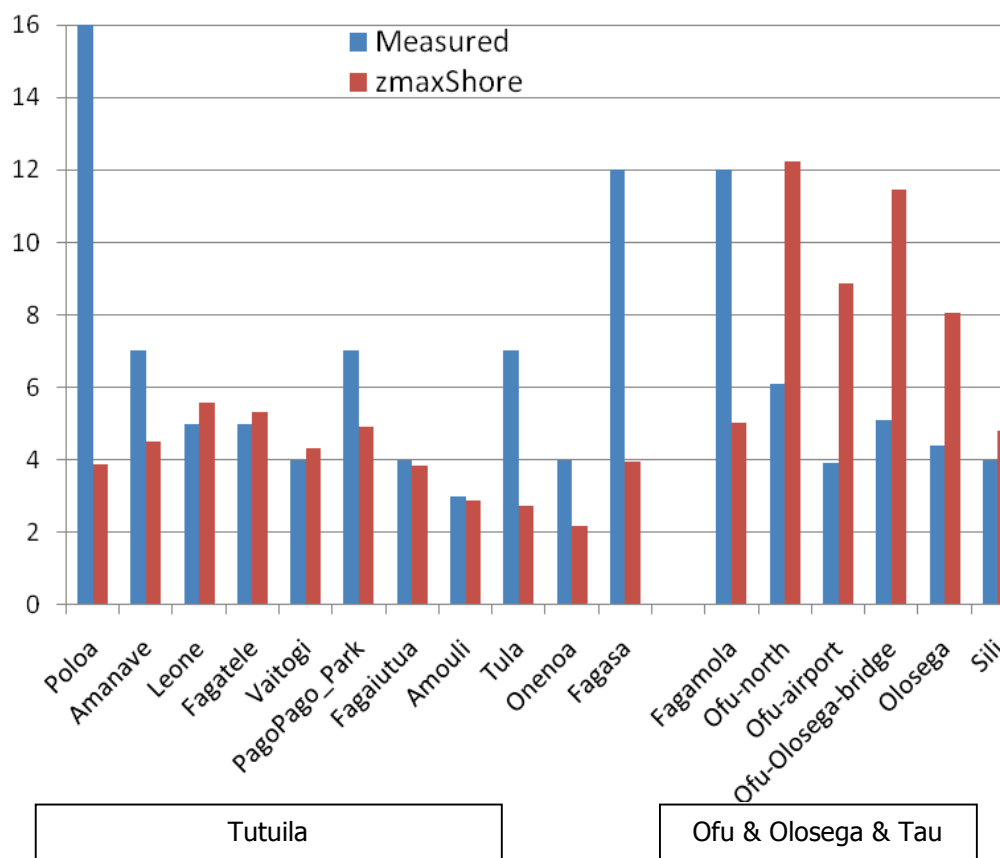


Figure 34 - Comparisons of measured run-up with the simulated water surface level at the shoreline (zmaxShore).

5.1.3 Niuatoputapu & Tafahi, Tonga

The tsunami impact on these islands was very high. A maximum run-up (EERI, 2010) of 22 m was measured at Tafahi Island and 15 m at Niuatoputapu Island, while maximum water surface level of about 7 m was simulated at both the islands. Major impacts have been surveyed along the east coast. The extended coral reef reduced the impact on villages on the west and north sides of the coastlines. In Figure 35 is shown the inundation map, which is qualitatively confirmed by the observations.

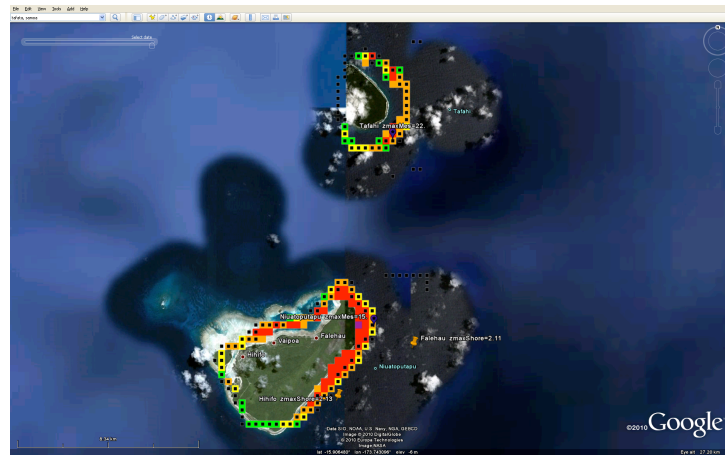


Figure 35 - Niuatoputapu, Tafahi Island. Inundation map and identified locations.

6 INUNDATION ASSESSMENT

The objective of an inundation assessment is to quantify the inundation extent in identified run-up areas. For this purpose, the use of high-resolution grids is necessary not only in ensuring accuracy and reliability of the simulations but is essential when describing local details like narrow bays, estuaries, harbours or in general any run-up areas affected by inundation.

In Figure 36, simulations with 300 and 90 m grid size respectively are shown. On both maps, the inundated localities are identified but, due to the coarse accuracy of the source data, the coastline is smoothed and the quantification of the inundation area obtained by the finer 90m simulation is not reliable. Increasing the simulation accuracy is not enough when the objective is to identify the extent of the inundated area. Therefore DEM data with higher accuracy is necessary for better inundation assessment.

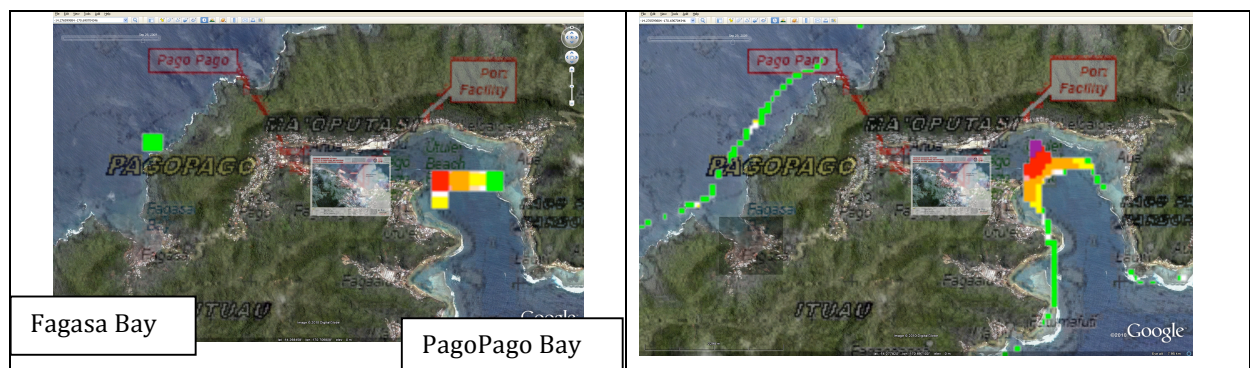


Figure 36 - Pago Pago and Fagasa bays. Inundation maps for simulations with grid size 300m (left) and 90m (right) interpolated from 900m grid (STRM30+)

For the Samoa 2009 Tsunami event, detailed DEM - 3 arc-second and 1/3 arc-second data, which correspond to about 90m and 10m - are available for the American Samoa Islands (see Table 5 and E.Lim, 2010). This very rare DEM availability provides an ideal opportunity to assess the HyFlux2 capabilities on inundation simulation. Another important issue is to analyse which grid-size simulation is the most suitable for inundation assessment: this is not a trivial exercise considering that the computer resources needed (CPU time and memory) drastically increase with increasing accuracy of the simulations.

Nested simulations with 90m, 30m and 10m-grid size accuracy have been performed. In Figure 37 are presented the inundation maps produced by 90 m (left) and 30 m (right) grid size simulations. In both simulations the DEM has been interpolated from a 90m grid. Contrary to the simulation performed at the same grid size (90 m) but interpolated from 900m, now the shoreline is captured more correctly, providing hot spots much more consistent with the observations. With 30m-grid size simulation the run-up line and inundation extent is captured with more detail.

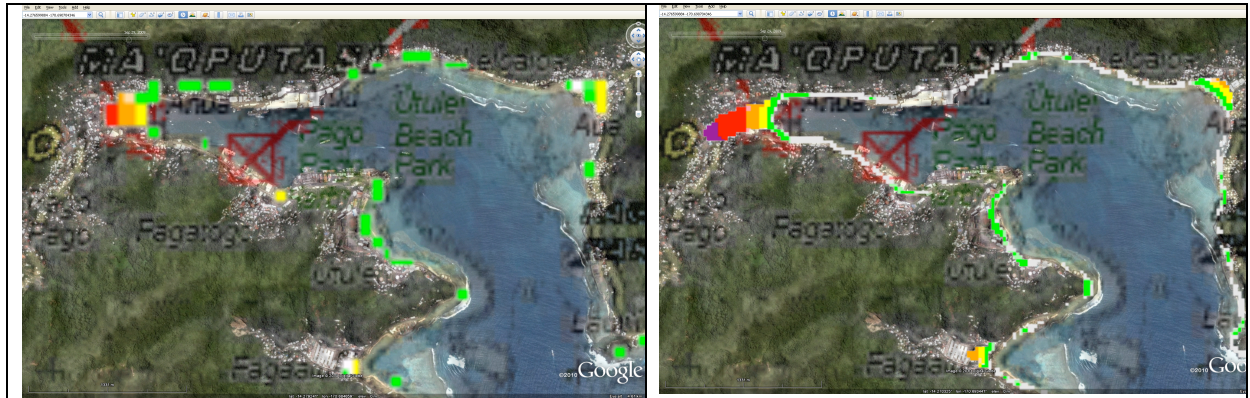
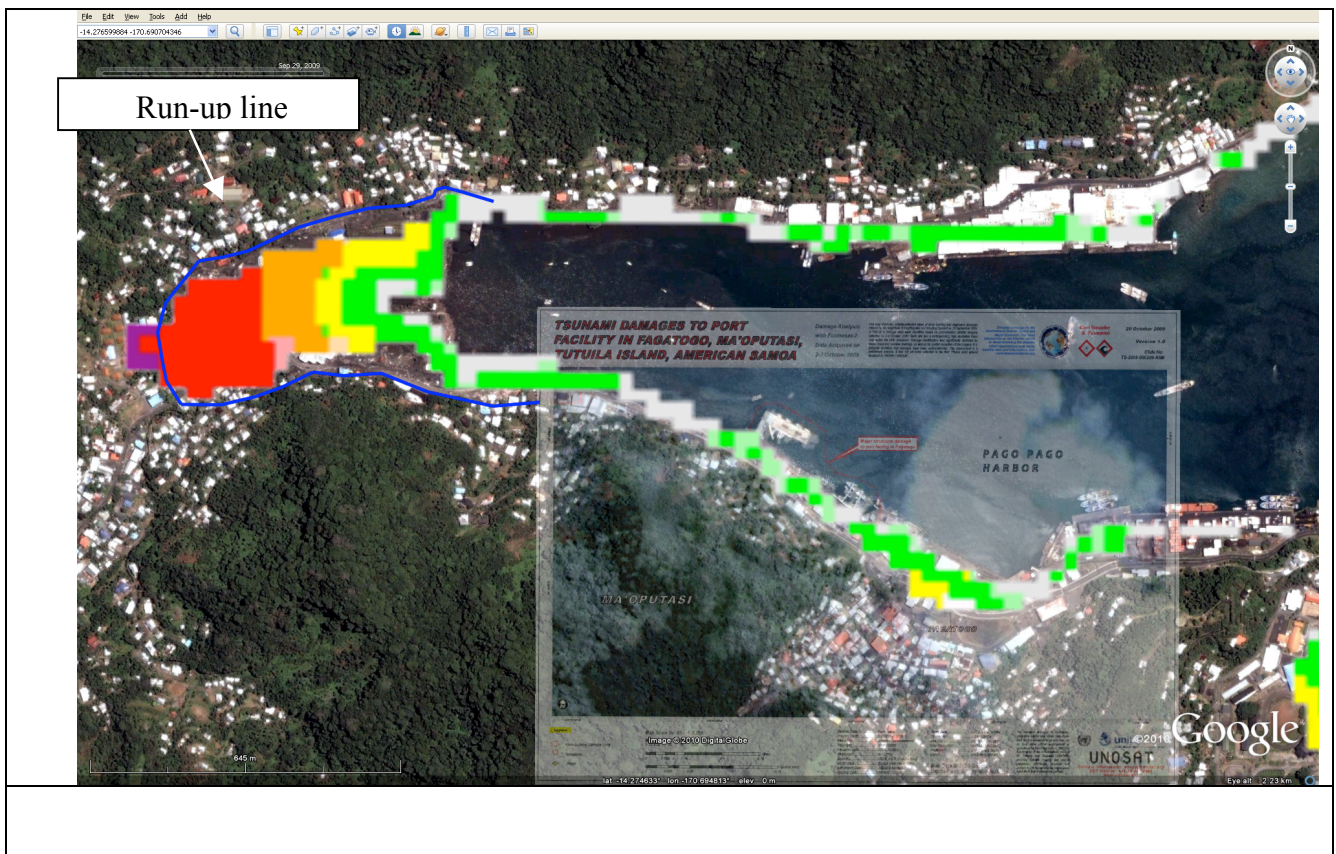


Figure 37 - Pago Pago bay. Inundation maps for simulations with grid size 90m (left) and 30m (right) interpolated from 90m grid (NOAA - AS 3 arc-second Pago Pago, see Table 5)

In Figure 38, inundation maps are presented produced by 30m (top) and 10m (bottom) grid size simulations, using a DEM interpolated from a 10m-grid size. The extra effort in CPU time (factor of 27) and memory (factor of 9) spent in producing the 10m simulation is not compensated by the negligible increase in accuracy of the results.



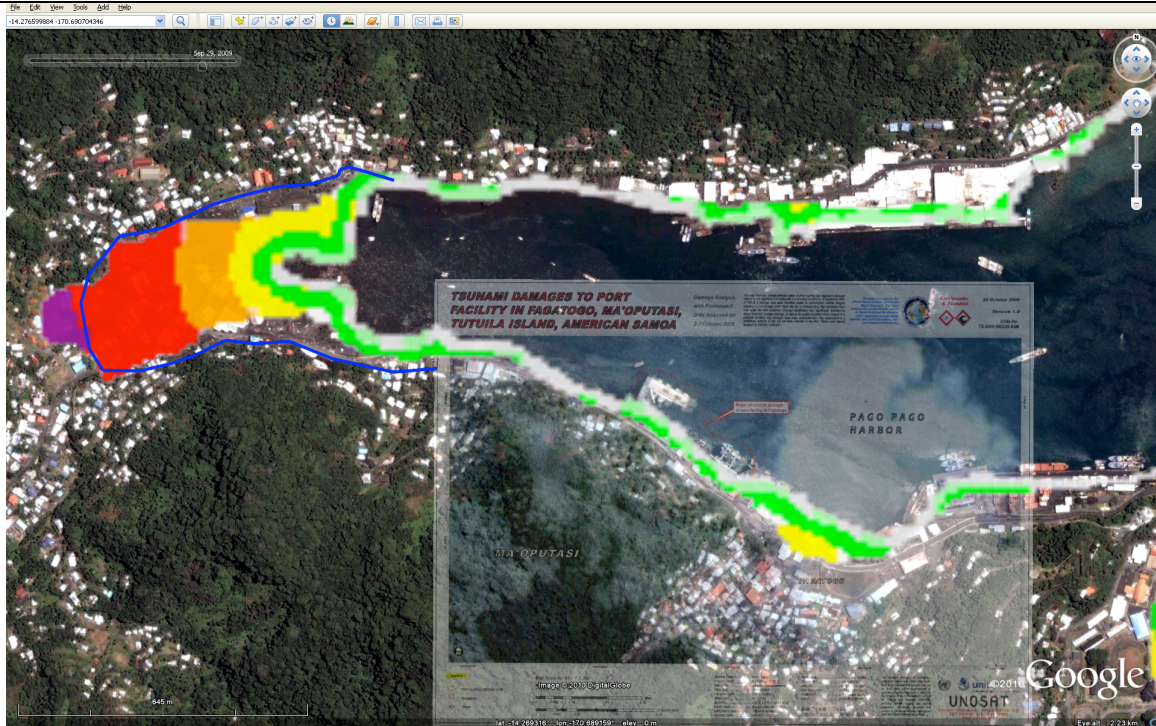


Figure 38 - Pago Pago Bay. Detailed inundation maps for simulations with grid size 30m (top) and 10m (bottom) interpolated from 10m grid. (NOAA - AS 1/3 arc-second Pago Pago, see Table 5)

In Figure 39, the inundation maps at 30m-grid size resolution are shown, with the DEM interpolated from 90m and 10m-grid size respectively. Only in the airport region did the inundation maps show a different degree of detail. In general, a 30m-grid size simulation is sufficient when an inundation assessment is required. A 10m (or smaller) grid size simulation could be of interest in case an impact assessment on buildings and local infrastructure is required.

The numerically simulated inundation maps performed at 30m grid size resolution are at least as accurate as the satellite image maps; however, with the simulations, additional locations not assessed by satellite images have been identified. It is worthwhile to note that the damage assessment performed through satellite imaging was significantly restricted by heavy clouds and shadow, so the southern and eastern coasts in Tutuila Island were not assessed.

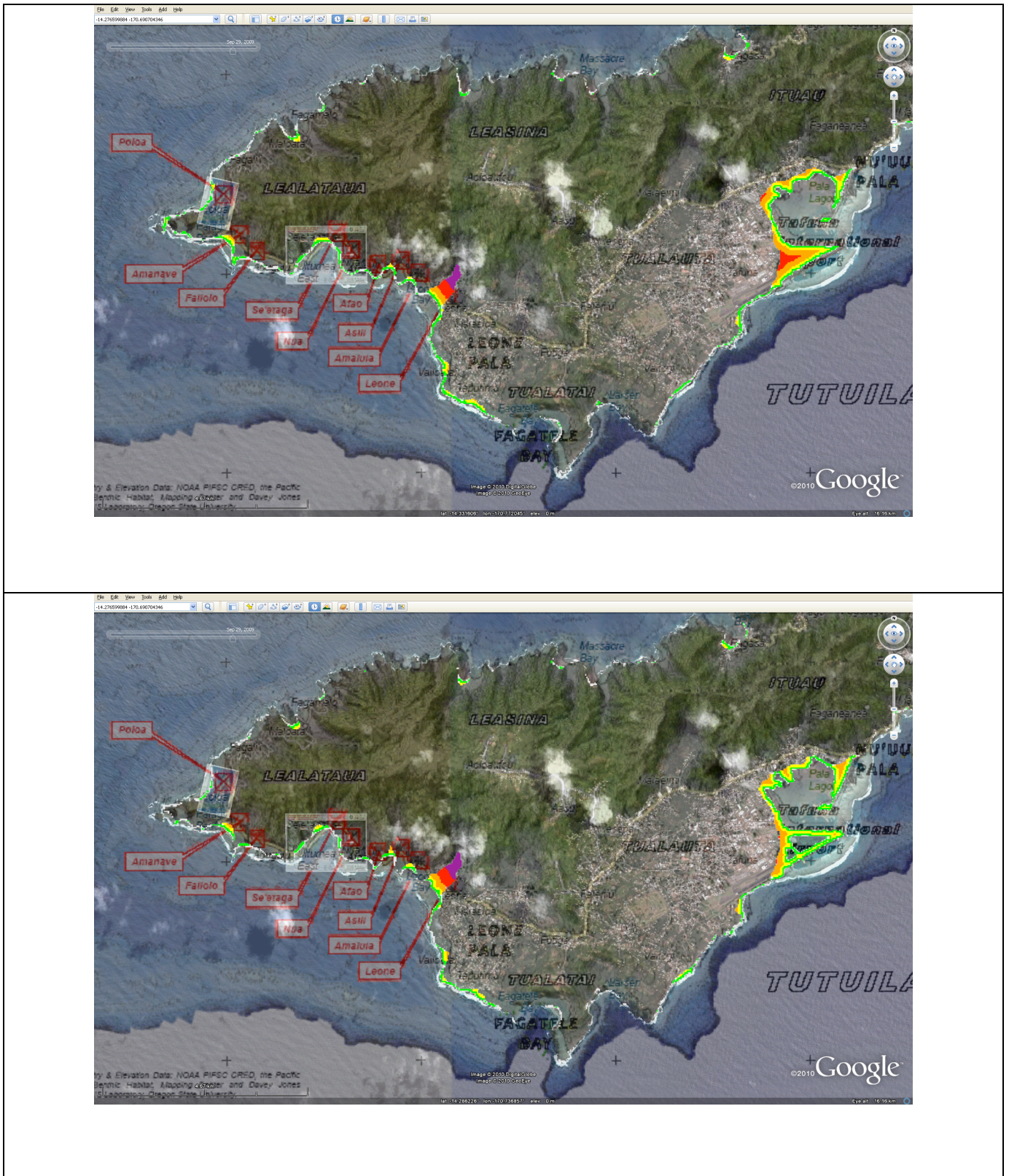


Figure 39 - East of Tutuils Isl. - Inundation maps for simulations with 30m grid size, interpolated from 90m grid (top) and 10m grid (bottom)

In Figure 40, a comparison of the post-tsunami survey measurements and simulation results are shown. The following observations can be drawn:

- Increasing the simulation accuracy, the simulated average $z_{maxShore}$ increases,

- from 1.1 m (1800 m run grid size) to 6 m (30 m run grid size). With the same simulation accuracy (but different data sources grid size), the simulated averages are more or less the same, but with different values considering the localities individually. This is particularly true for the 300 m and 90 m grid size runs.
- The average maximum height at the shore of 3~4 m has been calculated by a 300m run grid size: the same values in open sea were calculated also by the near-real time calculations performed at 4800 m grid size, but with a conservative fault (see section 4.1).
- The standard deviation (*stdev* in Figure 40) of the measurements (about 4 m) is rather high when comparing with the average value (6.8 m). This could indicate that, sometimes, values that are not representative of the area are included into the observations, such as local “splashes” due to 2D steep gradients in the DEM, i.e., the measurements in Poloa (16.3m) and Fagasa (12m) could correspond to such cases.
- The standard deviation of the simulations continues to increase with increasing simulation accuracy, from 0.4m (1800m run grid size) to about 2m (10m run grid size). To reach the standard deviation of the measurements should require a very high accuracy, at least on the order of several meters, including in the bathymetry/topography the influence of buildings, roads and other infrastructures.

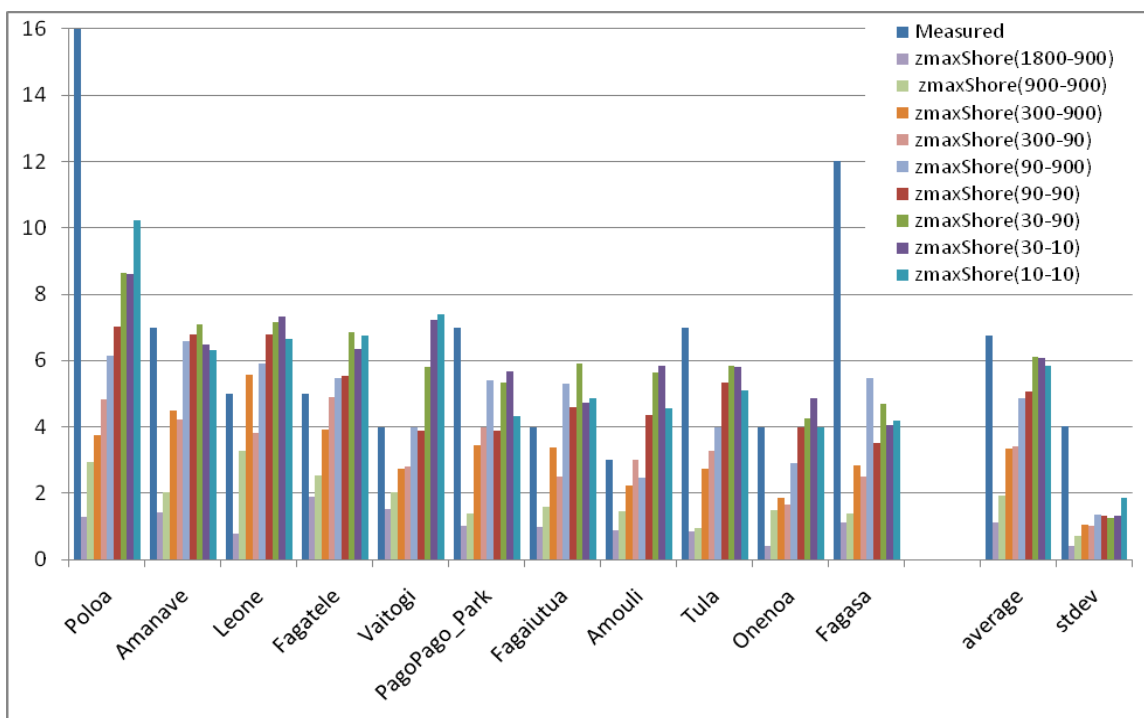


Figure 40 - Tutuila Island. Comparisons of measured run-up with the simulated water surface level at the shoreline. The labels zmaxShore (x-y) indicate simulations performed at x grid size, with DEM interpolated from y data source grid size

In Figure 41 are compared the inundation quantities evaluated at the localities where a maximum water height has been measured. In all these localities the trend is similar, indicating that the code is able to capture the physical run-up process. The average ratio between maximum inundation level and maximum surface level on the sea is about 1.46 ± 0.3 .

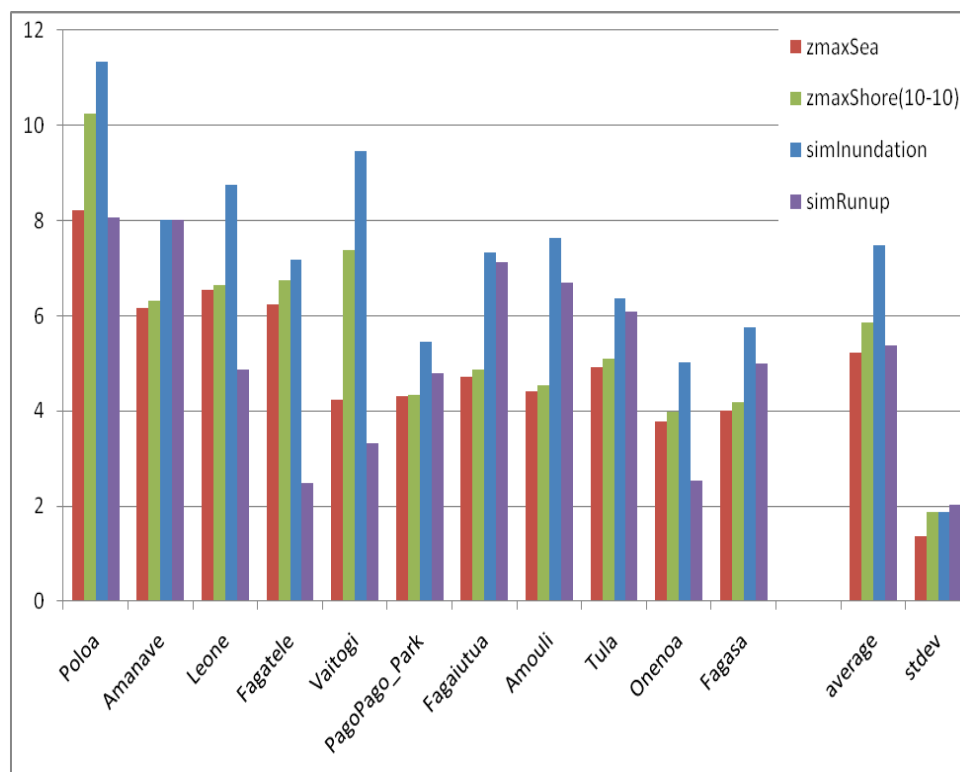


Figure 41 - Tutuila Island. Comparisons of tsunami inundation quantities (see also Figure 26 for definitions) evaluated by a 10 m run grid size

7 CONCLUSIONS

This report highlights the characteristics and impact of the tsunami that occurred in Samoa on 29 September 2009, describing the event, the available measurements in the months after the event and the seismological situation of the area.

It was shown that the GDACS system was able to give a correct preliminary estimate of the scale of the event, indicating which islands were likely to be affected by tsunami run-up.

An assessment of the simulation results of the SWAN-JRC code (used by GDACS) obtained from the initial conditions calculated by different fault models indicates that the Finite Fault Model best represents the event. The assessment also considers several hydrodynamic models, indicating that the wave propagation is modelled with the same level of accuracy by the SWAN-JRC, TUNAMI and HyFlux2 codes, despite the fact that the first two codes use a finite difference modelling approach while the third, developed particularly for inundation modelling, is a finite volume model. Differences between the codes have been seen when the wave approaches the coastline, showing oscillations in the results of the finite difference codes.

In order to draw up a more detailed map of the situation, finer calculations were performed after the event using the HyFlux2 code, identifying the most severely affected areas. It was concluded that a 300 m run grid size is adequate for early identification of the run-up area.

It was also attempted to evaluate the extent of inundation using a detailed digital elevation model, available for the American Samoa. The flooded areas for which we had satellite images and a post tsunami survey were in effect flooded and the extent of the maximum water surface level was estimated with a good accuracy.

It was concluded that a 30m run grid size is enough to estimate the flooding extent. Additional flooded areas not assessed by the satellite images - because of heavy clouds and shadow when the images were acquired - have been identified by the hydrodynamic simulations.

8. ACKNOWLEDGMENTS

The authors wish to thank Brian Worth for the careful reading and editing of the manuscript.

9 BIBLIOGRAPHY

Annunziato A. The Tsunami Assessment Modelling System by the Joint Research Centre [Article] // Science of Tsunami Hazards. - 2007. - Vol. 26(2).

Annunziato A., Franchello, G., Ulutas, E., De Groeve, T. 29 September 2009 Samoa Tsunami [Report] : JRC Scientific and Technical Reports. - [s.l.] : European Communities, 2009. - EUR Report 24068 EN.

Audusse E. [et al.] A fast and stable well-balanced scheme with hydrostatic reconstruction for shallow water equations [Journal]. - [s.l.] : SIAM J.Sci.Comp., 2004. - Vol. 25 (6). - pp. 2050-2065.

Beaven J. [et al.] Near-simultaneous great earthquakes at Tongan megathrust and outer rise in September 2009 [Journal]. - [s.l.] : Nature, 2010. - doi:10.1038/nature09292.

Brufau P. and Garcia-Navarro P. Unsteady free surface flow simulation over complex topography with a multidimensional upwind technique [Journal]. - [s.l.] : Journal of Computational Physics, 2003. - 2 : Vol. 186. - pp. 503-526.

Cruz A., Krausmann E. and Franchello G. Analysis of tsunami impact scenarios at an oil refinery [Article] // Natural Hazards. - [s.l.] : Springer Netherlands, 2010. - 10.1007/s11069-010-9655-x.

EERI Samoa Earthquake and Tsunami of September 29, 2009 [Online] // EERI Earthquake Engineering Research Institute. - January 2010. - September 22, 2010.

Franchello G. and Krausmann E. HyFlux2: a numerical model for the impact assessment of severe inundation scenario to chemical facilities and downstream environment [Report] : JRC Scientific and Technical Reports. - 2008. - EUR 233354 EN, ISSN 1018-5593E.

Franchello G. Modelling shallow water flows by a High Resolution Riemann Solver [Report] : JRC Scientific and Technical Reports. - 2008. - EUR 23307 EN.

Franchello G. Shoreline tracking and implicit source terms for a well balanced inundation model [Article] // Int. Journal for Numerical Methods in Fluids. - [s.l.] : Wiley, 2010. - Vol. 63. - pp. 1123-1146. - <http://www3.interscience.wiley.com/journal/122528271/abstract>.

Imamura F., Yalciner C. and Ozyurt G. Tsunami Modelling Manual (TUNAMI model) [Online] // DCRC -Tsunami Engineering Laboratory, TOHOKU University. - 2006. –

<http://www.tsunami.civil.tohoku.ac.jp/hokusai3/J/projects/manual-ver-3.1.pdf>.

Ji C., Wald D. J. and Helmberger D. V. Source description of the 1999 Hector Mine, California, earthquake, part I: Wavelet domain inversion theory and resolution analysis [Article] // Bull. Seismol. Soc. Am.. - 2002. - Vol. 92. - pp. 1192-1207.

Lay T. [et al.] The 2009 Samoa-Tonga great earthquake triggered doublet [Journal]. - [s.l.] : Nature, 2010. - doi:10.1038/nature09214.

Liang Q. A structured but non-uniform Cartesian grid-based model for the shallow water equations [Journal]. - [s.l.] : Int. J. Numer. Meth. Fluids, 2010. - DOI: 10.1002/flid.2266.

Liang Q. Flood simulation using a well balanced shallow flow model [Journal]. - [s.l.] : Journal of Hydraulic Engineering, 2010. - 669 : Vol. 136. - doi:10.1061/(ASCE)HY.1943-7900.0000219 .

Liang Q. Simulation of dam- and dyke-break hydrodynamics on dynamically adaptive quadtree grids [Journal]. - [s.l.] : Int. J. Numer. Meth. Fluids, 2004. - Vol. 46. - pp. 127-162. - DOI: 10.1002/flid.748.

Lim E. [et al.] Digital Elevation Models of Pago Pago, American Samoa: Procedures, Data Sources and Analysis [Online] // Tsunami Inundation Gridding Project | ngdc.noaa.gov. - 2009. –

http://www.ngdc.noaa.gov/mgg/inundation/tsunami/data/pago_pago_as/pago_pago_as.pdf.

Mader C. Numerical modeling of water waves [Book]. - [s.l.] : CRC Press, 2004. - ISBN 0-8493-2311-8.

Marche F. Theoretical and Numerical Study of Shallow Water Models. Applications to Nearshore Hydrodynamics. [Online]. - PhD Thesis; Université de Bordeaux, 2005. –

http://www.math.u-bordeaux.fr/~marche/THESE_Marche.pdf.

OCHA Samoa-Tonga Tsunami OCHA Situation Report No. 6 [Online] // ReliefWeb. - 6 October 2009. –

<http://www.reliefweb.int/rw/rwb.nsf/db900sid/AZHU-7WL2CX?OpenDocument>.

Okada Y. Surface deformation due to shear and tensile faults in a half-space [Article] // Bulletin of the Seismological Society of America.. - 1985. - Vol. 75. - pp. 1135-1154.

Pararas-Carayannis G. and Dong B. CATALOG OF TSUNAMIS IN THE SAMOA ISLANDS [Online] // <http://www.drgeorgepc.com/TsunamiSamoaIslandsCatalog.pdf>. - 1980.

Pelletier B., Calmant S. and Pillet B. Current tectonics of the Tonga–New Hebrides region [Article] // *Earth and Planetary Science Letters*. - 1998. - Vol. 164. - pp. 263-276.

Titov V.V, and Gonzales F.I. Implementation and testing of Method of Splitting Tsunami (MOST) model [Report] : Technical Memorandum / ERL PMEL ; NOAA. - 1997.

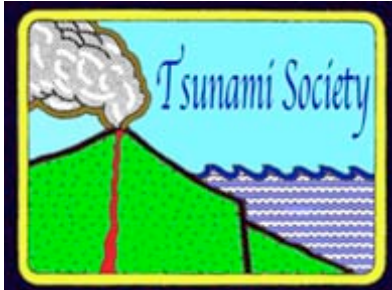
Titov V.V. [et al.] Real-time tsunami forecasting: Challenges and solutions [Article] // *Natural hazards*. - 2005. - Special Issue, U.S. National Tsunami Hazard Mitigation Program : Vol. 35(1). - pp. 41-45.

UNITAR/UNOSAT Tsunami in Samoa Island [Online] // International Space Charter website. - 29 09 2009. - 27 09 2010. - http://www.disasterscharter.org/web/charter/activation_details?p_r_p_1415474252_assetId=ACT-273.

Ward S.N. Tsunamis, *Encyclopedia of Physical Science and Technology* [Book] / ed. Meyers R.A.. - [s.l.] : Academic Press., 2002. - Vol. 17 : pp. 175-191.

Weinstein S. Lundgren P. Finite Fault Modeling in a Tsunami Warning Center Context [Journal]. - [s.l.] : *Pure and Applied Geophysics*, 2008. - Vol. 165. - pp. 451-474. - DOI 10.1007/s00024-008-0316-x.

ISSN 8755-6839



SCIENCE OF TSUNAMI HAZARDS

Journal of Tsunami Society International

Volume 31

Number 1

2012

A STUDY OF THE EFFECT OF PERMEABILITY OF ROCKS IN TSUNAMI GENERATION AND PROPAGATION BY SEISMIC FAULTING USING LINEARIZED SHALLOW –WATER WAVE THEORY

PARUL SAXENA*

*POSTDOCTORAL FELLOW, DEPARTMENT OF MATHEMATICS
JAYPEE INSTITUTE OF INFORMATION TECHNOLOGY
A-10, SEC-62, NOIDA, INDIA.*

LOKENDRA KUMAR

*ASST. PROFESSOR, DEPARTMENT OF MATHEMATICS
JAYPEE INSTITUTE OF INFORMATION TECHNOLOGY, India
A-10, SEC-62, NOIDA, INDIA.*

ABSTRACT

The effect of permeability of rocks inside the ocean on Tsunami generation and Propagation is investigated. We study the nature of Tsunami build up and propagation using realistic curvilinear source models. The models are used to study the effect of permeability on tsunami amplitude amplification as a function on spreading velocity and rise time. Effect of permeability on Tsunami waveforms within the frame of the linearized shallow water wave theory for constant water depth are analyzed analytically using Transform methods. It is observed that in the region of highly permeable rocks the tsunami wave run is fast in comparison to low permeable rocks. The amplitude as a function of the propagated uplift length and width are analyzed. The cases of Tsunami-2011 (Japan), Tsunami-2006 (Srilanka), and Tsunami-2006 (Madras) have been demonstrated in the study.

Keywords: Tsunami Modeling, Water wave, permeability, Laplace and Fourier Transforms

Science of Tsunami Hazards, Vol. 31, No. 1, page 62 (2012)

1. INTRODUCTION

The generation of Tsunamis by a seafloor deformation is an example for the case where the waves are created by a given motion of the bottom. There are different natural phenomena that can lead to a Tsunami e.g. one can mention submarine slumps, volcanic explosions, earthquakes. (Tinti and Bortolucci 2000) investigated analytically the generation of tsunamis by submarine slides. They specialized the general solution of the 1D Cauchy linear problems for longer water waves to deal with rigid body to explore the characteristics of the generated waves. (Kervella et al. 2007) performed a comparison between three-dimensional linear and nonlinear tsunami generation models.

They observed very good agreement from the superposition of the wave profiles computed with the linear and fully nonlinear models. (Abou - Dina and Hassan 2006) have adopted a nonlinear theory and constructed a numerical model of tsunami generation and propagation which permits a variable bed displacement with an arbitrary water depth to be included in the model. The body motion in terms of Froude number, wave pattern, wave amplitude and wave energy have been studied by many authors (Takahasi and Hatori 1962), (Okada 1985), (Kajiura 1963), (Villeneuve 1993), (Nakamura 1953), (Tuck and Hwang 1972). All the previous studies mention above neglected the details of wave generation in fluid during the source time. One of the reasons is that it is commonly assumed that the source details are not important. (Trifunac and Todorovska 2002) mentioned the source parameters for submarine slides and earthquakes including source duration, displacement amplitude areas and volumes of selected past earthquakes that have or may have generated a tsunami.

(Dutykh and Dias 2007) generated waves theoretically by multiplying the static deformations caused by slip along a fault by various time laws: instantaneous, exponential, trigonometric and linear. (Harbitz et al. 2006) have investigated the characteristics of a tsunami generated by a submarine landslide. It is observed that tsunamis generated by submarine landslides have very large run up heights close to the surface area, but have more limited field effects than earthquake tsunamis. (Marghany and Hashim 2011) have studied 3D tsunami wave reconstruction using fuzzy B-spline. They used 2DDFT and presented a model to reconstruct of coastal successive tsunami waves of the test site in Srilanka.

In all the previous approaches, authors have not included the under ground water conditions, such as the nature of rocks inside the ocean. The most important feature of rocks which affect wave run up is permeability. Our approach is to study the effect of permeability in Tsunami generation and propagation. We have taken the model demonstrated by (Hassan et al. 2010) and considered that the ocean floor is porous. We have improved the model by taking the approach that the floor below the ocean is made up of rocks which are porous and differ in permeability. We studied the effect of permeability on tsunami generation and propagation. It is observed that under the ocean region where the permeability of rocks is high, tsunami waverunup is faster in comparison to those regions where the permeability of rocks is low. The cases of Tsunamis at Japan, Srilanka and Madras have been discussed.

2. MATHEMATICAL FORMULATION OF THE PROBLEM

Consider a three dimensional fluid domain Ω as shown in Figure 1. It is supposed to represent the ocean above the fault area. It is bounded above by the free surface of the ocean $z = \eta(x, y, t)$ and below by the porous ocean floor $z = -h(x, y) + \zeta(x, y, t)$, where $\eta(x, y, t)$ is the surface elevation, $h(x, y)$ is the water depth and $\zeta(x, y, t)$ is the sea floor displacement function. The domain is unbounded in the horizontal directions x and y , and can be written as $\Omega = \mathbb{R}^2 \times [-h(x, y) + \zeta(x, y, t), \eta(x, y, t)]$. For simplicity, $h(x, y)$ is assumed to be a constant. Before the earthquake, the fluid is assumed to be at rest, thus the free surface and the porous boundary are defined by $z = 0$ and $z = -h$, respectively.

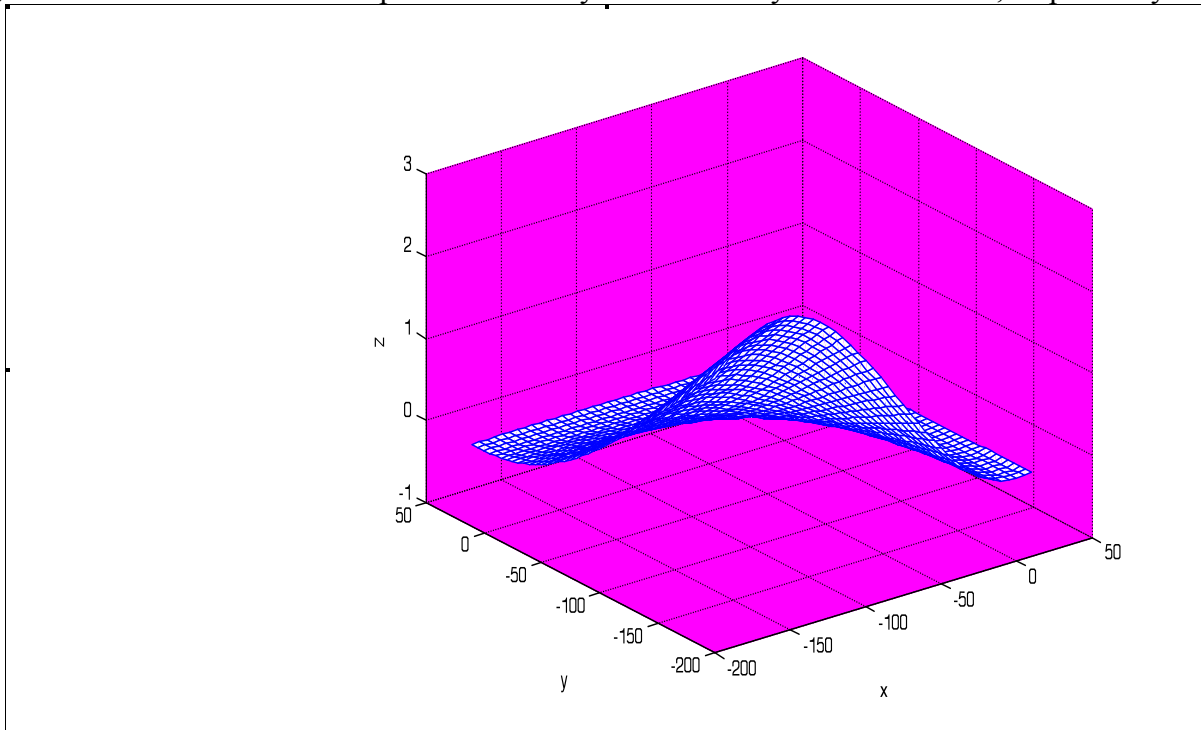


Figure 1. Definition of the fluid domain and coordinate system for a very rapid movement of the assumed source model.

Mathematically these conditions can be written in the form of initial conditions:

$$\eta(x, y, 0) = \zeta(x, y, 0) = 0.$$

At time $t > 0$ the bottom boundary moves in a prescribed manner which is given by $z = -h + \zeta(x, y, t)$.

The deformation of the sea bottom is assumed to have all the necessary properties needed to compute its Fourier transform in x, y and its Laplace transform in t . The resulting deformation of the free

surface $z = \eta(x, y, t)$ is to be found as part of the solution. It is assumed that the fluid is incompressible and the flow is irrotational. The former implies the existence of the velocity potential $\varphi(x, y, z, t)$ which fully describes the flow and the physical process. Since the ocean floor is made up of rocks which are porous, $\varphi(x, y, z, t)$ must satisfy the Brinkman equation of motion

$$\mu \nabla^2 \varphi(x, y, z, t) - \frac{\mu}{k} \varphi(x, y, z, t) = 0 \quad \text{where } (x, y, z) \in \Omega \quad (2.1)$$

The potential $\varphi(x, y, z, t)$ must satisfy the following kinematic and dynamic boundary conditions on the free surface and porous boundary, respectively:

$$\varphi_z = \eta_t + \varphi_x \eta_x + \varphi_y \eta_y \quad \text{on } z = \eta(x, y, t), \quad (2.2)$$

$$\varphi_z = \zeta_t + \varphi_x \zeta_x + \varphi_y \zeta_y \quad \text{on } z = -h + \zeta(x, y, t), \quad (2.3)$$

$$\varphi_t + \frac{1}{2} (\nabla \varphi)^2 + g\eta = 0 \quad \text{on } z = \eta(x, y, t) \quad (2.4)$$

where g is the acceleration due to gravity. As described above, the initial conditions are given by

$$\varphi(x, y, z, 0) = \eta(x, y, z, 0) = \zeta(x, y, z, 0) = 0. \quad (2.5)$$

In the case of tsunamis propagating on the surface of deep oceans, one can consider that Shallow-water theory is appropriate because the water depth (typically several kilometers) is much smaller than the wave length (typically several hundred kilometers), which is reasonable and usually true for most tsunamis triggered by submarine earthquakes, slumps and slides. Hence the problem can be linearized by neglecting the nonlinear terms in the boundary conditions (2-4) and if the boundary conditions are applied on the nondeformed instead of the deformed boundary surfaces (i.e. on $z = -h$ and $z = 0$ instead of $z = -h + \zeta(x, y, t)$ and $z = \eta(x, y, t)$). The linearized problem in dimensionless variables can be written as

$$(\nabla^2 - \sigma^2) \varphi(x, y, z, t) = 0 \quad \text{where } (x, y, z) \in \mathbb{R}^2 \times [-(h + h_s), 0], \quad (2.6)$$

Subjected to the following boundary conditions

$$\varphi_z = \eta_t \quad \text{on } z = 0 \quad (2.7)$$

$$\varphi_z = \zeta_t \quad \text{on } z = -h \quad (2.8)$$

$$\varphi_t + g\eta = 0 \quad \text{on } z = 0 \quad (2.9)$$

The linearized shallow water solution of the equation “(2.6)” can be obtained by Fourier-Laplace transform.

3. SOLUTION OF THE PROBLEM

Our interest is to study the effect of porous parameter in the resulting uplift of free surface elevation $\eta(x, y, t)$. An analytical analysis is examined to illustrate the generation and propagation of a tsunami with effect of permeability of rocks for a given bed profile $\zeta(x, y, t)$. Fourier-Laplace transform of the Brinkman equation has been used to study the effect of permeability of rocks in tsunami development. All our studies were taken into account constant depths for which the Laplace and Fast Fourier Transform (FFT) methods could be applied. The equations “(2.6)-(2.9)” can be solved by using the method of integral transforms. We apply the Fourier transform in (x, y) .

$$\mathfrak{F}[f] = \hat{f}(k_1, k_2) = \int_{R_2} f(x, y) e^{-i(k_1 x + k_2 y)} dx dy$$

with its inverse transform

$$\mathfrak{F}^{-1}[\hat{f}] = f(x, y) = \frac{1}{(2\pi)^2} \int_{R_2} \hat{f}(k_1, k_2) e^{i(k_1 x + k_2 y)} dk_1 dk_2$$

and the Laplace transform in time t ,

$$L[g] = G(s) = \int_0^{\infty} g(t) e^{-st} dt$$

For the combined Fourier and Laplace transforms, the following notation is introduced:

$$\mathfrak{F}(L(f(x, y, t))) = \bar{F}(k_1, k_2, s) = \int_{R_2} e^{-i(k_1 x + k_2 y)} dx dy \int_0^{\infty} f(x, y, t) e^{-st} dt$$

Combining “(2.7)” and “(2.9)” yields the single free-surface condition

$$\varphi_{tt}(x, y, 0, t) + g\varphi_z(x, y, 0, t) = 0. \quad (3.1)$$

After applying the transforms and using the property $\mathfrak{F}\left[\frac{d^n f}{dx^n}\right] = (ik)^n \bar{F}(k)$ and the initial conditions “(2.5)”, equations “(2.6)”, “(2.8)” and “(3.1)” become

$$\bar{\varphi}_{zz}(k_1, k_2, z, s) - (k_1^2 + k_2^2 + \sigma^2) \bar{\varphi}(k_1, k_2, z, s) = 0 \quad (3.2)$$

$$\bar{\varphi}_z(k_1, k_2, -h, s) = s\bar{\zeta}(k_1, k_2, s) \quad (3.3)$$

$$s^2 \bar{\varphi}(k_1, k_2, 0, s) + g\bar{\varphi}_z(k_1, k_2, 0, s) = 0 \quad (3.4)$$

The transformed free-surface elevation can be obtained from “(2.9)” as

$$\bar{\eta}(k_1, k_2, s) = -\frac{s}{g} \bar{\varphi}(k_1, k_2, 0, s) \quad (3.5)$$

The general solution of “(3.2)” will be given by

$$\bar{\varphi}(k_1, k_2, z, s) = A(k_1, k_2, s) \cosh(kz) + B(k_1, k_2, s) \sinh(kz) \quad (3.6)$$

where $k = \sqrt{k_1^2 + k_2^2 + \sigma^2}$. The functions $A(k_1, k_2, s)$ and $B(k_1, k_2, s)$ can be easily found from the boundary conditions “(3.3)” and “(3.4)”,

$$A(k_1, k_2, s) = \frac{g s \bar{\zeta}(k_1, k_2, s)}{\cosh(kh)[s^2 + g k \tanh(kh)]}$$

$$B(k_1, k_2, s) = \frac{s^3 \bar{\zeta}(k_1, k_2, s)}{k \cosh(kh)[s^2 + g k \tanh(kh)]}$$

Substituting the expressions for the functions A and B in the general solution “(3.6)” yields

$$\bar{\varphi}(k_1, k_2, z, s) = -\frac{g s \bar{\zeta}(k_1, k_2, s)}{\cosh(kh)[s^2 + \omega^2]} \left(\cosh(kh) - \frac{s^2}{gk} \sinh(kh) \right) \quad (3.7)$$

where $\omega = \sqrt{g k \tanh(kh)}$ is the circular frequency of wave motion. The free surface elevation $\bar{\eta}(k_1, k_2, s)$ can be obtained from “(3.5)” as

$$\bar{\eta}(k_1, k_2, s) = \frac{s^2 \bar{\zeta}(k_1, k_2, s)}{\cosh(kh)(s^2 + \omega^2)} \quad (3.8)$$

A solution for $\eta(x, y, t)$ can be evaluated for specified $\zeta(x, y, t)$ by computing approximately its transform $\bar{\zeta}(k_1, k_2, s)$ then substituting it into “(3.8)” and inverting $\bar{\eta}(k_1, k_2, s)$ to obtain $\bar{\eta}(k_1, k_2, t)$. We concern to evaluate $\eta(x, y, t)$ by transforming analytically the assumed source model then inverting the Laplace transform of $\bar{\eta}(k_1, k_2, s)$ to obtain $\bar{\eta}(k_1, k_2, t)$ which is further converted to $\eta(x, y, t)$ by using double inverse Fourier Transform.

The circular frequency ω describes the dispersion relation of tsunamis and implies phase velocity

$$c = \frac{\omega}{k} \text{ and group velocity } U = \frac{d\omega}{dk}. \text{ Hence } c = \sqrt{\frac{g \tanh(kh)}{k}} \text{ and } U = \frac{1}{2}c \left(1 + \frac{2kh}{\sinh(2kh)} \right).$$

Since, $k = \frac{2\pi}{\lambda}$, hence as $kh \rightarrow 0$, both $c \rightarrow \sqrt{gh}$ and $U \rightarrow \sqrt{gh}$, which implies that the Tsunami velocity $v_t = \sqrt{gh}$ for wavelengths λ long compared to the water depth h . The above linearized solution is known as the shallow water solution.

Now we consider a model for the sea floor displacement, namely a slowly curvilinear vertical faulting with rise time $0 \leq t \leq t_1$ and a variable single slip –fault, propagating unilaterally in the positive x -direction with time $t_1 \leq t \leq t^*$, both with finite velocity v . In the y -direction, the model propagate instantaneously. The set of physical parameters used in the problem are given in Table 1.

Table 1. Parameters used in the analytical solution of the problem.

| Parameters | Value for the uplift faulting |
|---|-------------------------------|
| Source width, W , km | 100 |
| Propagate length, L , km | 100 |
| Acceleration due to gravity, g , km/sec ² | 0.0098 |
| Water depth (uniform), h , km Tsunami velocity, $v_t = \sqrt{gh}$ | |
| Rupture velocity, v , km/sec, to obtain maximum surface amplitude | 0.14 |
| Duration of the source process, t , min | $t_1 = \frac{50}{v} = 5.95$ |

For the source model,

$$\zeta(x, y, t) = \begin{cases} \zeta_0 \frac{vt}{2L} (1 - \cos \frac{\pi}{50} x)(1 - \cos \frac{\pi}{100} (y+150)), & 0 \leq x \leq 100, \quad -150 \leq y \leq -50 \\ \zeta_0 \frac{vt}{2L} (1 - \cos \frac{\pi}{50} x), & 0 \leq x \leq 100, \quad -50 \leq y \leq 50 \\ \zeta_0 \frac{vt}{2L} (1 - \cos \frac{\pi}{50} x)(1 - \cos \frac{\pi}{100} (y-150)), & 0 \leq x \leq 100, \quad 50 \leq y \leq 150 \end{cases} \quad (3.9)$$

The free surface elevation takes initially the deformation of the bed shown in Figure 2 which remain at this elevation ζ_0 for $t \geq t_1$ and further propagate unilaterally in the positive x - direction with velocity v till it reaches t^* . Laplace and Fourier transform can now be applied to the bed motion described by (18) and we have

$$\mathfrak{S}(L(f(x, y, t))) = \bar{\zeta}(k_1, k_2, s) = \int_{\mathbb{R}_2} e^{-i(k_1 x + k_2 y)} dx dy \int_0^{\infty} \zeta(x, y, t) e^{-st} dt \quad (3.10)$$

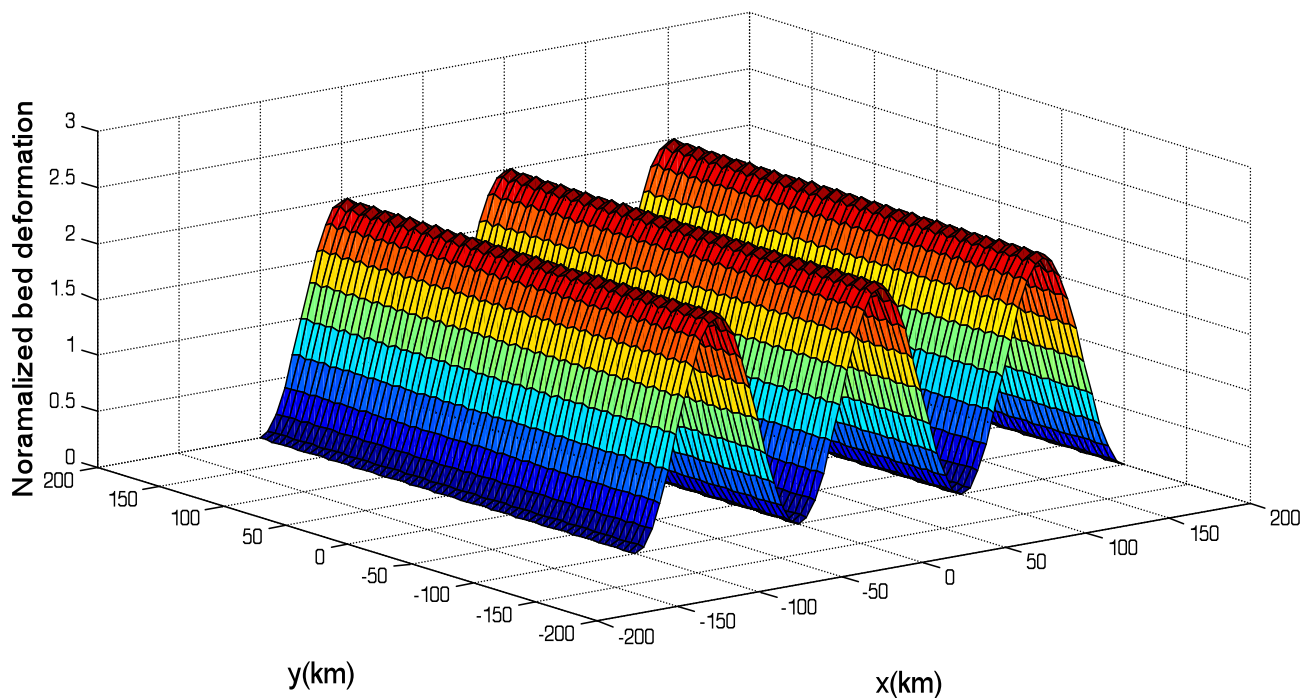


Figure 2. Three dimensional view of Normalized bed deformation representing by a slowly curvilinear uplift faulting at $t_1 = 50 / v$.

The limits of integration are apparent from “(3.9)”. Substituting the results of the integration “(3.10)” into “(3.8)”, yields

$$\bar{\eta}(k_1, k_2, s) = \frac{s}{\cosh(kh)(s^2 + \omega^2)} \zeta_0 \frac{v}{L} \frac{1}{2s} \left[\frac{(1 - e^{-i100k_1})}{ik_1} - \frac{e^{-i100k_1}}{1 - (\frac{50}{\pi}k_1)^2} [ik_1(\frac{50}{\pi})^2(e^{i100k_1} - 1)] \right] x$$

$$\left[\frac{(e^{i150k_2} - e^{i50k_2})}{ik_2} - \frac{1}{1 - (\frac{100}{\pi}k_2)^2} [ik_2(\frac{100}{\pi})^2(e^{i50k_2} + e^{i150k_2}) + \frac{4\sin(50k_2)}{k_2}] + \left[\frac{e^{-i50k_2} - e^{-i150k_2}}{ik_2} + \frac{1}{1 - (\frac{100}{\pi}k_2)^2} [ik_2(\frac{100}{\pi})^2(e^{i50k_2} + e^{i150k_2})] \right] \right] \quad (3.11)$$

The free surface elevation $\bar{\eta}(k_1, k_2, t)$ can be evaluated using inverse Laplace transform of $\bar{\eta}(k_1, k_2, s)$ as follows:

First, recall that $L^{-1}(\frac{s}{s^2 + \omega^2}) = \cos \omega t$ and $L^{-1}(\frac{1}{s}) = 1$, and the inverse of a product of transforms of two functions is their convolution in time.

Hence

$$\int_0^t \cos \tau \, d\tau = \frac{\sin \omega t}{\omega} \text{ and } \bar{\eta}(k_1, k_2, t) \text{ becomes}$$

$$\bar{\eta}(k_1, k_2, t) = \frac{\sin \omega t}{\omega \cosh(kh)} \zeta_0 \frac{v}{2L} \left[\frac{(1 - e^{-i100k_1})}{ik_1} - \frac{e^{-i100k_1}}{1 - (\frac{50}{\pi}k_1)^2} [ik_1(\frac{50}{\pi})^2(e^{i100k_1} - 1)] \right] x$$

$$\left[\frac{(e^{i150k_2} - e^{i50k_2})}{ik_2} - \frac{1}{1 - (\frac{100}{\pi}k_2)^2} [ik_2(\frac{100}{\pi})^2(e^{i50k_2} + e^{i150k_2}) + \frac{4\sin(50k_2)}{k_2}] + \left[\frac{e^{-i50k_2} - e^{-i150k_2}}{ik_2} + \frac{1}{1 - (\frac{100}{\pi}k_2)^2} [ik_2(\frac{100}{\pi})^2(e^{i50k_2} + e^{i150k_2})] \right] \right] \quad (3.12)$$

Finally, $\eta(x, y, t)$ is evaluated using the double inverse Fourier transform of $\bar{\eta}(k_1, k_2, t)$

$$\eta(x, y, t) = \frac{1}{(2\pi)^2} \int_{-\infty}^{\infty} e^{ik_2 y} \left[\int_{-\infty}^{\infty} e^{ik_1 x} \bar{\eta}(k_1, k_2, t) dk_1 \right] dk_2 \quad (3.13)$$

This inversion is computed by using the FFT. The inverse FFT is a fast algorithm for efficient implementation of the Inverse Discrete Fourier Transform (IDFT) given by

$$f(m, n) = \frac{1}{MN} \sum_{p=0}^{M-1} \sum_{q=0}^{N-1} F(p, q) e^{i\left(\frac{2\pi}{M}\right)pm} e^{i\left(\frac{2\pi}{N}\right)qn}, p = 0, 1, \dots, M-1; q = 0, 1, \dots, N-1$$

where $f(m, n)$ is the resulted function of the two spatial variables m and n , corresponding x and y , from the frequency domain function $F(p, q)$ with frequency variables p and q , corresponding k_1 and k_2 . This version is done efficiently by using the Matlab FFT algorithm.

The water wave motion in the near and far field by considering a model based on curvilinear uplifting has been discussed. The effect of permeability of rocks on the Tsunami wave generation and propagation have been investigated using the model.

4. DISCUSSION AND CONCLUSIONS

We are interested in investigating the effect of permeability of rocks near the ocean floor on the wave propagation in Tsunami based on the considered model. For $v/v_t = 0.8$, we have investigated the effect of porous ocean floor using Darcy number σ . Fig. 3, Fig. 4 and Fig. 5 represent the wave propagation during Tsunamis with $\sigma = 5.0$, $\sigma = 10.0$ and $\sigma = 15.0$ respectively. In these figures three dimensional and two dimensional waves run up have been shown with the effect of σ . The closer view of wave run-up has been shown in Fig. 6, Fig. 7 and Fig. 8 for $\sigma = 5.0$, $\sigma = 10.0$ and $\sigma = 15.0$ respectively.

The case of Tsunami in Japan -2011 has been discussed by taking the approach of this model. It is observed that the amplitude of Tsunami wave run is extremely high in this case as can be seen in Fig. 10. (Vithanage 2008) has demonstrated the wave run during Tsunami in Srilanka -2006 and we modified it by taking the effect of permeability of ocean floor and shown in Fig. 11. (Kumar et al. 2008) have studied Tsunami hazard along Chennai coast and demonstrated Inundation map for it. We have used that map to explain the effect of permeability of ocean floor based on considered model. In Fig. 12, the affected regions of India near Chennai-2004 by Tsunami have been shown. We have investigated that the Tsunami wave propagation depend on the vulnerability of the region which is based on the permeability of rocks and sediments inside the coastal zone. It is observed that in the region of less vulnerability the amplitude of Tsunami wave run was low in comparison to high vulnerable region.

It is observed that near the source the wave has large amplitude and as the permeability of the ocean floor increases the amplitude of wave increases. The present analysis suggests that some abnormally large tsunamis could be explained in part by considering the effect of permeability of rocks near the ocean floor. Our results should help to improve Tsunami forecasts and warnings based on recoverable seismic data.

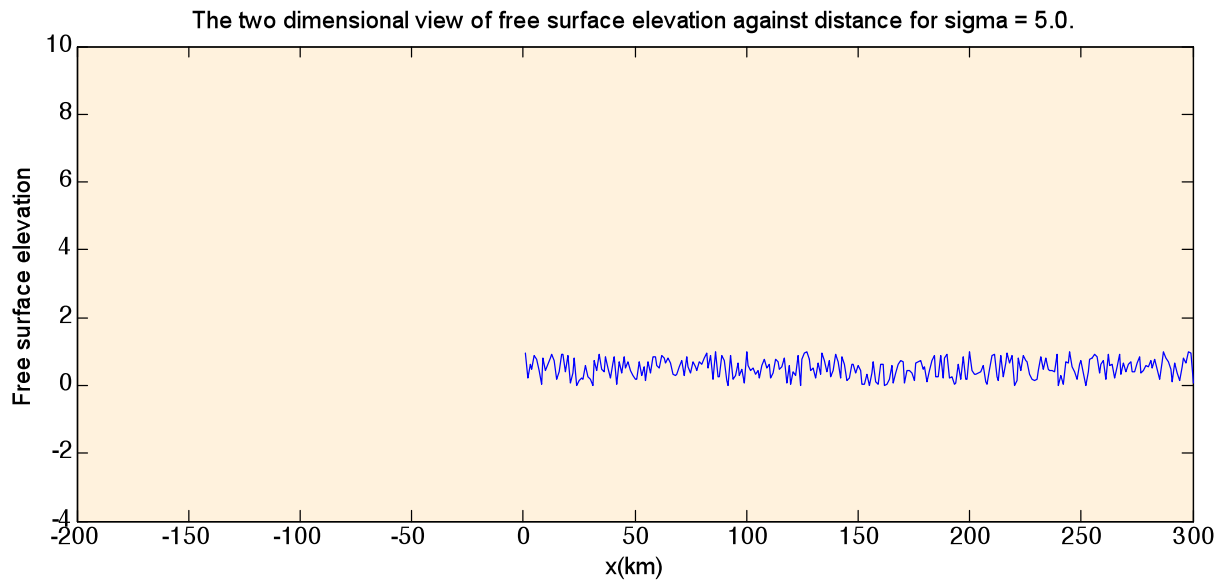
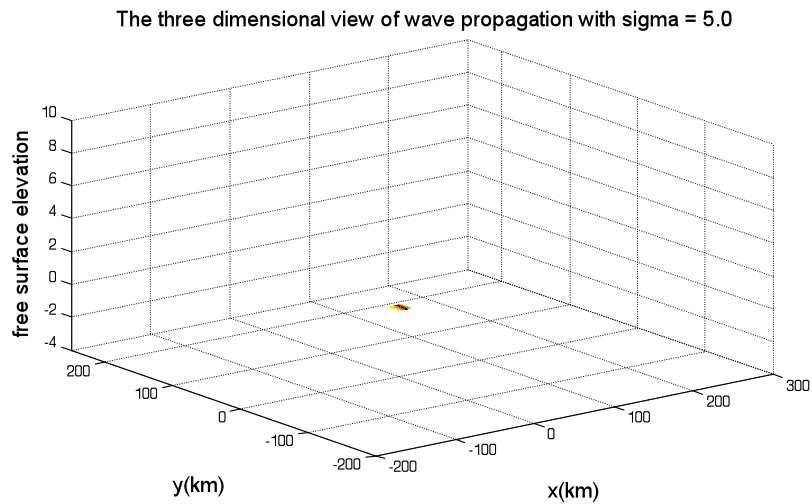
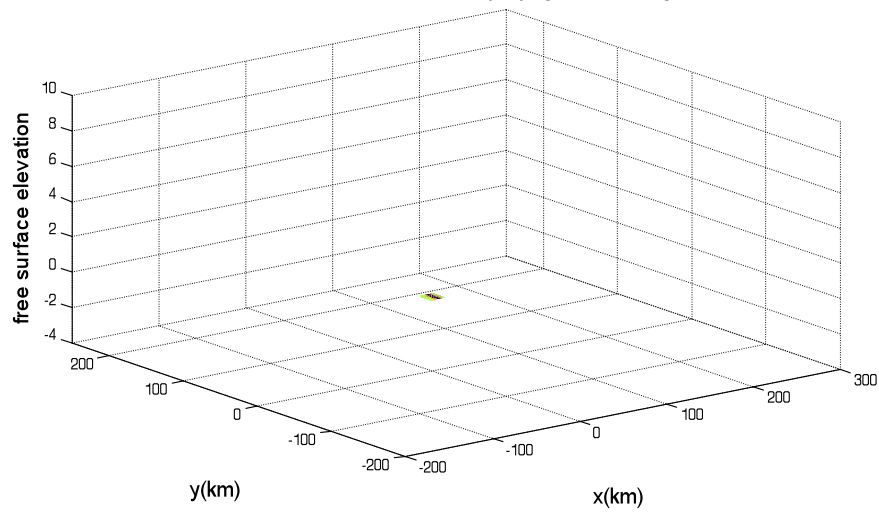


Figure 3. Dimensionless free surface deformation $\eta(x, y, t^*) / \zeta_0$ for $v/v_t < 1$ at $h = 2$ km, $L = 150$ km, $W = 100$ km, $v_t = 0.14$ km/sec and $t^* = 50/v$ sec.

The three dimensional view of wave propagation with sigma = 10.0



The two dimensional view of free surface elevation against distance for sigma = 10.0

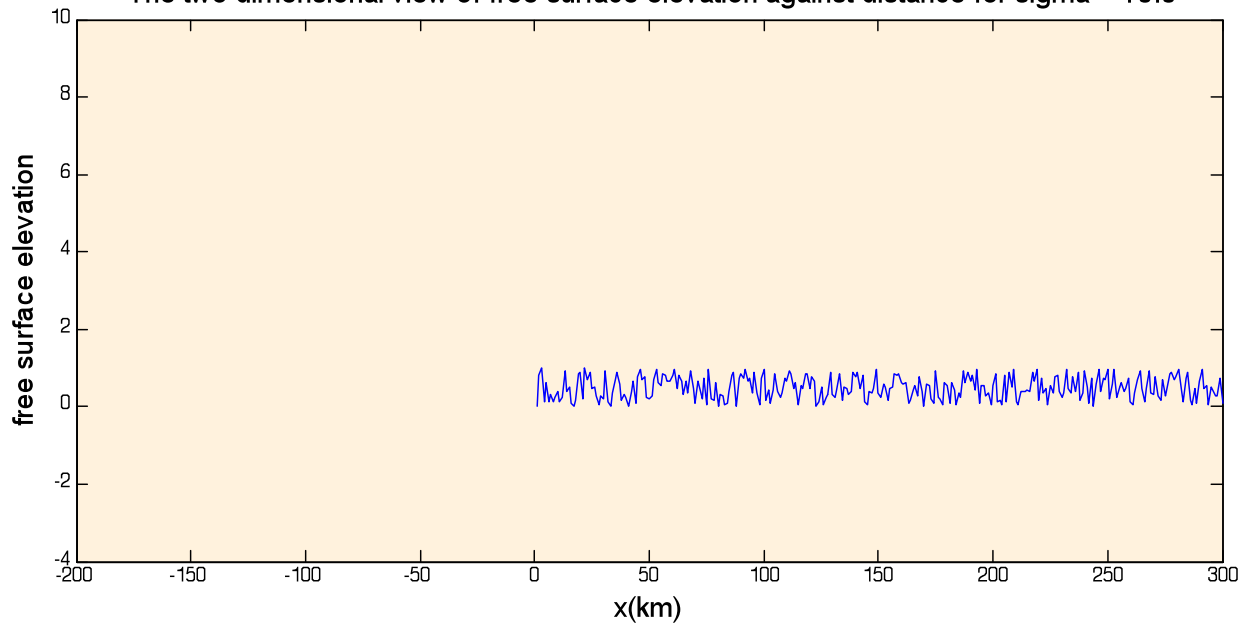


Figure 4. Dimensionless free surface deformation $\eta(x, y, t^*)/\zeta_0$ for $v/v_t < 1$ at $h = 2$ km, $L = 150$ km, $W = 100$ km, $v_t = 0.14$ km/sec and $t^* = 50/v$ sec.

Science of Tsunami Hazards, Vol. 31, No. 1, page 73 (2012)

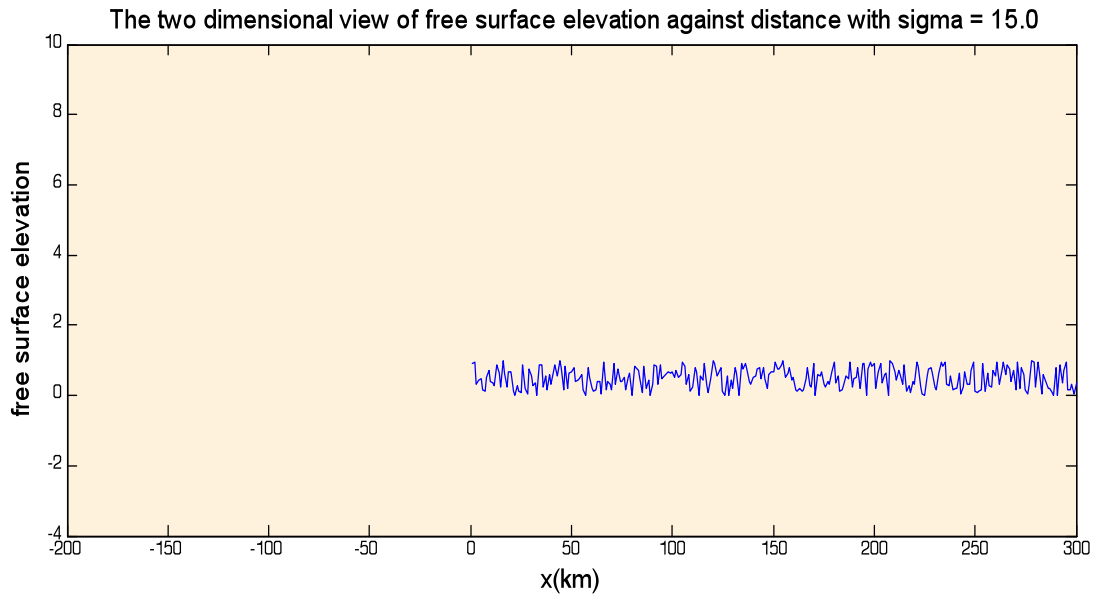


Figure 5. Dimensionless free surface deformation $\eta(x, y, t^*)/\zeta_0$ for $v/v_t < 1$ at $h = 2$ km, $L = 150$ km, $W = 100$ km, $v_t = 0.14$ km/sec and $t^* = 50/v$ sec.

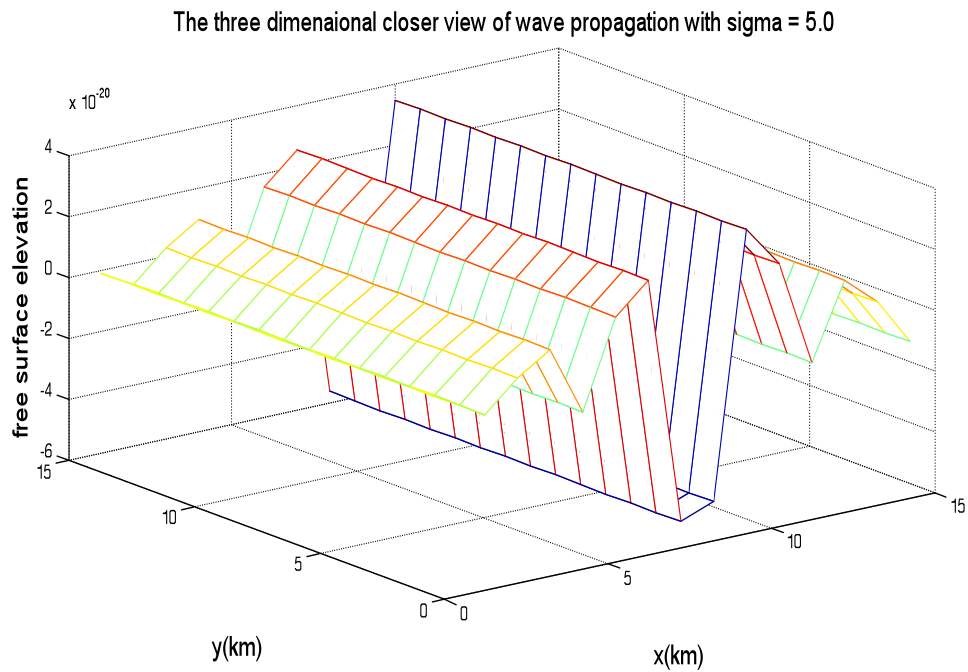


Figure 6. Dimensionless closer view of wave propagation for $h = 2$ km, $L = 150$ km, $W = 100$ km, $v_t = 0.14$ km/sec and $t^* = 50/v$ sec.

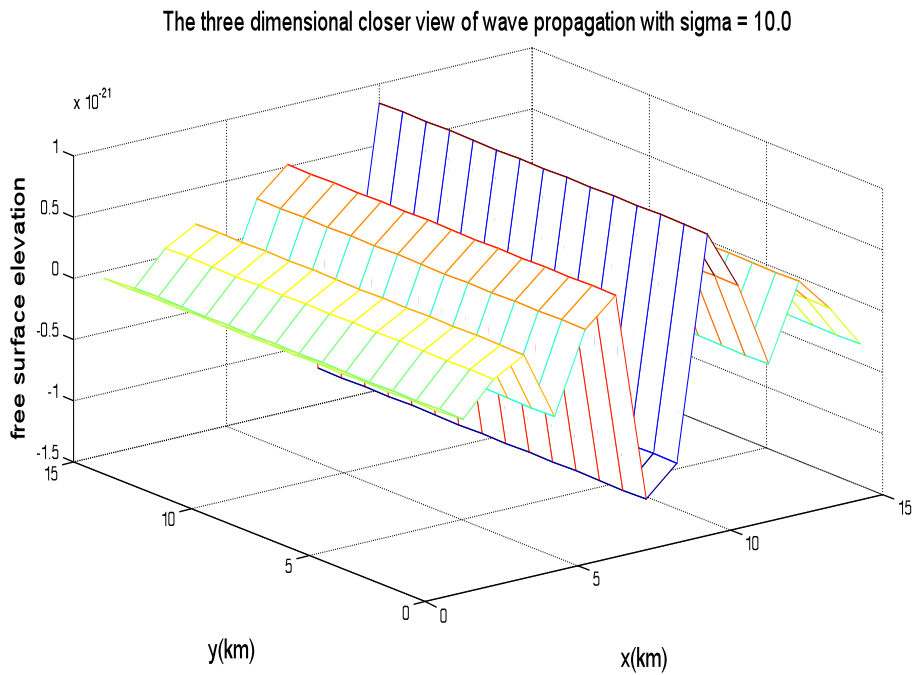


Figure 7. Dimensionless closer view of wave propagation for $h = 2$ km, $L = 150$ km, $W = 100$ km, $v_t = 0.14$ km/sec and $t^* = 50/v$ sec.

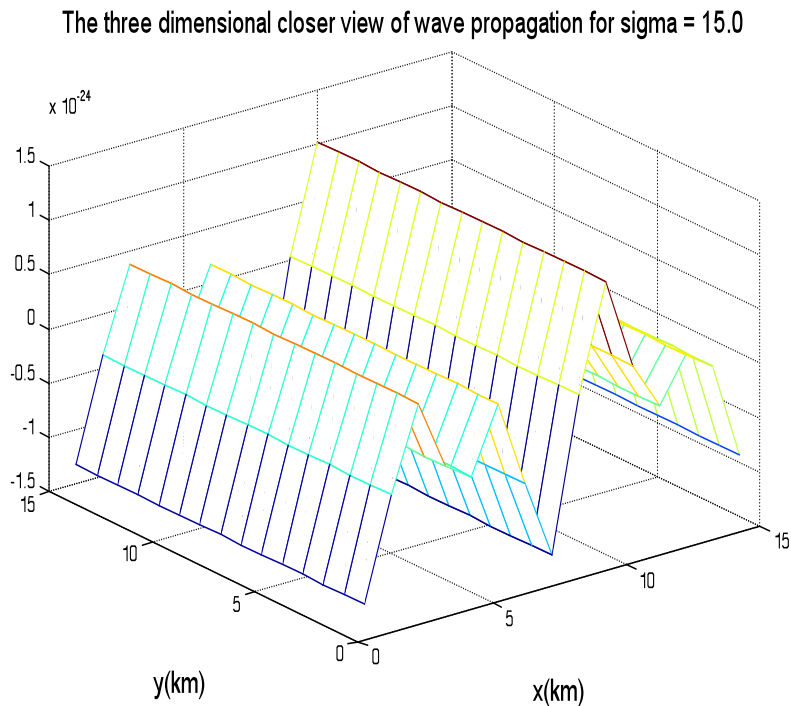


Figure 8. Dimensionless closer view of wave propagation for $h = 2$ km, $L = 150$ km, $W = 100$ km, $v_t = 0.14$ km/sec and $t^* = 50/v$ sec.



Figure 9. The affected regions of Japan in Tsunami -2011.

Science of Tsunami Hazards, Vol. 31, No. 1, page 76 (2012)

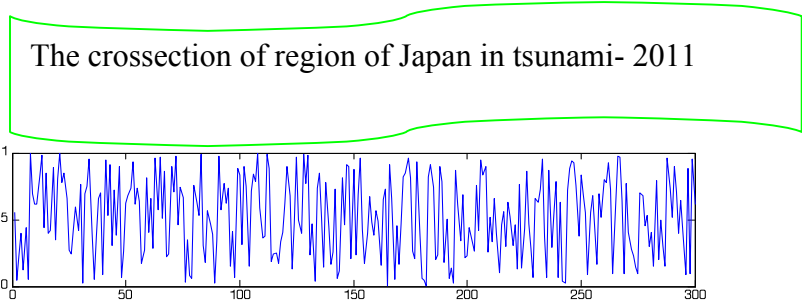
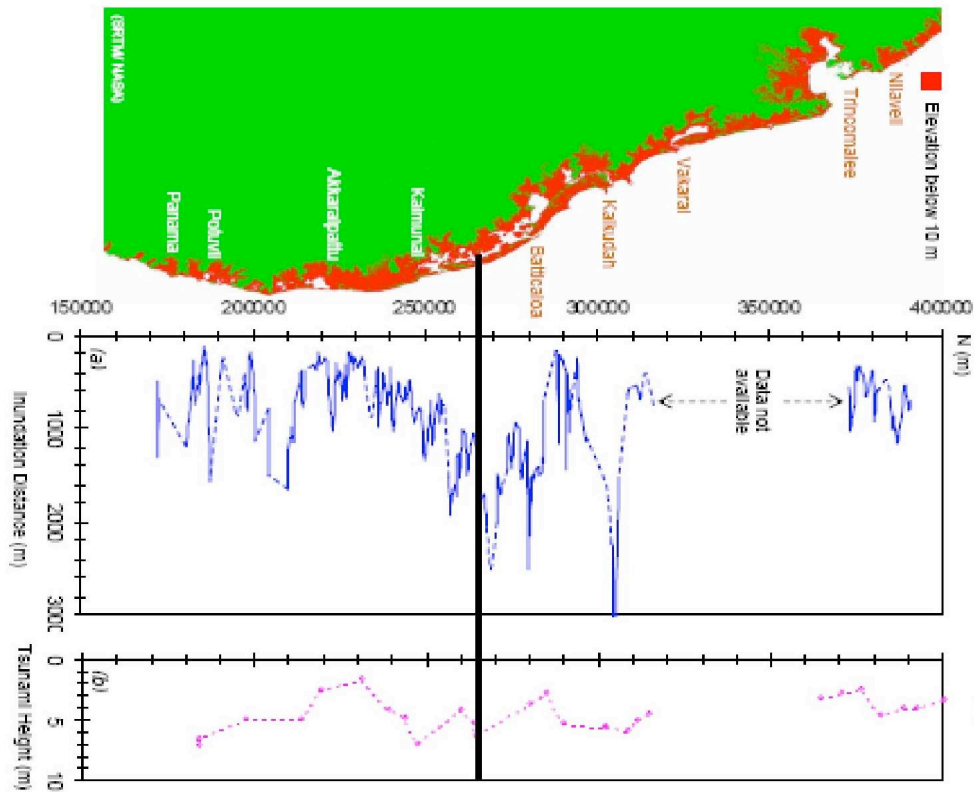


Figure 10. The wave propagation in Tsunami at Japan in 2011 based on the considered model.



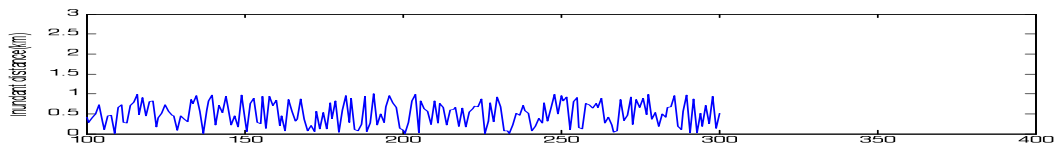


Figure 11. The wave propagation with the effect of permeability of rocks in Tsunami at Srilanka in 2006

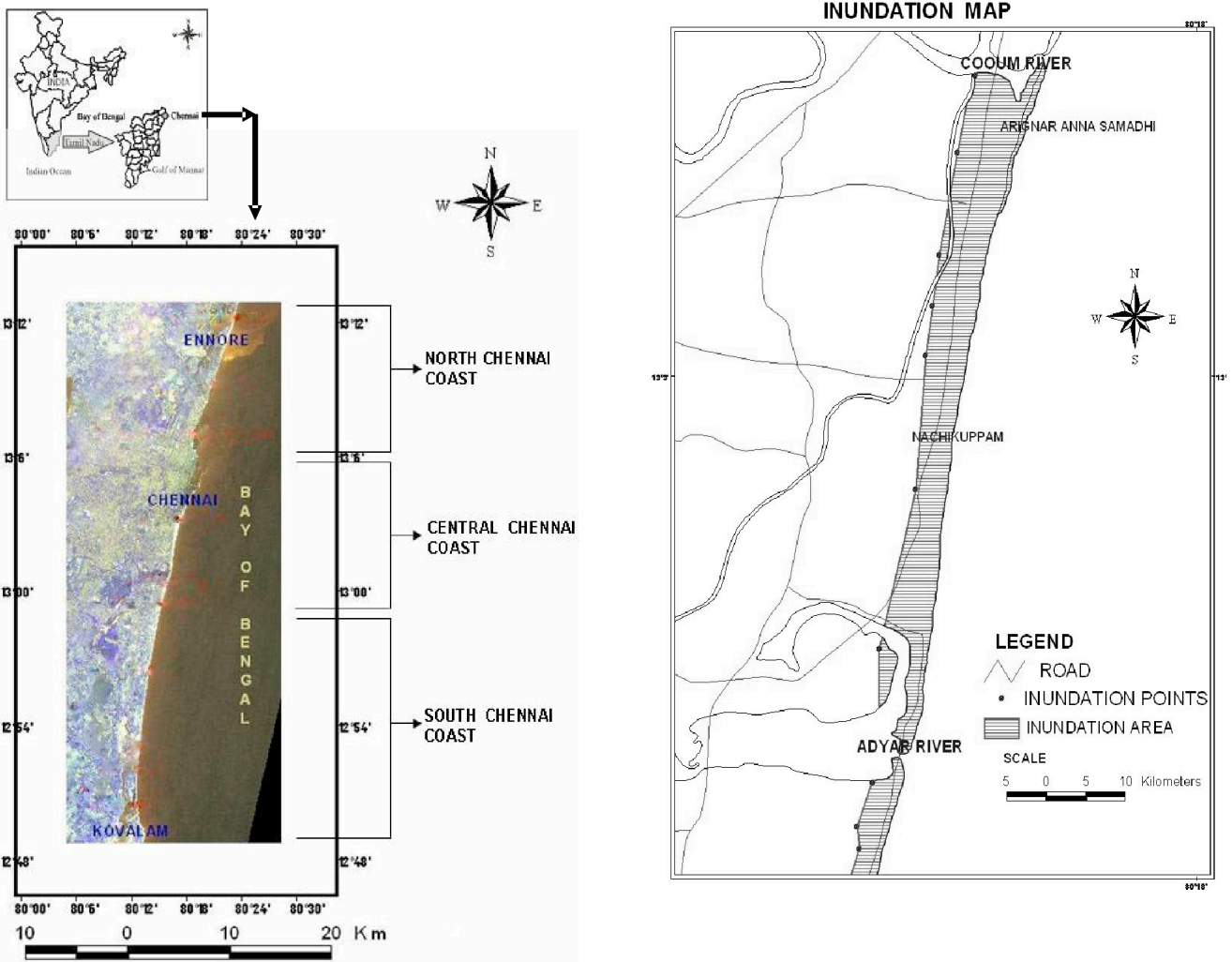


Figure 12. The affected regions of Chennai in Tsunami - 2004.

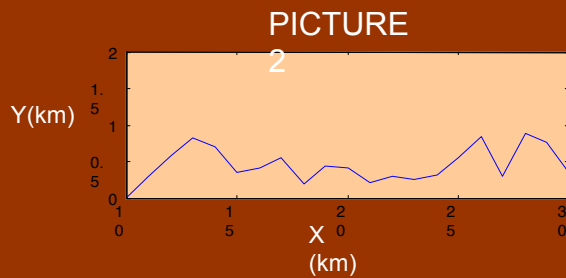
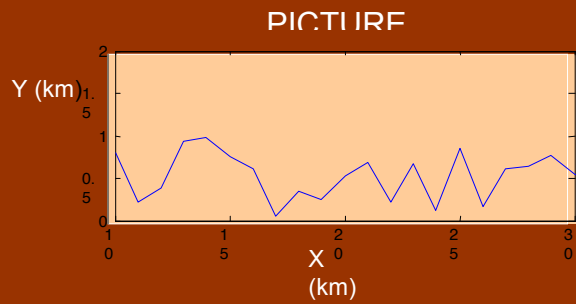


Figure 13. Picture 1 presents the wave propagation in less vulnerable region and Picture 2 presents it in high vulnerable region of Tsunami in Chennai 2004.

ACKNOWLEDGMENTS

The author, Parul Saxena is thankful to the Department of Atomic Energy, Government of India for the financial assistance and to the Department of Mathematics, Jaypee Institute of Information & Technology for research facilities during this work.

Science of Tsunami Hazards, Vol. 31, No. 1, page 79 (2012)

REFERENCES

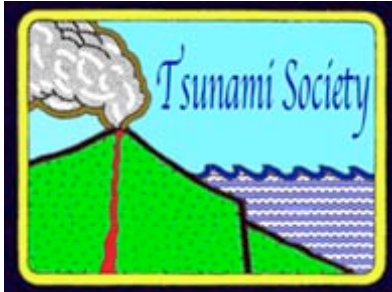
- Abou-Dina, M. S. and Hassan, F. M. [2006] “Generation and propagation of nonlinear tsunamis in shallow water by a moving topography,” *Applied Mathematics and computation*, **177** (2), 785-806.
- Dutykh, D. and Dias, F. [2007] “Water waves generated by a moving bottom,” *In K. Anjan, Ed. Tsunami and Nonlinear waves, Springer-Verlag, Berlin*, 63-94.
- Harbitz, C. B., Lovholt, F. G. Pedersen and Massan, D. G. [2006] “Mechanism of tsunami generation by submarine landslides: a short review,” *Norwegian Journal of Geology*, **86**, 255-264.
- Hassan, H. S., Ramadan, K. T. and Hanna, S. N. [2010] “Modeling of Tsunami generation and propagation by a spreading curvilinear seismic faulting in linearized shallow-water wave theory,” *Journal of Applied Mathematics*, **1**, 44-64.
- Kajiura, K. [1963] “Leading wave of a tsunami,” *Bulletin Earthquake Research Institute, Tokyo University*, **41**, 535-571
- Kervella, Y. Dutykh, D. and Dias, F. [2007] “Comparison between three-dimensional linear and nonlinear Tsunami Generation models,” *Theoretical and computational Fluid Dynamics*, **21**(4), 245-269.
- Kumar, C. S., Krishnamurthy, P. A., Usha, T. and Pari, Y. [2008] “Inundation mapping – a study based on December 004 Tsunami Hazard along Chennai coast, Southeast India,” **8**, 617-625.
- Marghany, M. and Hashim, M. [2011] “3D tsunami wave reconstruction from quickbird data by using fuzzy B-spline,” *International Journal of the Physical Sciences*, **6**(13), 3111-3115.
- Nakamura, K. [1953] “On the waves caused by the deformation of the bottom of the sea I.,” *Science Reports of the Tohoku University*, **5**, 1953, 167-176.
- Okada, Y. [1985] “Surface deformation due to shear and tensile faults in a half space,” *Bulletin of the seismological society of America*, **75**(4), 1135-1154.
- Takahasi, R. and Hatori, T. [1962] “A model experiment on the Tsunami generation from a bottom deformation area of elliptic shape,” *Bulletin Earthquake Research Institute, Tokyo University*, **40**, 235-248.
- Tinti, S. and Bortolucci, E. [2000] “Analytical investigation on Tsunamis generated by submarine slides,” *Annaali di Geofisica*, **43**(3), 519-536.

Trifunac, M. D. and Todorovska, M. I. [2002] “Generation of Tsunamis by a slowly spreading uplift of the sea floor,” *Soil Dynamics and Earthquake Engineering*, 22(2), 143-155.

Tuck, E. O. and Hwang, L. S. [1972] “Long wave generation on a sloping beach,” *Journal of Fluid Mechanics*, **51**(3), 449-461.

Villeneuve, M. [1993] “Nonlinear, Dispersive, Shallow-water waves Developed by a moving bed,” *Journal of Hydraulic Research*, **31**(2), 249-266.

Vithanage, M. S. [2008] “Effect of Tsunamis on coastal aquifers: Field study and tank experiments,” *PhD thesis, University of Copenhagen*.



SCIENCE OF TSUNAMI HAZARDS

Journal of Tsunami Society International

Volume 31

Number 1

2012

ALGERIA'S VULNERABILITY TO TSUNAMIS FROM NEAR-FIELD SEISMIC SOURCES

L. Amir^{1*}, A. Cisternas², J. -L. Vignerresse³, W. Dudley⁴, B. Mc Adoo⁵

¹*USTHB-FSTGAT, BP 32, Bab Ezzouar, Algiers, Algeria*

²*Universidad De Chile, Santiago, Chile*

³*UHP, UMR 7566, Vandoeuvre les Nancy, France*

⁴*University of Hawaii, Hilo, HI, 96720, USA*

⁵*Vassar College, Box 735, Poughkeepsie, NY, 12601 USA*

**Corresponding author, E-mail: lou.amir@gmail.com*

ABSTRACT

Evaluation of the effects of tsunami damage relative to earthquake damage may help to identify critical coastal zone structures and exposed populations for near field tsunami risk. In this work, we propose to define the ratio between tsunami intensity and earthquake intensity as a measure of near field tsunami vulnerability for coastal communities. This parameter is estimated for 13 tsunami events reported in North Algeria from the 14th century to present. Although the results show that there are no tsunamis that are unusually large for the size of the earthquake that generated them, coastal communities remain at risk from these periodic hazards.

We also use tsunami modelling and published information to estimate maximum inundation in Northern Algeria. Then, we generate a flooding map, which reveals the communities, buildings and infrastructure that are exposed to the tsunami hazard. This map shows that the majority of the people in Algiers and Oran live above 5 meters in elevation, and are hence not exposed to the hazard. Despite this, the coastline remains vulnerable to tsunami as earthquakes can damage poorly constructed buildings and other infrastructure, weakening it prior to the arrival of the tsunami. To increase resilience in the coastal zone, tsunami and earthquake awareness, education and preparedness must become a priority in the context of regional early warning programs.

Science of Tsunami Hazards, Vol. 31, No. 1, page 82 (2012)

1. INTRODUCTION

In the southwest Mediterranean, the convergence between Eurasia and Africa plates (< 1 cm/yr) results in earthquakes that reach magnitude up to 7.5. Northern Algeria is located at the boundary between the two tectonic plates. This region is subjected to moderate to large earthquakes (Fig. 1).

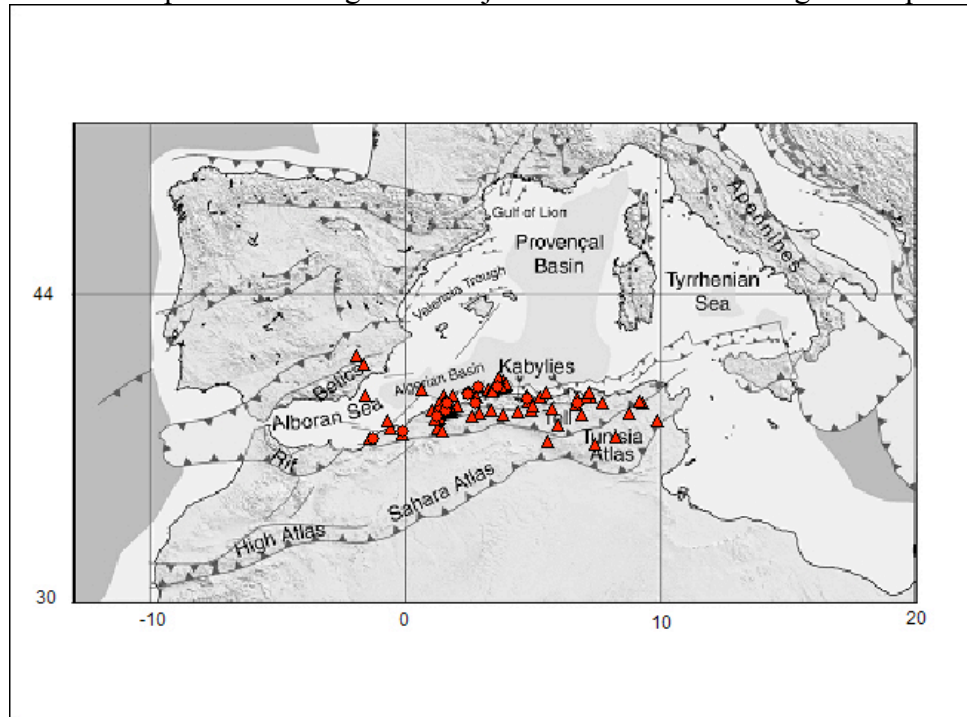


Fig. 1: Seismicity of Northern Algeria and Tectonic sketch of the West Mediterranean (modified from Mauffret, 2007). Earthquakes data are from the USGS-NEIC database (from 1980 to present). Red circles represent magnitude above 5.5 and red stars represent magnitude between 4.5 and 5.5.

Tsunami events have also been reported in historical documents. The first reported tsunami dates from the 14th century in Algiers (Ambraseys and Vogt 1988). The most recent tsunami was triggered in 2003 after a magnitude Mw 6.8 earthquake offshore of Boumerdes, 40 km east of Algiers (NEIC-USGS) (death toll: 2300) (Alasset et al., 2006). Advance and retreat of the sea were also observed in the coastal village of Dellys (50 km east of Algiers) (see pictures in Fig. 2– Anonymous).

Since the Sumatra-Andaman tsunami of December 2004 (death toll: 250000), the UNESCO - IOC (International Oceanographic Commission) has been working on a Tsunami Warning Program for the Mediterranean Sea. The Mediterranean is narrow and the disaster vulnerability (earthquake and tsunami) differs considerably from one country to the next. The rapid pace of urbanism in coastal cities that face near field tsunamis raises a question about the efficiency of a tsunami warning system and the consequences of possible false alarms.

The rapid growth of coastal infrastructure, individual houses and other features associated with urbanism and economic development raises the issue of tsunami and earthquake preparedness related to socio-economic challenges and vulnerability of urban centers to natural hazards. The Algerian

Mediterranean coast extends by 1200 km from the east to the west. The number of the total inhabitant of the country is 35 million. As of 2010, more than 60% of the Algerian population was considered as urban. Indeed, the urban population increased by 114% from 1960 to 2008 (Univ. of Sherbrooke, data from the World Bank, <http://perspective.usherbrooke.ca>). Expansion of the coastal city of Algiers (capital of Algeria) has increased every year and the agglomeration limits and the demography evolve in such a way that today, the number of inhabitants living in Algiers is more than 4 million (source: Algerian National Statistic Organism, 2010). With 1.8 million of inhabitants, Oran (Western part of coastal Algeria) is considered as the second largest urban agglomeration in the country.



Fig. 2: Pictures of the 2003 tsunami waves in Dellys (50 km east of Algiers) after a 6.8 magnitude earthquake in Zemmouri (40 km east of Algiers) (Pictures from Anonymous)

Because of the possibility of having destructive earthquakes, and induced tsunamis, this work is aimed at contributing to the development of a tsunami warning system policy for Northern Algeria. In this paper, we first review potential tsunami sources for the central and the western part of Northern Algeria from published information. Then, we present the tools and the methods we use to quantify and qualify the potential flooding limits from exposure to the near field tsunami hazard for the coastal Communities of Algiers and Oran. Finally, we discuss on the disaster risk policy in Northern Algeria in the context of the development of the Mediterranean Tsunami Warning System.

2. SEISMICITY, TSUNAMI SOURCES AND TSUNAMI OCCURRENCE IN ALGIERS AND ORAN REGIONS (NORTH ALGERIA)

Algeria is located at the boundary between the African and the Eurasian tectonic plates. Seismicity is shallow (5 to 20 km in depth) and concentrated in the northern part of the country. It is related to the Tell Atlas fold belt and associated active reverse faulting (Meghraoui, 1988; Aoudia et al., 2000). Seismicity is moderate to large and earthquakes magnitude reach 7 to 7.5. Those are mostly associated with thrust faulting mechanisms (Bezzeghoud et al., 1995, Deverchere et al., 2005).

The compressive motion between Africa and Eurasia has led to the formation of Quaternary faulted folds structures. In the central part of Algeria, the Sahel Anticline is related to the Sahel Blind Fault and in the western part of the country, the Murdjajo anticline is also associated with reverse faulting (Fig. 3) (Harbi et al., 2007, Bouhadad, 2001). Those geological structures are oriented NE – SW with strikes varying from 40 to 70°N. Offshore geophysical surveys conducted along the Algerian margin revealed numerous thrust faults dipping to the southeast direction (Domzig et al., 2006; Mauffret, 2007). Further, numerous canyons and headwall scarps were also identified and mapped offshore the Algerian margin by Dan et al. (2009).

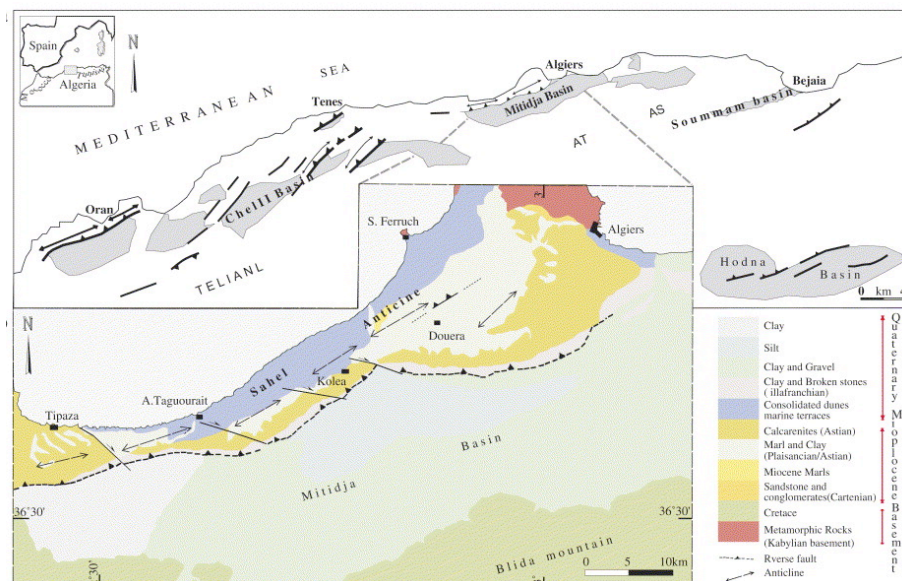


Fig. 3: The Sahel and the Murdjajo structures near Algiers and Oran (From Harbi et al., 2007).

2.1 The Central Algeria (Algiers Region)

The first reported earthquake that hit Algiers occurred on 3 January 1365. This earthquake destroyed the city ($I_0=X$, EMS-98). The earthquake triggered a tsunami that flooded the lower part of the city of Algiers (Ambraseys and Vogt, 1988). In 1716, the Mitidja region was hit by another devastating earthquake ($I_0=IX-X$, EMS scale) (death toll: 20,000 people). The city of Algiers was seriously impacted and the town of Blida was nearly destroyed (Ambraseys and Vogt, 1988). Landslides triggered by the event were also reported by Ambraseys and Vogt (1988). Harbi et al. (2007) also report the description of a tsunami event in 1773 in Algiers.

In September 1954, the Orleansville earthquake ($M=6.7$) generated turbidity currents. As explained by Heezen and Ewing (1955) "Breaks in submarine cables following the 1954 earthquake are believed to have been caused by the motion of a mass of sediments detached from the continental slope by the shock and transformed into a strong turbidity current which swept out across the Balearic abyssal plain, rather than directly by earthquake movements".

The 1980 El Asnam ($M_s=7.2$) seismic event was disastrous (2600 deaths). The earthquake focal mechanism indicates reverse faulting (Cisternas et al., 1982). Again, the breaking of phone cables is attributed to turbidity currents generated by the strong seismic shock (Robrini, 1985).

The 1989 Chenoua-Tipaza earthquake ($M_s=5.9$, USGS) also highlighted the existence of a blind thrust fault system (Meghraoui, 1990). The epicentre was located offshore and noted to have induced a disturbance in the sea. Meghraoui (1990) reported landslides observed on the coast road and on the southern side of the Mount Chenoua. A sea wave was observed by sailors and the sea dropped by more than a meter in Tipaza harbour (Meghraoui, 1990).

The most recent tsunami was triggered by a magnitude M_w 6.8 earthquake offshore of Zemmouri, 50 km east of Algiers (Alasset et al., 2006). Disturbance of the sea is reported for the Algerian coast and run ups of 1 to 2 meters in height were recorded on the Balearic tide gauges.

2.2 The Western Algeria (the Oranie Region)

In Western Algeria, the Oranie region is also a seismogenic area with destructive earthquakes reported in historical and recent documents. In 1790, the city of Oran was severely affected by an earthquake of intensity X (MSK intensity scale) (Marinas Lopez and Salord, 1990; Bouhadad, 2001; Bouhadad and Laouami, 2002). This earthquake was felt elsewhere in North Africa and Spain as well, and a tsunami was triggered (Marinas Lopez and Salord, 1990).

The Murdjajo fold-faults are considered as potential tectonically active structures prone to cause devastating earthquakes and tsunamis (Bouhadad, 2001). Mauffret (2007) pointed out the Arzew escarpment may result from a NE-SW left lateral fault with a reverse component. We suggest it also could have played a role during the 1790 Alboran tsunami (Amir and Cisternas, 2010). Since 1790, a seismic gap has been observed in the region with no event with magnitude larger than 5.5 (Ayadi et al., 2002).

3. MATERIAL AND METHODS

3.1 Mapping the Tsunami Flooding Hazard from modelling and published information

3.1.1 Tsunami Modelling

Tsunami models for earthquakes with moment magnitude of 7.5 are computed at the entrance of Algiers and Oran harbours. Those models are considered as a worst-case scenario.

Tsunami generation and propagation are calculated from the non-linear shallow water code SWAN (Mader, 2004). This program solves the 2D non-linear Eulerian equations within a finite difference scheme. The Mediterranean topography was obtained from the NOAA ETOPO two minute and one minute grids for the Algiers and the Oranie - Alboran case studies respectively (Amante and Eakins, 2009) (source: <http://www.ngdc.noaa.gov>). The two-minute grid was from 0 to 10 E and 35 N to 44 N. The one-minute grid was from 6 W to 2 E and 34 N to 42 N. For both tests, the time step calculation is 5 minutes.

The tsunami sources were computed from the Okada equations (Okada, 1992). The earthquake source parameters and the co-seismic rupture geometry were deduced from the seismic moment and the conventional seismological relationships of Kanamori (1975) and Wells and Coppersmith (1994). Table 1 lists the tsunami source input parameters for sea bottom calculation offshore for Algiers and Oran.

Table 1: Tsunami source input parameters for sea bottom calculation in Algiers and Oran.

| | Algiers | Oran |
|-----------------------------------|-------------|---------------|
| Magnitude Mw | 7.5 | 7.5 |
| Epicenter coordinates (°) | 3.1E, 36.8N | 0.58W, 35.76N |
| Focal depth (km) | 07 | 05 |
| Strike and Dip (°) | 55N, 40SE | 65N, 45SE |
| Length * Width (fault plane) (km) | 73.3*29.2 | 73.3 * 29.2 |
| Slip (m) | 3.45 | 3.45 |

3.1.2 Map Flooding for the Algiers and the Oran Bays.

The study of historical earthquakes and tsunamis is critical in order to evaluate the flooding hazard along the coast. In this work, potential tsunami flooding is estimated from numerical modelling tasks and published information (articles, photographs, public database).

Geo-browsers are useful tools that help common users and authorities to visualise, analyse and combine geo hazard information with coastal geography and urbanism as well. Using the path features from the Google Earth program, we created KML and KMZ files to represent inundation limits.

3.2 Preliminary Vulnerability Assessment:

Vulnerability to tsunamis and earthquakes can be defined as the impact of a catastrophic event in terms of damage (houses and infrastructures destroyed, casualties, and homeless people). Near-field tsunami regions are exposed to a combination of earthquakes and tsunami damage. To assess the vulnerability to near field tsunamis, this preliminary study focuses on the ratio of tsunami to earthquake intensity (TI / EI).

Damage from earthquakes (buildings, infrastructures and people) is identified using macroseismic intensities. In particular, the EMS intensity scale involves 12 grades that describe the effects of vulnerability to earthquakes.

Several scales have been defined to quantify tsunamis. Papadopoulos and Imamura (2001) proposed a new 12-grade intensity scale. This scale can be considered as an analog to the seismic intensity scale. Consequently, it helps to compare the damage of a near-field tsunami relative to the damage generated by earthquakes.

Scientists classically quantify the tsunami intensity from the Imamura or the Soloviev Intensity scale. In this study, we use available data from the NOAA-NGDC database (source: <http://www.ngdc.noaa.gov>). Here, the Soloviev and Go (1974) tsunami intensity values are converted into the Papadopoulos – Imamura (2001) intensities. Then, the vulnerability index is calculated from the ratio TI / EI.

4. RESULTS

4.1 Tsunami models for Algiers and Oran region

Near field tsunamis triggered in Northern Algeria produce water waves that reach the coast in less than 5 minutes. Figure 4 illustrates the topography and the offshore tectonic context for Western and North Central Algeria.

Figures 5a and 5b shows an earthquake located at 3.1E, 36.8N, e.g. nearby harbour of Algiers (distance to the shoreline is less than 05 km) which generate tsunami waves that are soon trapped in the Bay of Algiers for more than 15 minutes.

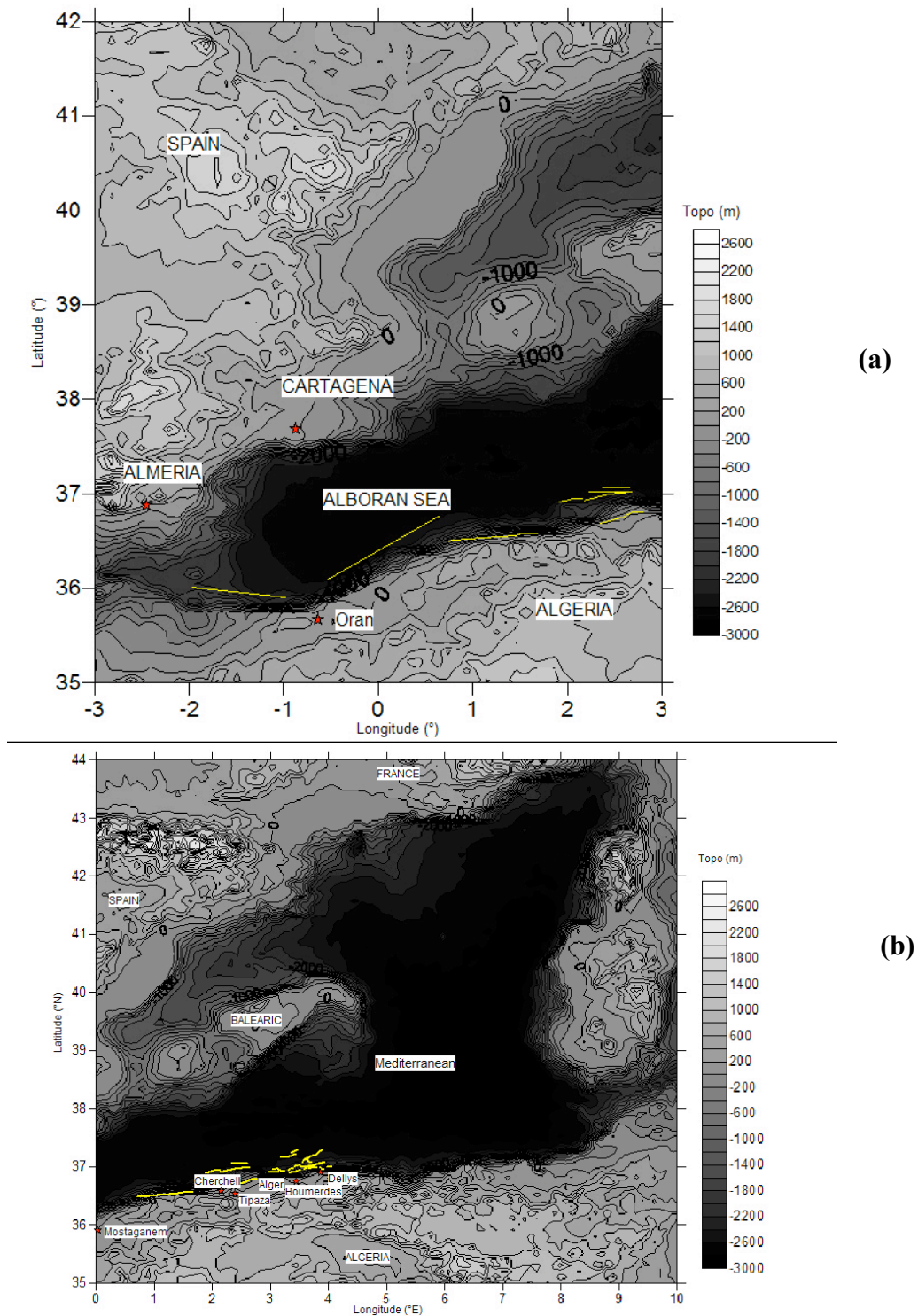


Fig. 4: Bathymetry (ETOPO database) for (a) North Western and (b) Central Algeria. Selected Offshore faults (yellow lines) are from (Domzig et al., 2006; Dan et al; 2009; Mauffret, 2007).

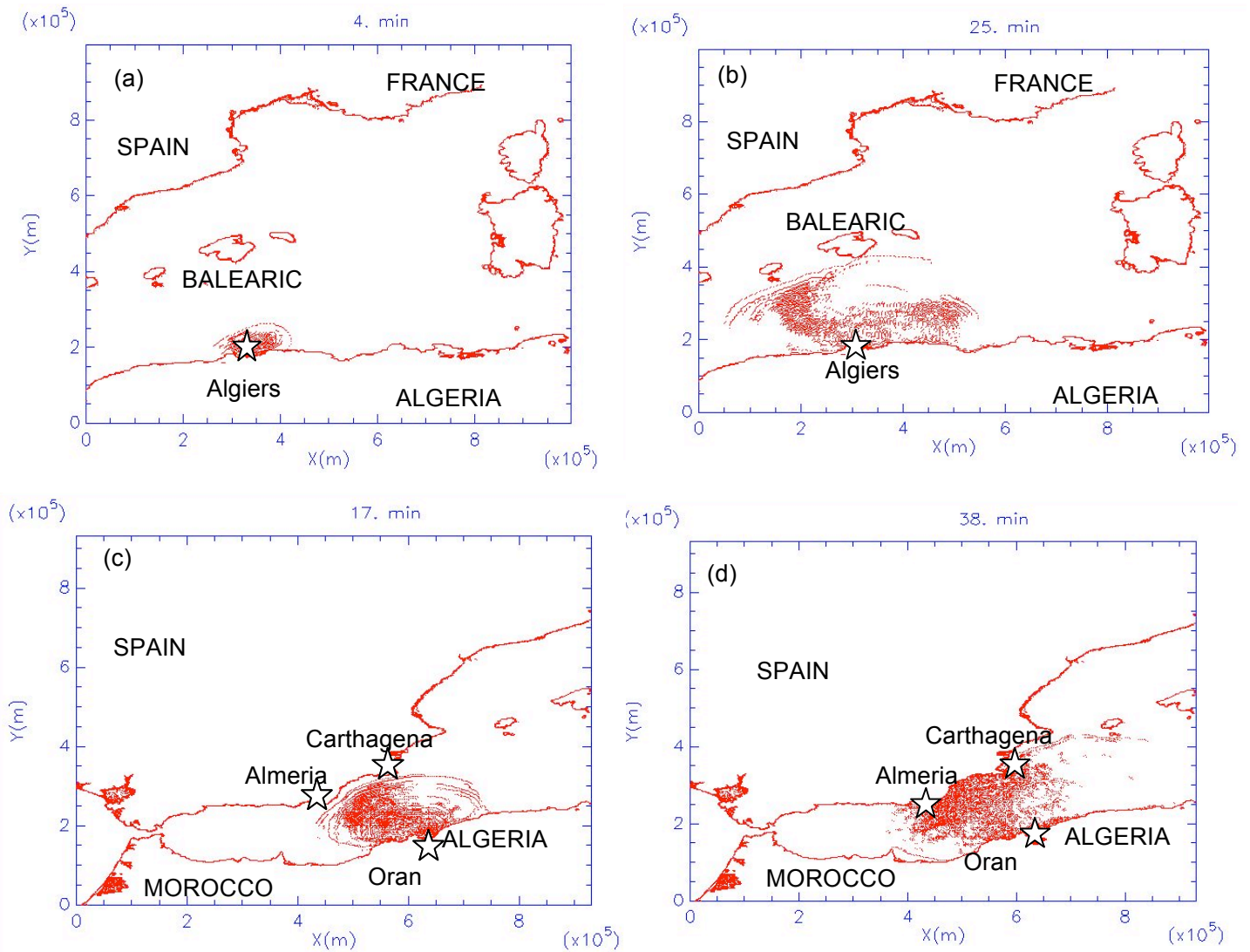


Fig. 5: Tsunami wave propagation for (a & b) Algiers and (c & d) Oran-Alboran study cases. The times are 4 and 25 min for Algiers and 17 and 38 min for Oran. The grid size is 2 min for Algiers and 1 min for Oran-Alboran.

The choice of this epicentre corresponds to the hypothetical earthquake location for the 1365 Algiers event (Ambraseys and Vogt, 1988; internal publication of the CRAAG). Likewise a seismogenic source located at 35.76N, 0.58W (distance to the shoreline less than 03 km), in the entrance of Oran harbour (Figures 5c and 5d) is used. This epicentre was adjusted according to published information on the 1790 Oran event (Bouhadad, 2001; Bouhadad and Laouami, 2002) and the description of tsunami waves observed in Oran, Carthage and Almeria and reported by Marinas and Salord (1990). Hence, advance and retreat of the sea can be observed along the Algerian coast for a period of 15 minutes. For the Algiers case study, the maximum wave heights computed in Algiers are no greater than 2 meters in Algiers (Figure 6a). For Oran, water wave heights are less than 3 meters (Figure 6c). In both cases, sources located in Northern Algeria results in tsunami waves that reach the Spanish and French coasts in less than 20 minutes.

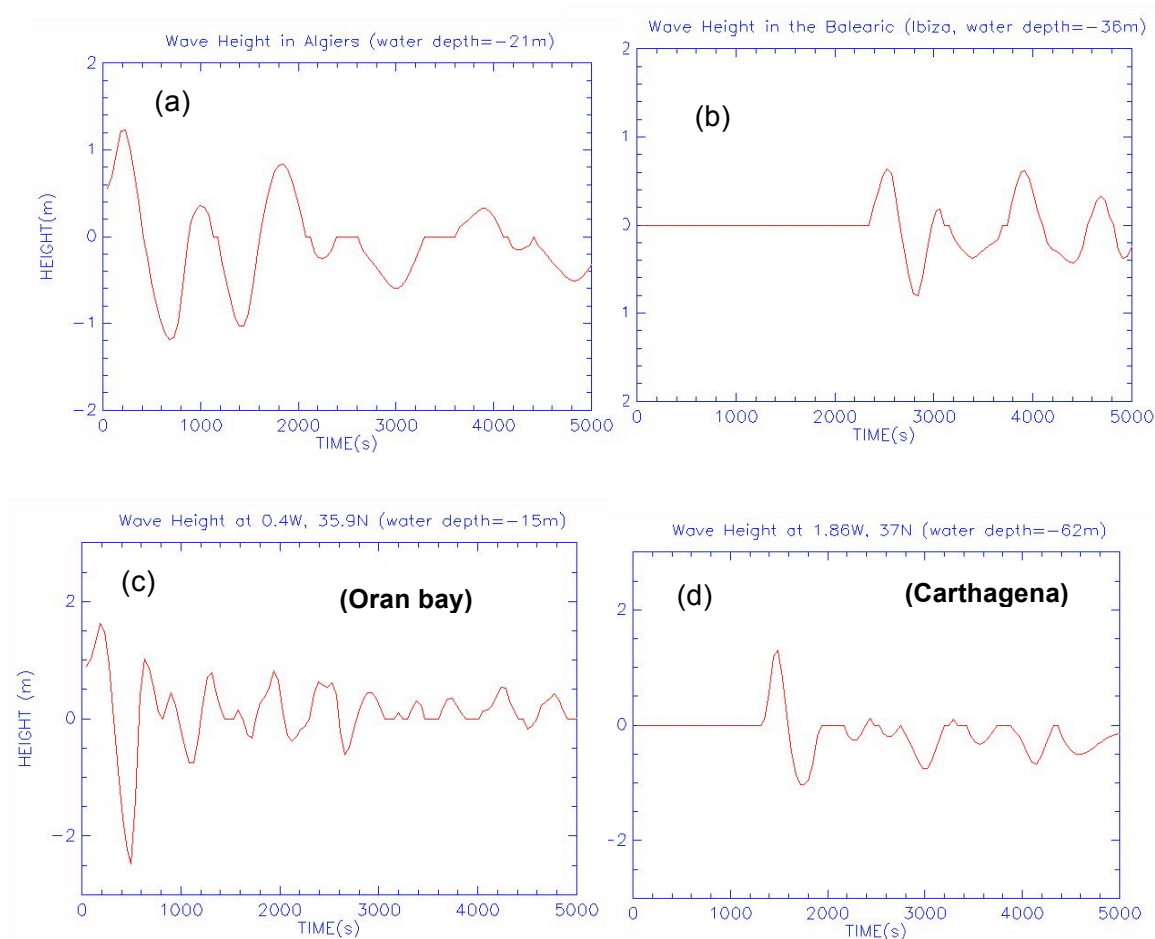


Fig. 6: Wave profiles computed with the SWAN code for (a & b) Algiers and (c & d) Oran – Alboran study cases.

4.2 Flood hazard map for Algiers and Oran urban coastal cities and Tsunami vulnerability in Northern Algeria

Modelling results showed maximum tsunami waves heights range from 0.5 to 3 meters. In 2009, Maouche et al. found tsunami evidence (boulders) from field investigations west and east of Algiers. They estimated those boulders could be associated with waves up to 5 meters in height. Studying the 1856 Jijel tsunamis (East of Algeria) from a compilation of historical documents, Roger and Hebert (2008) and Yelles et al. (2009) reported the flooding of the coast in Jijel and Bejaia after the destructive earthquake. Tsunami waves of 2-3 meters in height in Jijel and 5 meters in Bejaia are mentioned in historical documents. As a result, a maximum potential inundation height of 5 meters is reported on the flooding hazard map (Fig. 7 & 8).



Fig. 7: Flooding map for Algiers region (with Google earth). The red contour line is 5 meters in elevation. Credit for Pictures: L. Amir



Fig. 8: Flooding map for Oran region (Google Earth); the contour line is 5 meters in elevation (in red) – Photographs showing the Oran harbor and the Oran city are downloaded from Google Earth

Figure 9 presents the vulnerability index calculated for 13 tsunami events recorded for tsunami sources in Northern Algeria from the 14th century to present day. Results show that the ratio TI (Tsunami Intensity) / EI (Earthquake Intensity) is lower than 1. As a result, tsunami damage is minor relative to the corresponding earthquake damage.

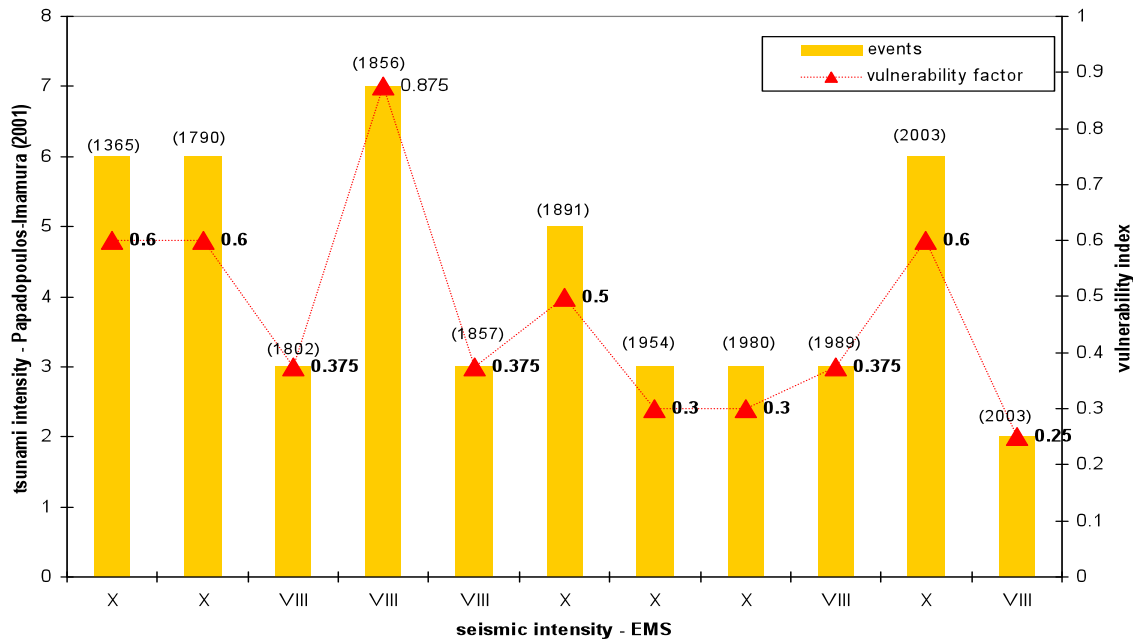


Fig. 9: Vulnerability index for Northern Algeria. (Year of the tsunami event between the brackets).

The inhabitants of Algiers and Oran mostly live in areas above 5 meters elevation. However, rapid urban growth raises the issues of (1) new coastal infrastructure and (2) commercial/residential buildings where the ground floor is dedicated to commercial activities. Nevertheless, the distance between the shoreline and safe places during a tsunami event is not respected. As a result in event of a tsunamigenic earthquake with a magnitude greater than 6, the lack of tsunami education and preparedness could result in panic reactions from the inhabitants.

5. DISCUSSION

5.1 Tsunami inundation limits from the modelling approach

In this work, computed values for tsunami flood hazard mapping are deduced from simulations using the shallow water SWAN code (Mader, 2004). Although the offshore wave heights calculated are less than 3 meters in height, near shore bathymetry and topography often amplifies wave heights, therefore tsunami risk should be considered for the northern part of the country. The effects of the friction and bottom slope angle were not considered in the present modelling. Limits of Tsunami inundation modelling from the SWAN code are discussed in Mader (2004).

The development and evaluation of a realistic friction model is an important remaining tsunami flooding problem. The tsunami wave period and amplitude, bottom slope angle and friction are parameters that affect the assessment of tsunami coastal inundation. Discrepancies between run-ups calculated from the Eulerian and the Navier-Stokes equations are also pointed out by Mader (2004). Numerical simulations need to be refined by using a higher resolution bathymetric grid and considering a slide component associated with the earthquake event.

6.2 Disaster preparedness in Northern Algeria

The timing between the earthquake occurrence along the fault and the first waves that reach the Algerian coast is less than 5 minutes. Fortunately, the tsunami vulnerability index shows that earthquakes in Algeria do not produce unusually large tsunamis. Regardless, coastal city urbanism, traffic, coastal erosion, and bay morphology all raise challenges that vulnerable populations have to face and necessitate improvements in disaster preparedness (construction, creation and location of evacuation routes, coastal infrastructure and effective emergency management policies). Early warning, education, and preparedness programs for earthquake and tsunami in near field tsunami regions marked by rapid urban growth helps reduce vulnerability and increase resilience.

One of the main issues for tsunami preparedness relates to earthquake-resistant coastal infrastructure and individual coastal buildings and residences. The question is what to do when a devastating earthquake occurs, site effects are such that buildings are damaged or collapse, and tsunami waves reach the coast so that people have to evacuate to higher elevations. The present study shows that a flooding hazard exists, but thanks to the topographic features of Algiers and Oran, most inhabitants live in sites above 5 meters. Consequently, the problem focuses on coastal urban growth and tsunami and earthquake preparedness, and mitigation zoning measures for threatened inhabited coastal areas.

Disaster preparedness, prevention and education are the object of a series of laws adopted by the Algerian national parliament on the 25th of December 2004, the day before the Asian tsunami disaster (law n°04-20, *source*: Ministry of the Territory Management). The content of these laws is concerned with emergency planning (ORSEC plans, the requirement for insurance for natural disasters; rules to reduce vulnerability, alert systems, education and information to be integrated within schools...). Nevertheless, the application of the procedures is still a challenge. Working on a project related to a Housing Earthquake Safety Initiative for a group of countries (Algeria, Indonesia, Nepal and Peru), the UNCRD (United Nations Centre for Regional Development) pointed to socio-economic problems in implementing disaster management in Algeria.

Although building codes exist since the 1954 Orleansville earthquake (1981: RPA/99; 2003: RPA/99 version 2003), 60% of the total buildings are not built to these codes (EERI, 2003). After the disaster resulting from the 2003 Mw 6.8 earthquake in Boumerdes, a building survey from the ERI (Earthquake Research Institute) revealed 42% to 59% of the individual homes were built without a legal permit (EERI, 2003).

In that context, only public information explaining tsunamis, their origin and occurrence, the range and probable limits of flooding, and vulnerability can help to create an effective warning tsunami program for near field tsunamis in Algeria.

6. CONCLUSIONS

Destructive earthquakes and tsunamis events have occurred and been reported in North Algeria in the past and up to the present day. The Sahel Anticline System (nearby of Algiers, central part of Algeria) and the Murdjajo Anticline system (Oran, west of Algeria) are associated with reverse faulting. Both geological structures have the potential to generate a disaster (earthquake and associated tsunami) along the Algerian coast.

Hence, the implementation of local tsunami warning centers for near field tsunamis regions could help to minimize loss of life and damage for urbanised coastal cities. However, an education and information campaign could reduce tsunami vulnerability and increase resilience.

Acknowledgements

The first author thanks Dr. C.L. Mader from Mader Consulting & Co (HI, USA) for his kind assistance with the SWAN code and constructive remarks. M.S. Boughacha and H. Benhallou from the University of Houari Boumediene (Algiers, Algeria) are gratefully acknowledged for the constructive discussions related to tsunamis in Oran region and disaster management for urban cities in Algeria.

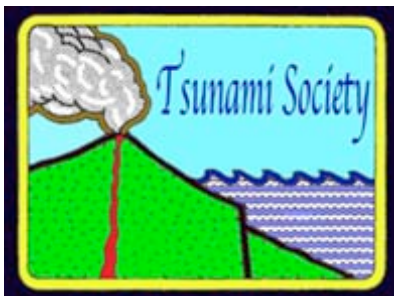
REFERENCES

- Amante, C. and B. W. Eakins** (2009), ETOPO1 1 Arc-Minute Global Relief Model: Procedures, Data Sources and Analysis, *NOAA Technical Memorandum NESDIS NGDC-24*, 19 pp.
- Alasset, P.-J., Hebert, H., Maouche, S., Calbini, V. and Meghraoui, M.** (2006), The Tsunami induced by the 2003 Zemmouri earthquake (Mw=6.9): modelling and results, *Geophysical Journal International*, 166, 213-226.
- Ambraseys, N. N. and Vogt, J.** (1988), Material for the investigation of the seismicity of the region of Algiers, *European Earthq. Eng.*, 3, 16-29.
- Amir, L. and Cisternas, A.** (2010), Appraisal of the 1790 Alboran Tsunami source in the west Mediterranean sea as inferred from numerical modelling: Insights for the tsunami hazard in Algeria, Proceedings of the 9th U.S. National and 10th Canadian Conference on Earthquake Engineering- Compte rendu de la 9^{ieme} Conference Nationale Americaine et 10^{ieme} conference Canadienne de Genie Parasismique, July 25-29, 2010, Toronto, Canada.
- Audia, A., Vaccari, F., Suhadolc, P. and Meghraoui, M.** (2000), Seismogenic Potential and Earthquake Hazard Assessment in the Tell Atlas of Algeria, *JOSE*, 4, 79-88.
- Ayadi, A., Oussadou-Ayadi, F. Bourouis, S. and Benhallou, H.** (2002), Seismotectonics and seismic quietness of the Oranie region (Western Algeria) : The Mascara earthquake of August 18th 1994, Mw=5.7, Ms=6.0, *Journal of Seismology*, 6, 13-23

- Bezzeghoud, M., Dimitrov, D., Ruegg, J.C. and Lammali, K.**, (1995), Faulting mechanism of the El Asnam (Algeria) 1954 and 1980 earthquakes from modelling of vertical movements, *Tectonophysics*, 249, 249-266.
- Bouhadad, Y.** (2001), The Murdjajo, Western Algeria, fault-related fold: Implications for seismic hazard, *Journal of Seismology*, 5, 541-558.
- Bouhadad, Y. and Laouami, N.** (2002), Earthquake Hazard Assessment in the Oran region (Northwest Algeria), *Natural Hazards*, 26, 227-243.
- Cisternas, A., Dorel, J. and Gaulon, R.** (1982), Models of the complex source of the El Asnam earthquake, *Bulletin of the Seismological Society of America*, 72, 6A, 2245-2266
- Deverchere, J., K. Yelles, A. Domzig, B. Mercier de Lepinay, J.P. Bouillin, V. Gaulier, R. Bracene, E. Calais, B. Savoye, A. Kherroubi, P. Le Roy, H. Pauc, and G. Dan** (2005), Active thrust faulting offshore Boumerdes, Algeria, and its relation to the 2003 Mw 6.9 earthquake, *Geophys. Res. Lett.*, 32, doi:10.1029/2004GL021646.
- Dan, G., Sultan, N., Cattaneo, A., Deverchere, J. and Yelles, K.** (2010), Mass-transport deposits on the Algerian margin (Algiers Area): Morphology, Lithology and Sedimentary processes, *Advances in Natural and Technology Hazards Research*, in: "Submarine Mass Movements and Their Consequences", Mosher DC., Ship C., Moscardelli, L., Chaytor, J., Baxter, C., Lee, H. and Urgeles, R. (Eds), 28. 527-539, 2010.
- Domzig, A., Le Roy, C, Yelles, K., Deverchere, J., Bouillin, J-P, Bracene, R., Mercier de Lepinay, B., Le Roy, P., Calais, E., Kherroubi, A., Gaulier, V., Savoye, B. and Pauc, H.** (2006), Searching for the Africa-Eurasia Miocene boundary offshore western Algeria (MARADJA'03 cruise), *C. R. Geoscience*, 338, 80-91.
- EERI** (2003), The Boumerdes, Algeria, Earthquake of May 2003, EERI Learning from Earthquakes Reconnaissance Report, 71 pp.
- Harbi, H., Maouche, S., Vaccari, F., Aoudia, A., Oussadou, F., Panza, G.F. and D. Benouar** (2007), Seismicity, seismic input and site effects in the Sahel-Algiers region (North Algeria), *Soil Dynamics and Earthquake Engineering*, Vol. 27, 5, 427-447.
- Heezen, B.C. and M. Ewing** (1955), Orleansville earthquake and turbidity currents, *AAPG Bull.*, 39, 2505-2514.
- Kanamori, H. and Anderson D.** (1975), Theoretical basis of some empirical relations in seismology, *Bulletin of seismological society of America*, 65, 5, 1073-1095.
- Mader, C.L.** (2004), Numerical Modeling of Water Waves, second edition, *CRC Press*, 269 pp.
- Maouche, S., Morhange, C. and Meghraoui, M.** (2009), Large boulder accumulation on the Algerian coast evidence tsunami events in the western Mediterranean, *Marine Geology*, 262, 96-104.
- Mauffret, A.** (2007), The Northwestern (Maghreb) boundary of the Nubia (Africa) Plate, *Tectonophysics*, 429, 21-44, doi: 10.1016/j.tecto.2006.09.007
- Marinas Lopez, J.M. and Salord, R.** (1990), El periodo sismico oranes de 1790 a la luz de la documentacion de los archivos espanoles, *I.G.N Publication*, 6, Madrid, 64 pp.
- Meghraoui, M.** Geologie des Zones Sismiques du Nord de l'Algerie : Paleosismologie, Tectonique Active et Synthese Sismotectonique, These de Doctorat Es Sciences, Universite de Paris Sud, Centre d'Orsay, 1988, 366 pp.

- Meghraoui, M.** (1990), Blind reverse faulting system associated with the Mont Chenoua-Tipaza earthquake of 29 October 1989 (north-central Algeria), *Terra Nova*, 3, 84-93.
- Okada, Y.** (1992), Internal deformation due to shear and tensile faults in a half-space, *Bulletin of Seismological Society of America*, 82, 2, 1018-1040.
- Papadopoulos, G. A. and Imamura, F.** (2001), A proposal for a new tsunami intensity scale, ITS 2001 Proceedings, session 5, number 5-1, 569-577.
- Roger, J. and Hebert, H.** (2008), The 1856 Djijelli (Algeria) earthquake and tsunami: source parameters and implications for tsunami hazard in the Balearic Islands, *Natural Hazards Earth System Sciences*, 8, 721-731.
- Soloviev, S. L. and Ch. N. Go** (1974), A catalogue of tsunamis on the western shore of the Pacific Ocean, Moscow, "Nauka" Publishing House, 308 p.. English Translation: Soloviev S. L., Go Ch. N. (1984), A catalogue of tsunamis on the western shore of the Pacific ocean, Translation by Canada Institute for Scientific and Technical Information, National Research Council, Ottawa, Canada KIA OS2.
- Wells, D. L. And Coppersmith, K. J.** (1994), New Empirical Relationships among Magnitude, Rupture Length, Rupture Width, Rupture Area, and Surface Displacement, *Bulletin of seismological society of America*, 84, 4, 974-1002.
- Yelles-Chaouche, A. K., Roger, J., Deverchere, J., Bracene, R., Domzig, A., Hebert, H. and Kherroubi, A.** (2009), The 1856 tsunami of Djidjelli (Eastern Algeria): Seismotectonics, modelling and hazard implications for the Algerian coast. *Pure and Applied Geophysics*, 166 (1-2), 283-300.

ISSN 8755-6839



SCIENCE OF TSUNAMI HAZARDS

Journal of Tsunami Society International

Volume 31

Number 1

2012

Copyright © 2011 - TSUNAMI SOCIETY INTERNATIONAL

TSUNAMI SOCIETY INTERNATIONAL, 1741 Ala Moana Blvd. #70, Honolulu, HI 96815, USA.

WWW.TSUNAMISOCIETY.ORG